THÈSE

En vue de l'obtention du

DOCTORAT DE L'UNIVERSITÉ DE TOULOUSE

Délivré par l'Institut National Polytechnique de Toulouse

Spécialité : Dynamique des f uides

Présentée et soutenue par Laia MORET-GABARRO

le 26 / 10 / 2009

Aeroacoustic investigation and adjoint analysis of subsonic cavity f ows

Etude aéroacoustique et analyse par l'état adjoint d'un écoulement subsonique de cavité

JURY

Pr. Christophe Airiau	Professeur, Université de Toulouse III	Directeur de thèse
Pr. Mejdi Azaiez	Professeur, ENSCPB, Bordeaux	Rapporteur
Pr. Alessandro Bottaro	Professeur, Università di Genova	Examinateur
Dr. Patricia Cathalifaud	Maître de Conférence, Université de Toulouse III	Co-directrice de thèse
Dr. Hugues Deniau	Chercheur, CERFACS, Toulouse	Examinateur
Pr. Azzedine Kourta	Professeur, Polytech Orléans	Examinateur
Dr. Aloïs Sengissen	Docteur, AIRBUS, Toulouse	Invité
Dr. Denis Sipp	Maître de Recherche (HDR), ONERA, Meudon	Rapporteur

---

École doctorale: Mécanique, Energétique, Génie Civil, Procédés (MEGeP)

Unité de recherche: Institut de Mécanique des Fluides de Toulouse (IMFT)

Contents

Acknowledgements

Je remercie Christophe Airiau, mon directeur de thèse, pour m'avoir accueillie au sein du groupe EMT2 à l'IMFT et m'avoir donnée l'opportunité de participer à cette expérience internationale. Je lui suis reconnaissante pour avoir assuré la direction de mes travaux et pour mavoir fait partager son expérience dans la recherche. Je remercie Patricia Cathalifaud, ma co-directrice de thèse, pour son enthousiasme, sa patience, sa motivation et sa bonne humeur pendant les longs mois de développement du code, ainsi que pour son aide pour les résumés en français de la thèse.

Je remercie chaleureusement Anaïs Guaus, qui a commencé à écrire le code numérique avec lequel j'ai travaillé. Je lui suis reconnaissante pour m'avoir montré tous les secrets du code, pour avoir partagé avec moi ses connaissances et pour ses conseils. Merci d'avoir toujours répondu à mes questions, même pendant et après la f n de ta thèse.

Je remercie Alessandro Bottaro pour avoir accepté de présider mon jury de thèse, ainsi que pour les discussions sur l'adjoint. Je remercie Mejdi Azaiez et Denis Sipp pour avoir évalué mes travaux de thèse en tant que rapporteurs, et Azzedine Kourta, Hugues Deniau et Aloïs Senginssen pour avoir accepté de prendre part à mon jury. Merci à tous pour vos observations pendant la soutenance.

Thanks to Sivam and Kaushik, my AeroTraNet collegues in Toulouse, who have travelled with me in this long journey of discovery of research. Thanks for your professional help, constant support and encouragement, and specially for your friendship.

Thanks to all the members of the AeroTraNet project to welcome us at the Politecnico di Torino, Università di Roma Tre and University of Leicester during the AeroTraNet meetings. Thanks to Aldo Rona to have welcome me in Leicester for a three-week stay, and to Jenny Ruane to organise the accommodation and transport. Thanks to Aldo Rona, Ivan Spisso and Marco Grottadaurea for interesting discussions on boundary conditions during the exchange visits and meetings.

Merci à mes amis et collègues de l'EMT2 pour les pauses 'thé' et pour avoir assuré la bonne ambiance et la bonne humeur au labo: Houssam, Xavier, Karim, Romain, Tim, Matteo, Wafa, Fernando, Marie, Rudy, Thibaud, Benjamin.

Je remercie le personnel administratif et technique de l'IMFT, et spécialement Marie Christine Tristani, secrétaire du group EMT2, pour avoir assuré toutes les démarches administratives. Merci également au personnel du Service Informatique pour sa patience à cause de mes nombreuses visites (et merci aussi à mon ordinateur C3PO qui, malgré tout, a fonctionné jusqu'à la f n de la thèse !).

Un petit mot aussi pour mes professeurs de français successifs, grâce auxquels j'ai pu soutenir la thèse en français.

Thanks to Johan Larsson and Clancy Rowley for interesting discussions about cavity f ows.

Merci à mes amis qui ont fait de mon séjour à Toulouse une expérience inoubliable : Mariyana et Bernhard 'les danseurs'; Jeanne, Dirk et les 'DeDanuistes'; Yannick 'le conseiller'; Sheetal, Yogesh et le petit Alaap; les 'doctoriants', le groupe de l'Alliance et les 'managers d'équipe'. Ana, muchas gracias por todo, y gracias también a Mauro y al resto de la red.

Very special thanks to all the friends who have been sending me their support from Barcelona, Göteborg, Durham, Olso, Madrid, Eindhoven, Montpellier, Paris... Moltes gràcies, muchas gracias, merci beaucoup, thanks a lot, grazie mille, danke och tack så mycket! And thanks to Marc 'Kitus' for his tips in latex.

And f nally, thanks to Roger (my brother) to make me laugh even in the most diff cult situations, and to Francesc and Gloria (my parents) to accept that I f y from country to country and to send me their support. Moltes gràcies!

This work has been done at the Institut de Mécanique des Fluides de Toulouse (IMFT), as part of the European project AerotraNet. This research project has been supported by a Marie Curie EST Fellowship of the European Communitys Sixth Framework Programme under contract number MEST CT 2005 020301. The computer resources provided by IDRIS (Orsay, France) are acknowledged.

Nomenclature

Roman

A	Amplitude of the forcing
c	Ambient speed of sound
c_p	Specif c heat at constant pressure
D	Depth of a cavity or height of a backward-facing-step
e	Internal energy
f	Frequency of oscillation
f'	Forcing of the direct f eld
F	Fluxes in *x*-direction
g^*	Forcing of the adjoint f eld
G	Fluxes in *y*-direction
h	Half-width of a channel
H	Shape factor of a boundary layer
$\mathcal{J}()$	Cost function
L	Length of a cavity
$\mathcal{L}()$	Lagrangian function
$\mathcal{L}_i$	Characteristic waves
m_x, m_y	*x*- and *y*-momentum
$\mathcal{N}()$	Navier-Stokes operator
p	Pressure
q	Vector of conservative variables
q_x, q_y	Heat f uxes in *x*- and *y*-direction
r	Universal gas constant
t	Time
T	Temperature
$\mathcal{T}$	Period of oscillation
u	Velocity in *x*-direction
U	Conservative variables of the system
v	Velocity in *y*-direction
W	Spanwise width of a cavity

Greek

γ	Ratio of specif c heats
δ	Boundary layer thickness
δ_{ij}	Kronecker Delta
Δ	Increment
θ	Momentum thickness
Θ	Dilatation
λ	Thermal conductivity
μ	Dynamic viscosity
ξ	Equidistant mesh spacing
ρ	Density
σ	Relaxation coeff cient
σ_p	Radius of the Gaussian pulse
τ	Wall friction
τ_{ij}	Viscous stress tensor
Φ_v	Viscous dissipation term
ω	Vorticity
ω_p	Frequency of the forcing
Ω	Spatial domain

Abbreviations

b.c.	Boundary condition
BT	Boundary terms
CFD	Computational Fluid Dynamics
CFL	Courant number
CAA	Computational Aeroacoustics
DES	Detached Eddy Simulation
DNS	Direct Numerical Simulation
DRP	Dispersion-relation-preserving
FFT	Fast Fourier Transform
$k-\omega$	$k-\omega$ turbulence model
LES	Large Eddy Simulation
LRM	Linear Relaxation Method
NS	Navier-Stokes
OSPL	Overall Sound Pressure Levels
PDE	Partial Differential Equation
PIV	Particle Image Velocimetry
POD	Proper Orthogonal Decomposition
PSE	Parabolized Stability Equations
RANS	Reynolds Averaged Navier-Stokes
1D	Mono dimensional
2D	Two dimensional
3D	Three dimensional

Subscripts and superscripts

c	Convective (f uxes)
f	Condition at the f nal time
g	Ghost cell
v	Viscous (f uxes)
w	Wall
0	Condition at the initial time
∞	Freestream value
$\tilde{a}$	Adimensional
a^*	Adjoint variable
a'	Perturbation
$\dot{a}$	Time derivative

Adimensional numbers

M	Mach number
Pr	Prandlt number
Re	Reynolds number
St	Strouhal number

General introduction

Recent rise in aviation transport and environmental concern has caused a growing interest in environmentally friendly aircrafts. Pollutant emissions have raised over the past years. The concentration of carbon dioxide (CO_2) in the atmosphere has increased by more than 30% after the industrial revolution [100]. Greenhouse gases contribute to climate change and global warming, in addition to other environmental impacts, such as sulphuric acid formation in the atmosphere, and health problems like respiratory diseases. From an aerodynamic point of view, gas emissions from aircrafts can be related to the gas consumption caused by the drag.

Furthermore, there is another issue which concerns aircrafts and causes environmental and health problems: the noise. Continuous exposure to high levels of noise, for example in the vicinity of an airport, may induce temporal or permanent health problems. Some of them are increase in stress, blood pressure and heart rate. Cardiovascular effects are associated with long-term exposure to values in the range of 65 to 70 dB or more, for both air- and road-traffic noise [181]. A mechanical damage of the ear can occur with very high instantaneous Sound Pressure Levels (around 140dB for adults and 120dB for children) [181].

Aircraft noise has three main sources, namely mechanical, aerodynamic and from aircraft systems. Mechanical noise is mainly produced by the engines. The aerodynamic noise is created by the unsteady flow around airframes. Aircraft systems contribute to the interior cabin noise. During landing, aerodynamic noise is as important as mechanical noise, thus the interest to reduce it.

Nowadays the understanding of these problems are motivating the research on environmentally friendly aircrafts, that is to say aircrafts which are *more affordable, safer, cleaner and quieter* [60].

AeroTraNet project

This PhD thesis is part of an European Project named AeroTraNet, which is the acronym for *Unsteady AEROdynamics TRAining NETwork* [1]. The AeroTraNet project concerns the investigation of aerodynamic aircraft noise, where the flow over a cavity is studied. The unsteady flow over a cavity produces the emission of acoustic waves which are perceived in the far-field as noise. A cylindrical cavity can be used to model a fuel vent, and a rectangular cavity can be seen as a cut-off or a gap in the airframe.

The project involves four research institutes: the University of Leicester (Leicester, UK), the Università degli Studi Roma Tre (Rome, Italy), the Politecnico di Torino (Turin, Italy) and the Institut de Mécanique des Fluides de Toulouse (Toulouse, France). The common objective is the study of different aspects of an unsteady flow over a cavity. Time-accurate computational fluid dynamics is performed

in Leicester, experimental aeroacoustics in Rome, time-resolved experimentation with Particle Image Velocimetry in Turin and reduced order modelling and flow control in Toulouse.

Overview of the thesis

The objective of this thesis is to numerically investigate the aeroacoustics of a rectangular cavity and to find strategies to reduce the noise. This document is divided in two parts - *direct simulations* and *adjoint simulations*.

The direct algorithm solves a set of equations which reproduce the physics of the flow, that is to say, it involves physical variables as velocity, pressure or temperature. Since it works with physical quantities, it can be validated using experimental data. The equations are time dependent, and so the iterative method starts at a given initial condition and time-marches the solution until the desired final time. The direct code is used to accurately predict both flow and acoustic fields in order to understand the mechanism of noise generation.

On the other hand the adjoint algorithm solves a set of equations which are mathematically derived from the direct system. The adjoint variables are not measurable quantities, even though they do have a physical meaning, representing the sensitivity of the flow to external forcing. One of the peculiarities of the adjoint algorithm is that it marches backward in time.

A question might arise: *why is it interesting to move backward in time?*. Imagine that for a given system (for an example an aircraft) and certain initial conditions the acoustic emission is known. Since the noise is too high, it must be reduced to a certain value. In this case the final state is known (the maximum value of noise allowed) and the initial condition is sought.

The adjoint code is then used to investigate the regions of the configuration where flow modifications would be more effective, in order to envision flow control strategies. This investigation is performed by a sensitivity analysis.

The structure of the document is as follows:

Direct simulations. Chapter §1 describes the numerical method used to implement the direct simulation algorithm. After that the code is validated by performing several test cases in chapter §2. Finally, in chapter §3 the direct algorithm is used to investigate the cavity flow oscillations and the emission of acoustic waves.

Adjoint simulations. In chapter §4 the mathematical formulation of the adjoint methods is given, as well as its numerical implementation for the present case. The validation of the adjoint algorithm is described and shown in chapter §5. At last, in chapter §6 the sensitivity analysis of channel and cavity flows is performed.

Part I

DIRECT SIMULATIONS

Chapter 1

Direct Numerical Simulation in compressible f ows

Simulation Numérique Directe d'un écoulement compressible

Dans ce chapître, nous nous sommes focalisés sur la simulation numérique d'écoulements subsoniques de cavités pour des nombres de Mach allant de 0.15 à 0.6. Nous avons pour celà utilisé un code aéroacoustique de simulation directe des équations de Navier-Stokes (DNS) sans aucun modèle de turbulence où les variables d'écoulement sont fonctions de l'espace et du temps. Ce code est écrit en Fortran, et son premier développement a été réalisé à l'IMFT par Anaïs Guaus (voir l'Appendice A de [82]). Les équations de Navier-Stokes non linéaires compressibles bidimensionnelles sont sous forme conservative, et écrites en coordonnées cartésiennes (x, y).

Schémas d'ordre élevé

Dans le cas d'écoulements compressibles, nous devons calculer non seulement le champ d'écoulement, mais aussi les ondes acoustiques, les ondes d'entropie et les ondes de vorticité. Afin de prédire correctement la propagation de ces ondes, les discrétisations spatiale et temporelle doivent être d'ordre élevé. De plus, la description des ondes instationnaires de petites échelles et de hautes fréquences nécessite que la dispersion et la dissipation des schémas numériques soient minimisées [34]. Pour celà, nous avons à notre disposition dans la littérature de nombreuses formulations de schémas d'ordre élevé.

Pour obtenir des résultats de haute précision, certaines précautions quant aux schémas numériques utilisés doivent être prises. Ainsi, les schémas explicites doivent alors faire intervenir une formulation utilisant un grand nombre de points de discrétisation. D'autres types de schémas sont donc plus appropriés, tels les schémas optimisés qui minimisent la différence entre la dispersion physique et numérique pour une gamme choisie de longueurs d'onde et de fréquences [170]. En résolvant de manière implicite les dérivées spatiales en chaque point de discrétisation, les schémas compacts, à précision égale avec les schémas explicites, font intervenir dans leur formulation un plus petit nombre de points de discrétisation [119]. Ce nombre de points peut être encore plus réduit en utilisant des schémas compacts préconditionnés [93].

Cependant, même les schémas d'ordre élevé (qu'ils soient optimisés ou compacts) peuvent présenter des ondes d'origine purement numérique provenant d'un décalage fréquentiel dû aux différences centrées. Les solutions communes pour éliminer ces ondes dites 'spurious' sont l'utilisation d'un filtre passe-bas, ou bien l'ajout d'amortissement au membre de droite de l'équation de l'énergie, ou encore l'amortissement par l'utilisation de schémas décentrés en amont, dépendants de la direction locale de la vitesse du son. Toutes ces méthodes ont un inconvénient commun : l'augmentation du temps de calcul.

Une méthode alternative consiste à utiliser une formulation dite 'progressive-regressive', c'est-à-dire une combinaison de schémas aux différences finies décentrés d'un coté puis de l'autre (en aval puis en amont), créant de manière intrinsèque un amortissement des ondes 'spurious', sans augmenter le temps de calcul. Ce type de formulation a été proposé pour la première fois par Kloker [108], comme extension du schéma centré du $6^{ème}$ ordre proposé par Lele [119].

Le schéma sélectionné pour la discrétisation des flux convectifs est le schéma compact du $6^{ème}$ ordre en formulation 'progressive-regressive' proposé par Kloker [108]. Quant aux flux visqueux, nous pouvons leur appliquer une discrétisation numériquement moins coûteuse car ils ne nécessitent pas une précision aussi élevée que les flux convectifs. Un schéma explicite classique du $4^{ème}$ ordre a donc été implémenté.

Une méthode standard de Runge-Kutta du $4^{ème}$ ordre a été utilisée pour la discrétisation temporelle. Chaque itération contient quatre sous-itérations de Runge-Kutta où nous alternons entre des formulations en décentrage aval et amont pour le schéma spatial.

Conditions aux limites non réfléchissantes

Des conditions aux limites non réfléchissantes doivent permettre aux ondes de quitter le domaine de calcul sans réflexion. De plus, nous devons définir l'état de l'écoulement entrant dans le domaine de calcul, condition qui est a priori connue et peut donc être imposée à la limite d'entrée du domaine de calcul. Il existe de nombreux travaux qui ont étudié différentes méthodes pour avoir des conditions aux limites non réfléchissantes [169]. Nous pouvons en gros en distinguer trois types : la méthode des caractéristiques, l'utilisation de solutions asymptotiques, et l'ajout d'une zone tampon dite zone 'buffer'.

L'idée principale des conditions aux limites caractéristiques est la décomposition des ondes traversant les limites du domaine en ondes entrantes et sortantes, puis la suppression les ondes entrantes [171]. Dans la première version du code écrite par Anaïs Guaus [82], les conditions aux limites caractéristiques de Giles [73, 74] ont été implémentées. Elles nécessitent que l'écoulement moyen soit estimé à toutes les frontières du domaine, car la différence entre les écoulements moyen et instantanné est utilisée pour calculer les ondes traversant les frontières du domaine.

Une difficulté supplémentaire apparaît aux frontières de sortie d'écoulement. En effet, l'écoulement moyen n'est a priori pas connu en aval à l'exception de la pression à l'infini aval. C'est pourquoi, nous avons implémenté dans ce cas une autre condition aux limites qui ne dépend d'aucune connaissance particulière des profils de vitesse de sortie : la formulation des conditions caractéristiques de Poinsot et Lele [140]. Cette méthode, adaptée aux équations de Navier-Stokes, prend en compte les non linéarités de l'écoulement. A la limite de sortie d'écoulement, l'onde sortante n'est pas entièrement supprimée, mais elle est estimée d'après la différence de pression statique $P - P_\infty$, ce qui permet à l'information concernant le champ de pression lointain d'interagir avec le domaine de calcul.

Les conditions aux limites de type asymptotique simulent les conditions aux limites en utilisant pour le

champ lointain l'expression asymptotique des équations d'Euler linéarisées. Cette approche est formulée en coordinnées cylindriques, où l'origine est habituellement choisie comme étant le centre de la source de bruit (mais il a été montré que cette origine peut en fait être fixée arbitrairement). Le principal avantage de cette approche est qu'elle est multidimensionnelle et que le problème lié aux coins est minimisé de par l'utilisation de coordonnées cylindriques. La formulation asymptotique de Tam and Dong [168] a été implémentée durant le développement de la version mono-bloc du code, et les résultats obtenus furent quasi identiques à ceux obtenus par la méthode des caractéristiques [82, 149].

Même avec des conditions aux limites non réfléchissantes, il est parfois impossible d'éviter des réflexions d'onde, en particulier aux coins du domaine de calcul. Une méthode classique utilisée pour supprimer ces réflexions est l'ajout d'une zone tampon ou zone 'buffer'. Cette zone tampon, dite aussi couche d'absorption, est une région de dimension finie ajoutée à l'extérieur du domaine de calcul où la physique de l'écoulement est modifiée. Cette zone tampon augmente l'efficacité de la condition aux limites, voire dispense même de l'utilisation d'une condition aux limites particulière. Dans les simulations que nous avons effectuées, nous avons utilisé une zone tampon constituée d'un maillage de plus en plus étiré au fur et à mesure que l'on s'éloigne de la condition aux limites, ainsi que d'un filtre tel que proposé par Lele [119].

Conditions aux limites de paroi

La formulation de conditions aux limites appropriées au cas de paroi solide pour des schémas d'ordre élevé est toujours un problème ouvert. En effet, les formulations communément utilisées pour les schémas d'ordre peu élevé peuvent conduire à des instabilités numériques quand elles sont appliquées aux schémas d'ordre élevé. Plusieurs solutions existent afin d'éviter ces solutions non physiques, telles que les conditions aux limites caractéristiques parfaitement réflexives qui sont basées sur la décomposition des ondes arrivant aux parois. Elles présentent cependant certains problèmes dans le cas d'ondes non perpendiculaires aux parois [140].

Une autre solution consiste à estimer les flux convectifs aux parois, ainsi que l'a proposé sous une formulation robuste Gloerfelt [75], solution qui a été implémentée dans la première version du code [82]. Cette condition a été validée pour des problèmes mono-bloc, mais elle a des difficultés à simuler correctement les écoulements au-dessus de surfaces discontinues en raison du couplage dans la dérivation multi-blocs.

La solution alternative à ce problème consiste à implémenter des points de maillage fantômes, appelés 'ghost cells'. Les 'ghost cells' sont des points de maillage utilisés à des fins numériques, placés à l'extérieur du domaine physique en vue de simuler la réflexion à la paroi solide. Pour les géométies de type cavité rectangulaire ou marche, les autres méthodes génèrent souvent l'apparition de fortes instabilités numériques à côté des coins supérieurs. Une méthode de type 'ghost cells' sans aucun point de maillage aux parois permet donc de contourner la complexité d'avoir à gérer des points de maillage placés exactement aux coins. C'est donc ce type de méthode qui a été utilisée pour implémenter des parois solides isothermes.

Nous présentons ici la méthode proposée par Guaus [82] pour calculer les dérivées dans le cas de configurations multi-blocs. Elle est basée sur la définition de plusieurs configurations des différents blocs suivant les directions des coordonnées cartésiennes, comme illustré dans les figures 1.5 (pas de 'ghost cells') et 1.6 (avec 'ghost cells').

Conclusion

En conclusion, un schéma compact du $6^{ème}$ ordre en formulation 'progressive-regressive' été utilisé pour la discrétisation spatiale des flux convectifs, et un schéma classique du $4^{ème}$ ordre de type Runge-Kutta a été utilisé pour la discrétisation en temps. Les conditions aux limites caractéristiques de Giles sont implémentées pour les frontières non réfléchissantes, et les conditions aux limites caractéristiques de Poinsot et Lele sont implémentées à la frontière de sortie de l'écoulement. Pour les parois solides, des conditions aux limites de type 'ghost cells' ont été implémentées et couplées avec la dérivation multi-blocs.

Introduction

The approach used to determine the flow variables is Direct Numerical Simulation (DNS), in which the Navier-Stokes equations are numerically solved without any turbulence model and the flow variables are obtained as a function of space and time. The first incompressible DNS computations date of the early 70's, when Orszag and Patterson [137] investigated isotropic turbulence numerically, and Fasel [61] studied the stability and initial transition phenomena of two-dimensional (2D) boundary layer flows. The development of DNS incompressible flows continued during the 80's [107, 117, 135], but it was not until the 90's that the first computations of compressible wall-bounded flows were done [37, 144]. A good review on Direct Numerical Simulation was written by Moin and Mahesh [132].

During the last 20 years the complexity of the simulations has increased, DNS being nowadays applied to computational aeroacoustic studies [49, 47, 116, 151] as well as flow control [8, 19, 42, 152]. However, the Reynolds number remains low respect to the values that are significant for real flows.

As the Reynolds number increases, so does the instantaneous range of space and time scales, making difficult the use of DNS for most engineering problems. Alternative numerical methods used to solve high Reynolds number problems are Large Eddy Simulation (LES) and Reynolds averaged Navier-Stokes (RANS). In LES the small energy-containing scales are modelled and the large scales are computed, hence reducing the grid requirements (see [120] for a review). In RANS, the statistical evolution of the flow is computed instead of the instantaneous flow-field (see [163] for a review).

As the Mach number increases, compressibility effects are more important and acoustic propagation as well. The far-field noise originated by an unsteady flow system can be predicted by several methods. One approach consists on computing it directly from a highly-accurate DNS of the Navier-Stokes equations, using a Computational Aeroacoustics (CAA) algorithm. In an alternative method, the noise is extracted from an approximate compressible flow prediction using an acoustic analogy [54, 63, 121].

The present study is focused to subsonic cavity flows for a Mach number range from 0.15 to 0.6. For this objective, the Computational Aeroacoustics code outlined in table 1.1 is used. The code is written in Fortran and the first developments were done by Anaïs Guaus at IMFT, as described in the Appendix A of [82]. The numerical method consists of a 6^{th} order compact scheme in space, a 4^{th} order scheme in time, the characteristic boundary conditions of Giles [73, 74] at the non-reflecting boundaries and the solid boundary conditions proposed by Gloerfelt [75] at the walls. More details are given in the coming sections.

Spatial discretization of convective f uxes	6^{th} order compact forward-backward scheme [108]
Spatial discretization of viscous f uxes	4^{th} order classic explicit scheme
Temporal discretization	4^{th} order classic Runge-Kutta scheme
Inf ow, radiation boundary conditions	characteristics of Giles [73, 74]
Outf ow boundary condition	characteristics of Giles [73, 74] characteristics of Poinsot and Lele [140]
Wall boundary conditions	formulation of Gloerfelt [75] ghost cells

Table 1.1 - *Overview of the numerical method. The boundary conditions are illustrated in figure 1.1.*

During the present work two new boundary conditions have been implemented: a wall boundary condition using ghost cells, described in §1.5.2, and the outf ow characteristic boundary condition of Poinsot and Lele [140], explained in §1.4.1. In addition, the multi-block treatment has been modif ed, as illustrated in §1.6.2.

This chapter starts with a brief introduction to Computational Aeroacoustics (§1.1). After that the governing equations are given (§1.2). Then the numerical method is described: spatial and temporal discretization (§1.3), non-ref ecting (§1.4) and solid (§1.5) boundary conditions. At the end, the treatment of the different blocks is explained (§1.6).

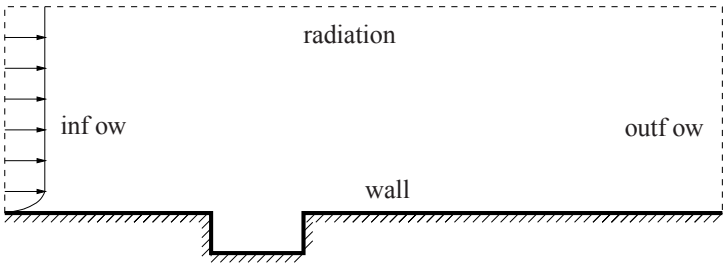

Figure 1.1 - *Computational domain and boundary conditions.*

1.1 Computational Aeroacoustics

In high Mach number f ows, not only the f ow f eld must be predicted but also the acoustic, entropy and vorticity waves. The acoustic waves are isotropic, non-dispersive, non-dissipative and propagate at the speed of sound. They expand radially and in the presence of a mean f ow they are convected downstream. The entropy and vorticity waves are non-dispersive, non-dissipative and highly directional, and they are convected in the direction and at the speed of the mean f ow without any distortion.

To predict wave propagation, spatial and temporal discretization must be of high order, and dispersion and dissipation must be minimized, in order to correctly describe unsteady, small scale, high-frequency waves [34]. In traditional Computational Fluid Dynamics (CFD) only the formal order of the scheme is considered to evaluate the quality of the results (i.e. a 4^{th} order scheme is expected to provide more accurate results than a 2^{nd} order scheme).

On the other hand, in CAA formal order gives no information about the accuracy, since numerical dispersion and dissipation, anisotropy, and prediction of wave propagation might induce higher errors than differentiation. Numerical dissipation is caused by the variation of the group velocity of the wave components of different wave numbers. Numerical dispersion can arise from spatial discretization, temporal discretization or both. Therefore, non-dispersive and non-dissipative properties are more relevant than formal order of accuracy [169]. A better description of high-order schemes is found in section §1.3.

For accurate prediction of acoustic waves numerical damping must be avoided, which can be achieved by taking a small time step. Actually, is has been shown that the time step must be much smaller than that indicated by the stability criterion in order to avoid dispersion and dissipation errors [97, 98]. Hu *et al.* [97, 98] derived a low-dissipation and low-dispersion Runge-Kutta scheme which optimizes (minimizes) the dissipation and dispersion errors for wave propagation [97, 98].

Boundary conditions must be adapted to high-order schemes. Far-field boundaries must avoid the reflection of waves: inflow and radiation boundaries must allow acoustic waves to leave the domain, and outflow boundaries must allow acoustic, entropy and vorticity waves to exit from the domain without reflection. Wall boundary conditions must avoid numerical instabilities. More details on boundary conditions are given in the following sections §1.4 and §1.5.

1.2 Governing equations

The code is implemented with the non-linear 2D compressible Navier-Stokes (NS) equations with conservative variables in Cartesian coordinates (x, y):

$$\frac{\partial U}{\partial t} = -\frac{\partial F^c}{\partial x} - \frac{\partial G^c}{\partial y} + \frac{\partial F^v}{\partial x} + \frac{\partial G^v}{\partial y} \tag{1.1}$$

with:

$$\begin{aligned} U &= (\rho,\ \rho u,\ \rho v,\ \rho e)^t \\ F^c &= (\rho u,\ p + \rho u^2,\ \rho uv,\ (\rho e + p)u)^t \\ G^c &= (\rho v,\ \rho uv,\ p + \rho v^2,\ (\rho e + p)v)^t \\ F^v &= (0,\ \tau_{11},\ \tau_{12},\ u\tau_{11} + v\tau_{12} - q_1)^t \\ G^v &= (0,\ \tau_{12},\ \tau_{22},\ u\tau_{12} + v\tau_{22} - q_2)^t \end{aligned} \tag{1.2}$$

where U are the unknown conservative variables of the system. F^c and G^c represent the convective fluxes and F^v and G^v the viscous fluxes. p, ρ and e are the pressure, density and internal energy of the flow respectively. u and v represent the velocity in *x*- and *y*- directions of the Cartesian system. τ_{ij} and q_i are the viscous stress tensor and the heat fluxes. And subscript t indicates the transpose of the vector.

For a Newtonian fluid, by Fourier's heat law the viscous stress tensors and heat fluxes are:

$$\begin{aligned} \tau_{ij} &= \mu\left(\frac{\partial u_i}{\partial x_j}+\frac{\partial u_j}{\partial x_i}-\frac{2}{3}\delta_{ij}\frac{\partial u_k}{\partial x_k}\right) \\ q_i &= -\lambda\frac{\partial T}{\partial x_i}=-\frac{\mu c_p}{Pr}\frac{\partial T}{\partial x_i} \end{aligned} \tag{1.3}$$

where μ is the dynamic viscosity which depends on the temperature T, λ is the thermal conductivity, $Pr = 0.72$ is the Prandlt number considered constant and c_p is the specif c heat at constant pressure. The repetition of the index k indicates the summation of this index by Einstein's notation (also known as Einstein's summation convention) and δ_{ij} is the Kronecker delta, which is equal to 1 if $i = j$, and 0 otherwise. Also note that the index 1 indicates the streamwise direction and 2 corresponds to the direction normal to the f ow, so $x_1 = x$, $x_2 = y$, $u_1 = u$ and $u_2 = v$.

The temperature can be obtained from the equation of state for ideal gases:

$$\begin{aligned} p &= \rho r T \\ e &= \frac{p}{[(\gamma-1)\rho]}+\frac{u^2+v^2}{2} \end{aligned} \tag{1.4}$$

where r is the universal gas constant and γ is the ratio of specif c heats.

The implemented algorithm can also be used to solve the compressible Euler equations by neglecting the viscous terms F^v and G^v.

1.3 Spatial and temporal discretization

Performing numerical simulations of compressible f ows with a discretized system of equations might create unphysical, high frequency spatial oscillations. In order to minimize this problem, high-order schemes with low dissipative and low dispersive properties are becoming more and more popular.

Explicit schemes require large computational stencils to obtain high-accuracy results (e.g. a 6^{th} order explicit scheme needs a seven-point stencil in a constant uniform mesh). Optimized schemes minimize the difference between the physical and the numerical dispersion relationship over a chosen range of wavelengths and frequencies. The coeff cients are determined up to a certain formal order of accuracy and the remaining coeff cients are optimized. An example of an optimized scheme is the dispersion-relation-preserving (DRP) scheme of Tam and Webb [170].

Compact (implicit) schemes use smaller stencils by implicitly solving the spatial derivatives at each point. For instance, a 6^{th} order compact scheme uses a f ve-point stencil. Compact schemes are more accurate than explicit ones and give results similar to optimized schemes. Nevertheless, they have some disadvantages: a linear system must be solved to obtain the derivatives, increasing the computational time and making the algorithm more diff cult to parallelize, and the boundary stencil has a large effect on the stability and the accuracy of the scheme. Examples of compact schemes are the formulations of Lele [119] and Kloker [108].

Prefactored compact schemes allow the use of even smaller stencils, e.g. from five to three points to obtain 6^{th} order accuracy. The original tridiagonal matrix is reduced by factorization to independent upper and lower bidiagonal matrices. A part than a smaller stencil, it presents other advantages: only one boundary stencil is necessary, and the computational time required is lower than for a standard compact scheme. The main disadvantage is that when solving non-linear equations, artificial dissipation is required to damp spurious high-frequency waves generated in the solution. This formulation was proposed by Hixon [93].

However, even high-order (optimized or compact) schemes might present spurious waves originated by a frequency shift due to the central differentiation. Common solutions to eliminate the undesired waves are low-pass filtering, extra damping on the right hand side of the energy equation or damping by an upwind-biased scheme depending on the local sign of the sound speed. All these methods have a common disadvantage: additional computational time.

An alternative method consists on a progressive-regressive formulation, i.e. the combination of positively and negatively biased finite-difference schemes (forward-backward). The forward-backward biased schemes quasi add-up to a central scheme, but with the advantage that the final accuracy is higher than those of the individual steps and the damping in inherent, so no additional computational time is required. This formulation was proposed by Kloker [108] and it is an extension of the usual sixth-order centered scheme proposed by Lele [119].

1.3.1 Spatial discretization

The spatial discretization of the convective fluxes is a compact sixth-order finite-difference scheme optimized in a five-point stencil. A progressive-regressive formulation by Kloker [108] generates numerical fluxes of alternate sign that are used in a classical fourth-order Runge-Kutta scheme to time-march the flow and the acoustic field. In each temporal iteration the forward-backward sequence is inverted to implicitly eliminate high-frequency numerical oscillations, so extra filtering or the introduction of an artificial viscosity term are not necessary. This scheme is stable up to a Courant number of 1.11 [108].

The schemes presented in this section are given in *x*-direction as an example. Their formulation in *y*-direction is equivalent in all the cases. The forward and backward formulations to compute the derivative of the convective flux F^c are [table I, (Ia,Ib) [108]]:

$$\begin{aligned} \frac{\partial F^c_{i-1}}{\partial x} + 3\frac{\partial F^c_i}{\partial x} + \frac{\partial F^c_{i+1}}{\partial x} &= \frac{1}{48\Delta x}(5F^c_{i-2} - 148F^c_{i-1} + 54F^c_i + 76F^c_{i+1} + 13F^c_{i+2}) \qquad (1.5) \\ \frac{\partial F^c_{i-1}}{\partial x} + 3\frac{\partial F^c_i}{\partial x} + \frac{\partial F^c_{i+1}}{\partial x} &= \frac{1}{48\Delta x}(-13F^c_{i-2} - 76F^c_{i-1} - 54F^c_i + 148F^c_{i+1} - 5F^c_{i+2}) \end{aligned}$$

Since it is not possible to use this scheme at the boundaries, a special compact sixth-order scheme with a non-centered five-point stencil is used at the second and the last but one points [table I, (V) [108]]:

$$
\begin{aligned}
6\frac{\partial F_1^c}{\partial x} + 8\frac{\partial F_2^c}{\partial x} + \frac{\partial F_3^c}{\partial x} &= \frac{1}{12\Delta x}(-43F_1^c - 80F_2^c + 108F_3^c + 16F_4^c - F_5^c) \\
6\frac{\partial F_N^c}{\partial x} + 8\frac{\partial F_{N-1}^c}{\partial x} + \frac{\partial F_{N-2}^c}{\partial x} &= \frac{1}{12\Delta x}(43F_N^c + 80F_{N-1}^c - 108F_{N-2}^c - 16F_{N-3}^c + F_{N-4}^c)
\end{aligned} \tag{1.6}
$$

where N is the last point of the computational grid.

The values at the interior domain and the boundaries can be written in a pentadiagonal matrix, and hence the problem can be formulated as:

$$A\, DF^c = BF^c$$

where A is a tridiagonal matrix containing the left-hand-side coeff cients of equations (1.5)-(1.6), B is a pentadiagonal matrix containing the right-hand-side coeff cients of equations (1.5)-(1.6) and F^c is a matrix containing the convective f uxes. The derivatives of the f uxes, DF^c, are determined by LU decomposition.

In order to obtain the derivatives of the f uxes in the whole computational domain, the matrix F^c requires the information of the boundaries, i.e. the f rst and last points. As a consequence, the matrices A and B must be completed with a boundary stencil, which is an explicit f fth-order scheme in a six-point stencil [table I, (IV)[108]]:

$$
\begin{aligned}
\frac{\partial F_1^c}{\partial x} &= \frac{1}{60\Delta x}(-137F_1^c + 300F_2^c - 300F_3^c + 200F_4^c - 75F_5^c + 12F_6^c) \\
\frac{\partial F_N^c}{\partial x} &= \frac{1}{60\Delta x}(137F_N^c - 300F_{N-1}^c + 300F_{N-2}^c - 200F_{N-3}^c + 75F_{N-4}^c - 12F_{N-5}^c)
\end{aligned} \tag{1.7}
$$

Nevertheless, the numerical values of the boundary points are not a direct output of the matricial formulation, but are computed in a later stage using the specif c boundary conditions.

On the other hand, viscous f uxes of the Navier-Stokes equations do not require an accuracy as high as the convective f uxes. They are in general much smaller, and in addition diffusion does not take an important role in the propagation of acoustic waves. Therefore, a less computationally expensive discretization can be used. The implemented scheme is a classic 4^{th} order explicit scheme.

For the interior domain, the derivative of the viscous f uxes F^v is:

$$\frac{\partial F_i^v}{\partial x} = \frac{1}{12\Delta x}(F_{i-2}^v - 8F_{i-1}^v + 8F_{i+1}^v - F_{i+2}^v) \tag{1.8}$$

For the second and the last but one points it is:

$$
\begin{aligned}
\frac{\partial F_2^v}{\partial x} &= \frac{1}{12\Delta x}(-3F_1^v - 10F_2^v + 18F_3^v - 6F_4^v + 5F_5^v) \\
\frac{\partial F_{N-1}^v}{\partial x} &= \frac{1}{12\Delta x}(3F_N^v + 10F_{N-1}^v - 18F_{N-2}^v + 6F_{N-3}^v - 5F_{N-4}^v)
\end{aligned} \tag{1.9}
$$

For the first and last points it is:

$$\begin{aligned}\frac{\partial F_1^v}{\partial x} &= \frac{1}{12\Delta x}(-25F_1^v + 48F_2^v - 36F_3^v + 16F_4^v - 3F_5^v) \\ \frac{\partial F_N^v}{\partial x} &= \frac{1}{12\Delta x}(25F_N^v - 48F_{N-1}^v + 36F_{N-2}^v - 16F_{N-3}^v + 3F_{N-4}^v)\end{aligned} \tag{1.10}$$

When working with a non-equidistant mesh x, it is necessary to derive the variables F (F^c or F^v) respect to an equidistant mesh ξ and then apply the chain rule:

$$\frac{\partial F}{\partial x} = \frac{\partial F}{\partial \xi}\frac{\partial \xi}{\partial x} \tag{1.11}$$

where the term $\partial F/\partial \xi$ is calculated at each iteration using the schemes previously described for the convective and viscous fluxes. On the other hand the term $\partial \xi/\partial x$ is computed once at the beginning of the simulation and stored to be used at each iteration. A 6^{th} order compact centered scheme is used to derive $\partial \xi/\partial x$ [table I, (I) [108]]:

$$\frac{\partial \xi_{i-1}}{\partial x} + 3\frac{\partial \xi_i}{\partial x} + \frac{\partial \xi_{i+1}}{\partial x} = \frac{1}{12\Delta x}(-\xi_{i-2} - 28\xi_{i-1} + 28\xi_{i+1} + \xi_{i+2}) \tag{1.12}$$

where the boundary schemes are the same as those used for the convective fluxes, given in (1.6) and (1.7).

1.3.2 Temporal discretization

The time marching is implemented with a usual 4^{th} order in time Runge-Kutta method. Each iteration has four Runge-Kutta sub-iterations, in which the spatial scheme described in the equations (1.5) alternates the forward $(+)$ and backward $(-)$ steps. Furthermore, at each temporal iteration the sequence is inverted, being for instance $(+-+-)$ whereas in the next temporal iteration is $(-+-+)$.

Each variable U^{n+1} at the iteration $n+1$ is computed from its value U^n at the iteration n, for which three intermediate states U^{n1}, U^{n2} and U^{n3} and needed:

$$\begin{aligned}U^{n1} &= U^n + \frac{\Delta t}{2}r^n \\ U^{n2} &= U^n + \frac{\Delta t}{2}r^{n1} \\ U^{n3} &= U^n + \Delta t r^{n2} \\ U^{n+1} &= U^n + \frac{\Delta t}{6}(r^n + 2r^{n1} + 2r^{n2} + r^{n3})\end{aligned} \tag{1.13}$$

where Δt is the time step and r^k is calculated as

$$r^k = -\frac{\partial}{\partial x}(F_c^k - F_v^k) - \frac{\partial}{\partial y}(G_c^k - G_v^k) \qquad k = n, n1, n2, n3 \tag{1.14}$$

The time step depends on the CFL stability criterion defined by equation (1.15). The maximum Courant number CFL_{max} allowed for convective flows and the considered scheme is 1.11 [108].

$$\Delta t \cdot max\left[\frac{|\ u\ | + c}{\Delta x}\right] \leq CFL_{max} = 1.11 \tag{1.15}$$

where c is the ambient speed of sound. To define the time step Δt, an initial Courant number is used and Δt is kept constant during the computations. After each iteration, a new Courant number is calculated with the new velocity value, and it is verified that it is within a specified limit.

1.4 Non-reflecting boundary conditions

The problem of oscillations is especially difficult to avoid at the boundaries, where due to the extrapolated information and high-order schemes the acoustic waves might be reflected. Moreover, as the acoustic energy is usually a small percentage of the total energy of the flow, the reflected wave (of numerical origin) might be more important than the physical acoustic waves. In steady compressible simulations acoustic phenomena is suppressed by numerical dissipation, which permits a good prediction of the mean flow. In linearized codes, the mean flow is imposed and the acoustic waves can be controlled. On the other hand, the use of non-linear equations and low dispersive low dissipative schemes require adequate boundary conditions which allows a good prediction of the mean flow and prevents acoustic reflection.

A theoretical analysis of the system of equations gives the number of necessary and sufficient conditions that must be imposed to insure that the system is well-posed, and shows that the boundary conditions are independent from the numerical method. For the hyperbolic Euler equations the theoretical analysis is possible, but for the Navier-Stokes equations the analysis is much more complex and sometimes even impossible [140]. This is why there are a lot of boundary conditions available for the Euler equations, while a less number are written for Navier-Stokes, which requires extra conditions over the viscous terms.

Non-reflecting boundary conditions must allow waves to leave the domain without reflection. The inflow condition, moreover, must define the state of the flow coming into the domain, which is known and so can be imposed. Several methods have been investigated in numerous studies. A good review on boundary conditions for compressible flow simulations was done by Colonius [44]. Broadly speaking, there are three methods to implement non-reflecting boundary conditions [169]: the method of characteristics, the use of asymptotic solutions and the addition of a buffer zone.

1.4.1 Characteristic boundary conditions

The main idea of characteristic boundary conditions is to decompose the waves crossing the boundaries into incoming and outgoing waves, and suppress the incoming ones. They were first proposed by Thompson [171], and alternative formulations were done by Giles [73, 74] and Poinsot and Lele [140].

The main advantage of this formulation is that it is valid even for nonlinear waves. Its main disadvantage is that it is essentially mono-dimensional, good in absorbing waves travelling in a direction normal

Giles [73, 74]	**Poinsot and Lele** [140]
Linearized characteristics	Non-linear characteristics
Euler equations	Navier-Stokes equations
Disturbances calculated with respect to the mean f ow	Disturbances calculated from the gradients
Knowledge of the prof le required	Knowledge of the prof le not required
Perfectly non-ref ecting	Pressure relaxation

Table 1.2 - *Main differences between the characteristic boundary conditions of Giles, and Poinsot and Lele.*

to the boundary. Consequently, it presents problems when the travelling waves are oblique with respect to the boundary, and also when there is an important mean f ow tangential to the boundary.

In the f rst version of the code written by Anaïs Guaus [82] the characteristic boundary conditions of Giles were implemented, in which the mean f ow must be estimated at all the boundaries: inf ow, radiation and outf ow. The reason is that the difference between the mean and the instantaneous f ow (i.e. the perturbation) is used to calculate the waves crossing the boundary.

Outf ow boundary conditions have the extra diff culty that, normally, the mean f ow is not known downstream, except for the pressure at inf nity. For simple cases such as channel or boundary layer f ows the mean f ow at the outf ow can be estimated, but this is not the case for more complex problems as f ows over steps or cavities. In order to solve them, an outf ow boundary condition which does not depend upon previous knowledge of the outf ow prof le is needed. For this reason, another boundary condition has been implemented at the outf ow: the characteristics formulation of Poinsot and Lele. The main differences between the formulation of Giles and that of Poinsot and Lele are outlined in table 1.2.

Firstly, the basics of the characteristic based methods are presented for a mono-dimensional problem using Euler equations. After that, the two alternatives used in this study are described for two dimensional problems.

1D characteristic boundary conditions

To describe in detail the characteristic method, it is going to be derived in its simplest case, the mono-dimensional (1D) Euler equation. Thompson's formulation [171] is used throughout. Let $U = (\rho, u, p)$ be the vector of primitive variables density, velocity and pressure, which satisfy the linearized Euler equation:

$$\frac{\partial U}{\partial t} + A\frac{\partial U}{\partial x} = 0 \tag{1.16}$$

where A is the matrix obtained from the equations of conservation of mass, momentum and energy:

$$A = \begin{bmatrix} u & \rho & 0 \\ 0 & u & 1/\rho \\ 0 & \rho c^2 & u \end{bmatrix} \tag{1.17}$$

In order to obtain the eigenvalues and eigenvectors of the system, the matrix A is decomposed as follows:

$$SAS^{-1} = \Lambda \tag{1.18}$$

where S is the matrix of eigenvectors, which represent the directions of the characteristic waves. Λ is the diagonal matrix of eigenvalues, $\Lambda_{ii} = \lambda_i$, which are the characteristic velocities:

1. $\lambda_1 = u - c$, corresponding to an acoustic wave propagating upstream.
2. $\lambda_2 = u$, corresponding to an entropy wave propagating at the speed of the f ow.
3. $\lambda_3 = u + c$, corresponding to an acoustic wave propagating downstream.

To get the amplitude of the waves crossing the boundaries, the vector of state is projected over the characteristic directions, which means multiplying the Euler equation (1.16) by S:

$$S\frac{\partial U}{\partial t} + SA\frac{\partial U}{\partial x} = S\frac{\partial U}{\partial t} + \Lambda S\frac{\partial U}{\partial x} = 0 \tag{1.19}$$

The mean f ow is assumed to be locally constant in space and time, i.e. $\frac{\partial S}{\partial t} = \frac{\partial S}{\partial x} = 0$ close to the boundary. Then equation (1.19) can be re-written as:

$$\frac{\partial SU}{\partial t} + \Lambda\frac{\partial SU}{\partial x} = 0 \tag{1.20}$$

The wave amplitudes are def ned as $V = SU$ and so:

$$\frac{\partial V}{\partial t} + \Lambda\frac{\partial V}{\partial x} = 0 \tag{1.21}$$

which is the equation of wave propagation. It is important to remember that it is assumed that the directions of propagation are constant, which is true only locally.

Def ning $\mathcal{L} = \Lambda S\frac{\partial U}{\partial x}$ as the characteristic waves, equation (1.21) is expressed as:

$$\frac{\partial V}{\partial t} + \mathcal{L} = 0 \tag{1.22}$$

where $\mathcal{L}_2$ is an entropy wave and $\mathcal{L}_1$ and $\mathcal{L}_3$ are acoustic waves, which are function of the gradients in space of the primitive variables:

$$\begin{aligned}\mathcal{L}_1 &= (u-c)\left(\frac{\partial p}{\partial x} - \rho c \frac{\partial u}{\partial x}\right) \\ \mathcal{L}_2 &= u\left(c^2\frac{\partial \rho}{\partial x} - \frac{\partial p}{\partial x}\right) \\ \mathcal{L}_3 &= (u+c)\left(\frac{\partial p}{\partial x} + \rho c \frac{\partial u}{\partial x}\right)\end{aligned} \tag{1.23}$$

For instance, for a subsonic outf ow, $\mathcal{L}_2$ and $\mathcal{L}_3$ are outgoing waves, while $\mathcal{L}_1$ is an incoming wave. Numerically, the outgoing waves depend only on information within and at the boundary, making then possible to calculate them according to equations (1.23) using a non-centered scheme. On the other hand, incoming waves depend on external data, and hence can not be computed (except in some specif c cases where an analytical far-f eld solution can be derived).

Consequently, usual outf ow conditions consist on calculating the outgoing waves using the information of the interior domain, and prescribing the amplitude of the incoming wave.

$$\begin{aligned}\mathcal{L}_{outgoing} &= \Lambda S \frac{\partial U}{\partial x} \\ \mathcal{L}_{incoming} &= \text{imposed}\end{aligned} \tag{1.24}$$

The temporal gradients of the primitive variables are thus obtained from the characteristic waves as:

$$\begin{aligned}\frac{\partial \rho}{\partial t} &= \frac{1}{c^2}\left(\frac{1}{2}(\mathcal{L}_3 + \mathcal{L}_1) + \mathcal{L}_2\right) \\ \frac{\partial u}{\partial t} &= \frac{1}{2\rho c}(\mathcal{L}_3 - \mathcal{L}_1) \\ \frac{\partial p}{\partial t} &= \frac{1}{2}(\mathcal{L}_3 + \mathcal{L}_1)\end{aligned} \tag{1.25}$$

When dealing with 2D simulations, an equivalent analysis of the system can be done, obtaining 4 characteristic waves: one entropy wave, one vorticity wave and two acoustic waves.

Linear Relaxation Method

As it has been explained, a common way to treat incoming waves in characteristic methods is to impose its amplitude. A natural way to treat a subsonic outf ow consists on totally suppress the incoming wave, i.e. $\mathcal{L}_{incoming} = 0$. This procedure is called perfectly non-ref ecting boundary and it has been used by Thompson [171] and Giles [73]. This method has been proved to be adequate to control acoustic waves (when they are perpendicular to the boundary) but not the mean f ow. Physically, the mean pressure is imposed by the far-f eld state, and numerically it is fed back into the domain through the incoming wave.

If it is totally suppressed, this information is not fed back and the flow might not retain a constant mean pressure.

One possible way to solve this problem is to calculate an analytical solution for the incoming wave. This is possible in certain academic configurations, yet it is difficult or impossible in most of the cases. An alternative solution, more practical even though less accurate, consists on applying relaxation over the static pressure difference. This method is called Linear Relaxation Method (LRM).

This approach was first proposed by Rudy and Strikwerda [154], who added the correction term $K(p - p_\infty)$ into the energy equation to simulate a non-reflecting subsonic outflow boundary condition. An extensive study of the coefficient K showed that it depends on the Mach number M and a characteristic length of the domain l, in the form:

$$K = \sigma(1 - M^2)c/l \tag{1.26}$$

where an optimal value σ was found analytically to be around 0.27, even though in numerical simulations a better result was obtained with $\sigma \simeq 0.58$ [154].

Poinsot and Lele [140] derived two-dimensional characteristic boundary conditions for Navier-Stokes equations. In their approach, a subsonic outflow is not defined as perfectly non-reflecting, but it allows certain reflection in order to fed back the far-field pressure into the domain. This is done by setting the amplitude of the incoming wave as proportional to the static pressure difference:

$$\mathcal{L}_{incoming} = K(p - p_\infty) = \sigma(1 - M^2)(c/l)(p - p_\infty) \tag{1.27}$$

The coefficient K is defined as by Rudy and Strikwerda [154] in equation (1.26), but Poinsot and Lele chose $\sigma = 0.25$.

In simple problems as a Poiseuille channel flow, an analytical solution for the incoming wave can be easily derived, using for example asymptotic methods. In that case, the exact solution is added to equation (1.27) in order to ensure a good matching of derivatives:

$$\mathcal{L}_{incoming} = K(p - p_\infty) + \mathcal{L}^{exact}_{incoming} \tag{1.28}$$

Selle *et al.* [157] investigated the relaxation coefficient K when using the characteristic approach of Poinsot and Lele for a subsonic non-reflecting outflow. According to their study, a cutoff frequency can be defined from the relaxation coefficient $f_c = K/4\pi$. This cutoff frequency is interpreted as the frequency below which the boundary condition will not allow the waves to leave the domain.

Furthermore, there is a minimum value σ_{min} which prevents a drift in the mean values. The minimum value of σ is not fixed by acoustics, and it strongly depends on the computational parameters. Selle *et al.* suggest that a value under 0.1 may increase convergence time and it may prevent the simulation to reach a steady state.

2D characteristic boundary conditions of Giles

The mono-dimensional characteristic formulation of Thompson [171] has been used to describe in detail the method. Even though this method is also available in two dimensions, for this investigation two other characteristic formulations have been implemented and compared.

The first one is an alternative formulation, more simple, proposed by Giles [73] and derived for the Euler equations. In this approach, the 2D linearized Euler equations are normalized by the density and the speed of sound. The main difference respect to Thompson's method consists on the way to obtain the values of the outgoing waves. While Thompson proposed to calculate them from the spatial gradients (eq. (1.23)), Giles considers disturbances respect to the mean flow which has been used to linearize the equations.

Then, the exact formulation of the characteristic outgoing waves for the 2D equations is (using Giles' notation):

$$\begin{aligned} \mathcal{L}_1 &= \delta p - c^2 \delta \rho \\ \mathcal{L}_2 &= \rho c \delta v \\ \mathcal{L}_3 &= \delta p + \rho c \delta u \\ \mathcal{L}_4 &= \delta p - \rho c \delta u \end{aligned} \tag{1.29}$$

where $\delta\rho, \delta u, \delta v, \delta p$ are the disturbances with respect to the mean flow. $\mathcal{L}_1$ is an entropy wave, $\mathcal{L}_2$ is a vorticity wave, $\mathcal{L}_3$ is an acoustic wave traveling downstream and $\mathcal{L}_4$ is an acoustic wave propagating upstream.

Giles method is perfectly non-reflecting and hence incoming waves are imposed to be zero. Once the characteristic waves are calculated, they are used to recover the disturbances of the primitive variables using:

$$\begin{aligned} \delta\rho &= \frac{\mathcal{L}_3 + \mathcal{L}_4}{2c^2} - \frac{\mathcal{L}_1}{c^2} \\ \delta u &= \frac{\mathcal{L}_3 - \mathcal{L}_4}{2\rho c} \\ \delta v &= \frac{\mathcal{L}_2}{\rho c} \\ \delta p &= \frac{\mathcal{L}_3 + \mathcal{L}_4}{2} \end{aligned} \tag{1.30}$$

The main advantage of this method compared to the one of Thompson [171] is that it is simpler to implement and it is less computationally expensive. The main drawback is that a previous knowledge of the mean field at the boundary is required, and in many cases they are unknown.

2D characteristic boundary conditions of Poinsot and Lele

The second characteristic boundary condition considered is an extension to the Navier-Stokes equations of Thompson's method [171], which was proposed by Poinsot and Lele [140]. This formulation can be used to implement any far-field boundary, even though here it has only been used for the outflow boundary condition.

Consider the 2D Navier-Stokes equations:

$$\frac{\partial U}{\partial t} = -\frac{\partial F^c}{\partial x} - \frac{\partial G^c}{\partial y} + \frac{\partial F^v}{\partial x} + \frac{\partial G^v}{\partial y} \tag{1.31}$$

where $U = (\rho, \rho u, \rho v, \rho e)$ are the unknown conservative variables of the system. F^c and G^c represent the inviscid fluxes and F^v and G^v the viscous fluxes. Considering a flow moving in x-direction, the characteristic analysis [171] is applied to modify the hyperbolic terms of equation (1.31) corresponding to waves propagating in this direction, i.e. the convective fluxes F^c.

Moreover, for a subsonic outflow using Navier-Stokes equations 2 viscous conditions are necessary: the gradient of the tangential viscous stresses and the normal heat flux must be zero at the boundary, i.e. $\partial\tau_{12}/\partial x = \partial q_1/\partial x = 0$.

Hence the system can be re-written as:

$$\begin{aligned}
\frac{\partial \rho}{\partial t} &+ d_1 + \frac{\partial \rho v}{\partial y} \\
&= 0 \\
\frac{\partial \rho u}{\partial t} &+ u d_1 + \rho d_3 + \frac{\partial \rho u v}{\partial y} \\
&= \frac{\partial \tau_{11}}{\partial x} + \frac{\partial \tau_{12}}{\partial y} \\
\frac{\partial \rho v}{\partial t} &+ v d_1 + \rho d_4 + \frac{\partial \rho v^2}{\partial y} + \frac{\partial p}{\partial y} \\
&= \frac{\partial \tau_{22}}{\partial y} \\
\frac{\partial \rho e}{\partial t} &+ \frac{1}{2}\left(u^2 + v^2\right) d_1 + \frac{d_2}{\gamma - 1} + \rho u d_3 + \rho v d_4 + \frac{\partial [(\rho e + p) v]}{\partial y} \\
&= \frac{\partial u \tau_{11}}{\partial x} + \tau_{12}\frac{\partial v}{\partial x} + \frac{\partial u \tau_{12}}{\partial y} + \frac{\partial v \tau_{22}}{\partial y} - \frac{\partial q_2}{\partial y}
\end{aligned} \tag{1.32}$$

which contains the derivatives in y, the non-zero viscous terms and d_i, with $i = 1, ..., 4$, where:

$$
\begin{aligned}
d_1 &= \frac{\partial \rho u}{\partial x} \\
d_2 &= u\frac{\partial p}{\partial x} + \rho c^2 \frac{\partial u}{\partial x} \\
d_3 &= u\frac{\partial u}{\partial x} + \frac{1}{\rho}\frac{\partial p}{\partial x} \\
d_4 &= u\frac{\partial v}{\partial x}
\end{aligned}
$$

The vector d_i is given by the characteristic analysis performed for the system $\partial U/\partial t = -\partial F^c/\partial x$, and is function of the characteristic waves as:

$$
\begin{aligned}
d_1 &= \frac{1}{c^2}\left(\frac{1}{2}(\mathcal{L}_4 + \mathcal{L}_1) + \mathcal{L}_2\right) \\
d_2 &= \frac{1}{2}(\mathcal{L}_4 + \mathcal{L}_1) \\
d_3 &= \frac{1}{2\rho c}(\mathcal{L}_4 - \mathcal{L}_1) \\
d_4 &= \mathcal{L}_3
\end{aligned}
$$

where $\mathcal{L}_1$ is an acoustic wave propagating upstream, $\mathcal{L}_2$ is an entropy wave, $\mathcal{L}_3$ is a vorticity wave and $\mathcal{L}_4$ is an acoustic wave traveling downstream.

Using an analogy with the derivation detailed for the 1D case, the vector d_i corresponds to the temporal derivatives of the primitive variables (ρ, p, u, v). The characteristic waves in 2D are given by:

$$
\begin{aligned}
\mathcal{L}_1 &= (u - c)\left(\frac{\partial p}{\partial x} - \rho c \frac{\partial u}{\partial x}\right) \\
\mathcal{L}_2 &= u\left(c^2\frac{\partial \rho}{\partial x} - \frac{\partial p}{\partial x}\right) \\
\mathcal{L}_3 &= u\frac{\partial v}{\partial x} \\
\mathcal{L}_4 &= (u + c)\left(\frac{\partial p}{\partial x} + \rho c \frac{\partial u}{\partial x}\right)
\end{aligned}
$$

For a subsonic outf ow $\mathcal{L}_1$ is the only incoming wave, i.e. the only one which must be imposed and not calculated from the spatial gradients. In this approach, a LRM is applied according to equation (1.27).

1.4.2 Asymptotic boundary conditions

This method uses the far-f eld asymptotic expression of the linearized Euler equations to simulate the boundary conditions. Tam and Webb [170] derived asymptotic boundary conditions for uniform f ows,

which were extended to non-uniform flows by Tam and Dong [168]. This approach is formulated in cylindrical coordinates, where the origin is usually the center of the noise source but it has been shown that it can be arbitrarily fixed. Its main advantage is that it is multidimensional and the problems at the corners are reduced due to the use of cylindrical coordinates.

The formulation of Tam and Dong is [168]:

$$\frac{1}{V_g}\frac{\partial}{\partial t}\begin{pmatrix}\rho\\u\\v\\p\end{pmatrix}+\left(\frac{\partial}{\partial r}+\frac{1}{2r}\right)\begin{pmatrix}\rho-\bar{\rho}\\u-\bar{u}\\v-\bar{v}\\p-\bar{p}\end{pmatrix}=0 \tag{1.33}$$

where $(\bar{\rho},\bar{u},\bar{v},\bar{p})$ represents the far-field at the boundary, in the absence of perturbations, and V_g is the group speed of the acoustic waves, defined as:

$$V_g=\bar{\mathbf{u}}\cdot\mathbf{e_r}+\sqrt{\bar{c}^2-(\bar{\mathbf{u}}\cdot\mathbf{e}_\theta)^2}\quad\text{with}\quad\begin{cases}\mathbf{e_r}=(\cos\theta,\sin\theta)\\\mathbf{e}_\theta=(-\sin\theta,\cos\theta)\\\bar{\mathbf{u}}=(\bar{u},\bar{v})\end{cases} \tag{1.34}$$

where $\bar{c}$ is the averaged speed of sound.

This approach was implemented for all the non-reflecting boundaries during the development of the single block version of the code, and it was found to give very similar results to those from the characteristic method [82, 149]. However, its formulation in cylindrical coordinates made complicated its application in multi-block geometries, and hence it was not further used.

1.4.3 Buffer zone

Even with non-reflecting boundary conditions sometimes it is not possible to avoid reflections, especially at the corners of the computational domain. A common method used to suppress undesired oscillations is the addition of a buffer zone. A buffer zone, or absorbing layer, is a finite region added outside the computational domain where the flow physics are modified. They are used to either enhance the efficiency of a boundary condition or to obviate the need for a complex boundary condition.

In the present computations a buffer zone consisting on a stretched mesh with increased cell length near the boundary and a 4^{th} order compact filter proposed by Lele [119] is used:

$$\alpha\hat{U}_{i-1}+\hat{U}_i+\alpha\hat{U}_{i+1}=aU_i+\frac{b}{2}\left(U_{i+1}-U_{i-1}\right)+\frac{c}{2}\left(U_{i+2}-U_{i-2}\right) \tag{1.35}$$

where U are the non-filtered values, $\hat{U}$ are the filtered values, and the coefficients are:

$$a=\frac{1}{8}(5+6\alpha),\quad b=\frac{1}{2}(1+2\alpha),\quad c=-\frac{1}{8}(1-2\alpha) \tag{1.36}$$

There are other ways to implement a buffer zone. For instance, Colonius *et al.* [48] proposed a filter, Freund [66] used a forcing term which can be added in the right-hand-side of the equations and Wasistho *et al.* [178] damped directly the disturbances calculated from a reference flow.

1.5 Wall boundary conditions

The formulation of an appropriate wall boundary condition in high-order-schemes is still an open problem, since common formulations for low-order schemes might lead to numerical instabilities when applied to high-order schemes. In low-order schemes, the derivatives of the Euler equation are approximated by a first-order finite difference scheme, preserving the same order as the original partial differential equations (PDE). In high-order schemes, the order of the resulting finite difference equation is higher than the order of the original PDE, and hence it can support solutions without a counterpart in the original system. This unphysical solutions are called spurious solutions, and they can be generated by the initial conditions or surface discontinuities as a wall.

Several solutions have been proposed to avoid creating these unphysical solutions at a solid boundary:

Ghost cells: They are non-physical points used for numerical purposes, placed outside the physical domain in order to simulate the reflection at the solid boundary. They are further described in §1.5.2.

Characteristics: The characteristic methods described in §1.4.1 can be used to implement a wall by considering a perfectly reflecting boundary. As in the case of non-reflecting boundaries, they might present problems if the waves are not perpendicular [140].

Robust formulation over the convective fluxes: In this approach the solid condition is applied by estimating the convective fluxes at the wall [75], as explained in §1.5.1.

Impedance mismatched method: From classic acoustics theory, a wave in a fluid medium which encounters a second medium is partially reflected into the first medium and transmitted in the second one, where the ratio reflection/transmission depends on the characteristic impedance. Thus a solid boundary can be numerically simulated with a region in which the characteristic impedance is set to a much higher value than the fluid region, in order to reflect the impinging waves [34].

Solid boundaries in this investigation are modelled as isothermal and can be either slip or non-slip. In the first version of the code written by Anaïs Guaus [82] a robust formulation proposed by Gloerfelt [75] was implemented and validated for single block problems. In order to improve the code, an alternative wall boundary condition with ghost cells was implemented as part of this thesis.

1.5.1 Gloerfelt's wall boundary condition

This method consists on estimating the convective fluxes normal to the wall. If an horizontal wall is considered, the x-direction is tangential to the wall, y-direction is normal to the wall, and the convective fluxes in conservative form are:

$$\begin{aligned}
\frac{\partial G^c_\rho}{\partial y} &= \rho\frac{\partial v}{\partial y} + v\frac{\partial \rho}{\partial y} \\
\frac{\partial G^c_{\rho u}}{\partial y} &= \rho u\frac{\partial v}{\partial y} + v\frac{\partial \rho u}{\partial y} \\
\frac{\partial G^c_{\rho v}}{\partial y} &= \frac{\partial p}{\partial y} + v\frac{\partial \rho v}{\partial y} + \rho v\frac{\partial v}{\partial y} \\
\frac{\partial G^c_{\rho e}}{\partial y} &= \left(\frac{\gamma}{\gamma-1}p + \frac{\rho u}{2}\right)\frac{\partial v}{\partial y} + v\left(\frac{\gamma}{\gamma-1}\frac{\partial p}{\partial y} + \frac{\partial}{\partial y}\left(\frac{u+v}{2}\right)\right)
\end{aligned} \tag{1.37}$$

For a slip wall (used when solving the Euler equations), $v = 0$ and the pressure gradient normal to the wall is imposed to be zero ($\partial p/\partial y = 0$). Applying all these conditions the convective fluxes in conservative form normal to the wall can be predicted as:

$$\begin{aligned}
\left.\frac{\partial G^c_\rho}{\partial y}\right|_w &= \rho\frac{\partial v}{\partial y} \\
\left.\frac{\partial G^c_{\rho u}}{\partial y}\right|_w &= \rho u\frac{\partial v}{\partial y} \\
\left.\frac{\partial G^c_{\rho v}}{\partial y}\right|_w &= 0 \\
\left.\frac{\partial G^c_{\rho e}}{\partial y}\right|_w &= \left(\frac{\gamma}{\gamma-1}p + \frac{\rho u}{2}\right)\frac{\partial v}{\partial y}
\end{aligned} \tag{1.38}$$

where the subscript w denotes the wall position, and $\partial v/\partial y$ is obtained with a second-order approximation:

$$\left.\frac{\partial v}{\partial y}\right|_w = \frac{4v_{w+1} - v_{w+2}}{2\Delta y} \tag{1.39}$$

For a non-slip wall, the condition $u = 0$ must be added in addition to the conditions for a slip wall. In the first version of the code these boundary conditions were applied over the total fluxes $G^c + G^v$. The algorithm has been modified in order to apply them only over the convective fluxes G^c. Both implementations are tested and compared in one of the validation test cases, §2.2.1.

Both isothermal and adiabatic walls have been implemented. In this formulation, the isothermal condition is directly imposed by calculating the density at the given temperature at the wall at the end of each iteration. To implement an adiabatic wall, $\partial T/\partial y = 0$, which implies $q_y = 0$. This condition is directly applied when calculating the viscous flux $G^v_{\rho e}$ (the only one where q_y appears).

1.5.2 Wall boundary condition with ghost cells

The approach proposed by Gloerfelt [75] gives satisfactory results for single-block problems, as is it to be shown in the validation test cases from chapter §2. However, it presents problems in simulations of flows over surface discontinuities due to the coupling with the dynamic block derivation described in section §1.6. In these simulations, high numerical instabilities appear near the upper corners due to the corner points. The proposed solution to this problem consists on the implementation of an alternative wall boundary condition with ghost cells.

There are different ways to implement boundary conditions with ghost cells [75]:

1. Place the first line of points on the wall, and the ghost cells inside the wall, as shown in figure 1.2(a).

2. Place the first line of points in the interior domain, and the ghost cells inside the wall, as shown in figure 1.2(b).

3. Use the minimum number of ghost cells, as proposed by Tam and Dong [167]. For a non-viscous flow, $v = 0$, which can be interpreted as the pressure done by the wall over the fluid. The idea is to use a ghost cell to calculate the pressure and compute the other variables from the values at the interior domain. For a viscous flow, $u = v = 0$, and a part from calculating the pressure with a ghost cell, another condition will be necessary, which can be interpreted as a tangential shear stress applied by the wall on the fluid. So in this case, the pressure and another variable representing the shear stress are computed with ghost cells and the other variables normally using a non-centered boundary scheme.

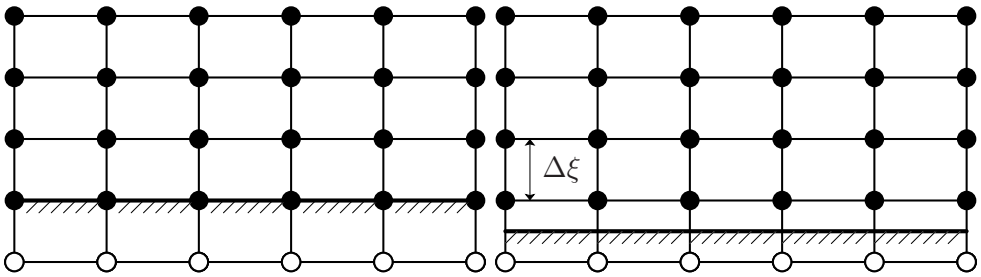

(a) Ghost cells with points on the wall (b) Ghost cells without points on the wall

Figure 1.2 - *Representation of the ghost cells method. Interior points* •*, ghost cells* ○

Since the wall boundary condition without ghost cells presents high instabilities near the upper corner due to the corner point, a ghost cells method without any point at the wall is selected. The wall is considered to be at the same distance from the ghost cell and the first interior point, as shown in figure 1.2(b).

The ghost cells method has been used to implement an isothermal wall. The isothermal condition is directly applied by imposing the temperature of the wall at the ghost cell, and compute the corresponding density from the equation of state for an ideal gas. The non-slip condition consists on imposing the

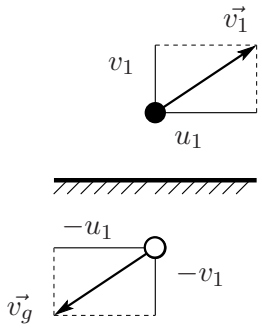

Figure 1.3 - *Determination of the velocity vector at the ghost cell. Interior points ●, ghost cells ○*

velocities u and v to be zero at the wall, which is done by mirroring them from the first interior point to the ghost cell, as shown in figure 1.3.

To define the pressure at the wall, the gradient of pressure in the direction normal to the wall is imposed to be zero as it was done by Gloerfelt [75]. At the grid points which are closer to the wall the flow locally behaves like a boundary layer, so $\partial p/\partial y = 0$ can be considered, even in separated flows. The equations used to estimate the flow state at the ghost cells in an horizontal wall are:

$$\begin{aligned} u_g &= -u_1 \\ v_g &= -v_1 \\ \left.\frac{\partial p}{\partial y}\right|_w &= 0 \\ \rho_g &= \frac{p_g}{rT_w}. \end{aligned} \tag{1.40}$$

where subscript w denotes a condition at the wall, 1 at the first interior point and g at the ghost cell, and r is the universal gas constant.

In order to obtain the pressure gradient two different schemes have been used. The first one is a second-order classic explicit centered scheme, in which $p_g = p_1$.

The second one is a fourth-order non-centered scheme with a five-point stencil that has been derived from a Taylor expansion to obtain the pressure gradient at the wall:

$$\left.\frac{\partial p}{\partial y}\right|_w = a_g p_g + a_1 p_1 + a_2 p_2 + a_3 p_3 + a_4 p_4 = 0 \tag{1.41}$$

where subscript g denotes the ghost cell and subscripts $1, ..., 4$ denote the 4 interior points adjacent to the wall. The Taylor expansion of the pressure at the wall is:

$$p(y + h_\alpha) = p(y) + h_\alpha p'(y) + \frac{h_\alpha^2}{2!}p''(y) + \frac{h_\alpha^3}{3!}p'''(y) + \frac{h_\alpha^4}{4!}p''''(y) \tag{1.42}$$

where the wall is placed at $y = 0$, $\alpha = g, 1, ..., 4$ and:

$$\begin{aligned} h_g &= (-1/2)\Delta\xi \\ h_1 &= (1/2)\Delta\xi \\ h_2 &= (3/2)\Delta\xi \\ h_3 &= (5/2)\Delta\xi \\ h_4 &= (7/2)\Delta\xi \end{aligned}$$

for a uniform equidistant grid in *y*-direction with spatial increment $\Delta\xi$ as shown in f gure 1.2(b). Solving the equation system gives the values of the coeff cients $a_g, ..., a_4$:

$$\left.\frac{\partial p}{\partial y}\right]_w = \frac{1}{48\Delta\xi}(22p_g - 17p_1 - 9p_2 + 5p_3 - p_4) \tag{1.43}$$

which implies that the pressure at the ghost cell can be calculated as:

$$p_g = \frac{1}{22}(17p_1 + 9p_2 - 5p_3 + p_4) \tag{1.44}$$

1.6 Multi-block treatment

The simulation of f ows over surface discontinuities, like steps or cavities, requires different blocks to create the geometry. In these complex conf gurations, it is important to implement good connectivity conditions between the different blocks. Here a numerical method proposed by Guaus [82] to calculate the derivatives in multi-block conf gurations is presented.

1.6.1 Dynamic block derivation

A common inter-block condition consists on copying the last line of information from one block to the adjacent block, as shown in f gure 1.4. The f rst column of points of block 2, represented by white circles, are copied next to the last column of block 1, represented by black circles. Then, the derivative of the f uxes in block 1 are computed like it were a single block problem. The same procedure is applied to block 2, where the last column of points of block 1 is added in order to get the derivatives of the f uxes.

Once the derivatives have been calculated for all the blocks, the right-hand-side of the equation (1.1) is calculated separately for each block, without taking into account the extra columns used for the derivatives. After that, the left-hand-side of equation (1.1) is updated according to the Runge-Kutta integration and f nally the boundary conditions (non-ref ecting and solid) are applied.

The complexity of the problem increases with the existence of a corner. In that case, a part from copying the last rows and columns, it is important to give the adequate information to the corner point in order to simulate correctly the f ow at the separation point.

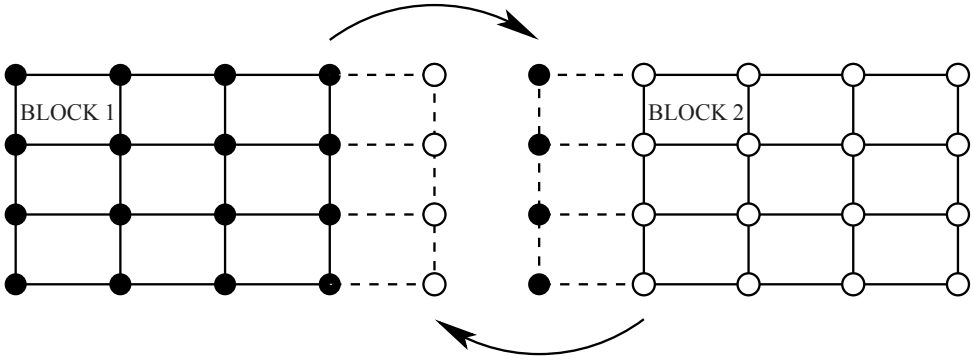

Figure 1.4 - *Common connectivity condition between two blocks*

An alternative method to compute the derivatives in multi-block conf gurations described in the Appendix A of [82] is implemented. It consists on the def nition of different block conf gurations according to the directions of the Cartesian coordinates. To better illustrate the dynamic block derivation method, the block distribution shown in f gure 1.5 for a backward-facing-step is used as an example.

Figure 1.5(a) shows the block conf guration which def nes the geometry and is used throughout the computational simulation. In order to get the derivatives in *x*-direction, the alternative distribution of f gure 1.5(b) is used, where only two blocks are present. Equivalently, to compute the derivatives of the f uxes in *y*-direction the conf guration of f gure 1.5(c) is considered. The main idea is to compute the derivatives of the f uxes in each direction like it were a single block, and no accuracy between blocks is lost.

The re-distribution of the blocks to get the derivatives is done automatically by the code, and it can handle any kind of rectangular block conf guration (backward-facing step, forward-facing-step, cavity,

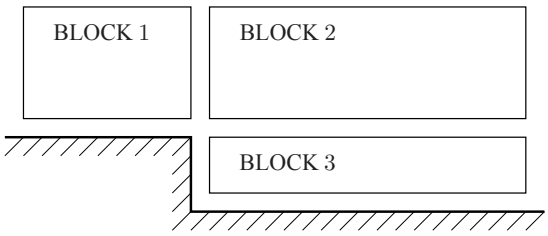

(a) Block distribution to def ne geometry

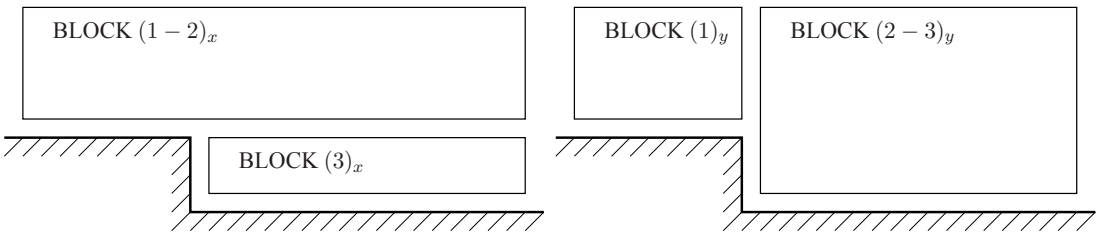

(b) Block distribution for *x*-derivatives

(c) Block distribution for *y*-derivatives

Figure 1.5 - *Dynamic block derivation*

channel with an interior rectangular obstacle, etc.). It is only required that adjacent blocks have the same physical dimensions and the same grid points on their adjacent edge.

1.6.2 Dynamic block derivation with ghost cells

The ghost cells method has been integrated into the code and coupled with the dynamic block derivation. An example of block conf guration is shown in f gure 1.6. The complexity of the problem consists in matching the block sizes in order to join them to compute the derivatives. Consequently, the ghost cells are not part of the blocks, but are def ned as independent vectors related with them, as shown by • in f gure 1.6(a).

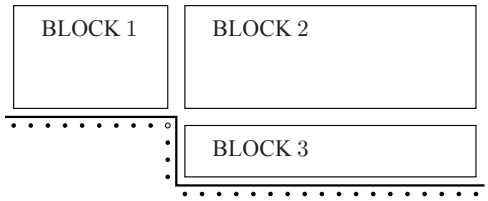

(a) Block distribution to def ne geometry

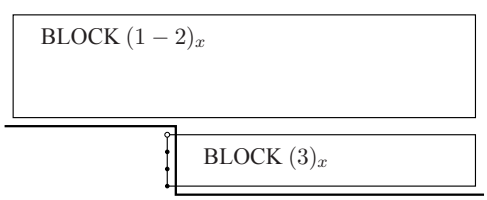

(b) Block distribution for *x*-derivatives

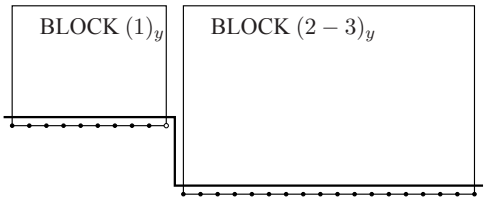

(c) Block distribution for *y*-derivatives

Figure 1.6 - *Dynamic block derivation with the use of ghost cells. Interior domain (—), ghost cells •, ghost cell at the corner ∘*

The block distribution to calculate the derivatives in *x*-direction is shown in f gure 1.6(b). Blocks 1 and 2 are computed together as explained in §1.6.1, and the ghost cells related to the horizontal wall on the south of block 1 are not considered, since they do not take part in the derivatives in this direction. On the other hand, block 3 has a vertical wall on the west, and the corresponding ghost cells are necessary to calculate the derivatives in *x*-direction. In order to use the ghost cells in the derivation of the f uxes, they are added to block 3 in the same way that blocks 1 and 2 are joined.

An equivalent treatment is done to the blocks to calculate the derivatives in *y*-direction. In this case, the ghost cells related to horizontals walls are required to correctly compute the derivatives. Blocks 1 and 3 have a solid boundary on the south, so the ghost cells vectors are added to them. Blocks 2 and 3 are put together as explained in the previous subsection.

The addition of blocks and ghost cells is done automatically by the program which can handle any rectangular block conf guration with walls in any boundary (east, west, north or south). The use of ghost cells is also possible when dealing with a single block problem, since the ghost cell vector is independent and can be added to any block.

Specif c conditions must be added into the code regarding the corners. For a backward-facing step,

for instance, there is one ghost cell which is common for the blocks 1 and 3 (represented by a circle ∘ in figure 1.6(a)). In this case, in order to impose the flow coming from the inflow, this ghost cell is calculated using the variables from block 1 and ignoring the values from block 3. For a forward-facing step, an equivalent treatment is done, giving preference to the block were the outflow is located. The same conditions are applied to a cavity flow, which is the combination of a backward-facing and a forward-facing steps.

1.7 Conclusions

In summary, the numerical method used consists on a 6^{th} order compact scheme with a progressive-regressive formulation for the spatial discretization of convective fluxes [108], a 4^{th} order explicit scheme for the viscous fluxes and a classic 4^{th} order Runge-Kutta scheme for the time-marching. The use of a progressive-regressive formulation, in which the sequence forward-backward is inverted at each temporal iteration, avoids the use of a filter or artificial damping since it naturally suppresses high-frequency oscillations of numerical origin.

The characteristic boundary conditions of Giles [73, 74] are used for the non-reflecting boundaries, and in addition the characteristic formulation of Poinsot and Lele [140] is implemented at the outflow. The proposal of Poinsot and Lele does not require previous knowledge of the mean flow at the outflow, and it considers non-linearities of the flow and viscous effects. Wall boundary conditions with ghost cells have been implemented, in which there is no point at the wall. This formulation avoids the singularity of having one point at the corner.

The problem of the multi-block derivation is solved by defining different configurations according to the direction in which the derivative is calculated. The ghost cells have been integrated into the dynamic block derivation and any rectangular multi-block geometry can be simulated.

Chapter 2

Validation test cases

Cas tests de validation

Il est très important de valider unes à unes les différentes méthodes numériques utilisées, durant les phases de développement et d'amélioration du code de calcul. Le but est d'avoir un outil numérique approprié pour l'étude du bruit émis par un écoulement laminaire au-dessus d'une cavité, dans lequel plusieurs caractéristiques entrent en jeu : l'aéroacoustique, les effets visqueux et la géométrie multi-blocs. Pour chacunes de ces caractéristiques, plusieurs cas tests de validation ont été réalisés, lesquels sont listés dans le tableau 2.1.

Cas tests aéroacoustiques

Cinq cas tests de complexité croissante ont été implémentés afin de tester l'aptitude de notre code à réaliser des études acoustiques. Leur objectif est de valider le caractère non dissipatif et non diffusif des schémas de discrétisation, ainsi que les conditions aux limites non réfléchissantes et de parois solides, et le traitement des coins. Dans tous les cas testés (sauf indication contraire), le nombre de Mach de l'écoulement libre est de $M = 0.5$, et les équations simulées sont les équations d'Euler sur un maillage uniforme.

Les deux premiers cas consistent à simuler les propagations d'une onde acoustique, d'une onde d'entropie et d'une onde de vorticité dans un écoulement moyen uniforme suivant la direction x (cas §2.1.1), puis uniforme suivant les directions x et y (cas §2.1.2), et cela sans la présence de paroi solide. L'onde acoustique se propage à la vitesse ($u_\infty + c$) en aval et ($u_\infty - c$) en amont, tandis que les deux autres ondes sont convectées à la vitesse de l'écoulement u_∞. Les résultats de ces deux cas tests ont été comparés aux solutions analytiques données lors du premier workshop sur les problèmes de référence en aéroacoustique numérique [89].

Les deux cas tests suivants mettent en jeu la reflexion sur une paroi solide d'une onde acoustique dans un écoulement uniforme (cas §2.1.3) puis en présence d'une couche limite (cas §2.1.4). Le cas test §2.1.3 a été validé en utilisant la solution analytique donnée par [89]. Le cas test §2.1.4 est une extension du cas précédent §2.1.3 aux équations de Navier-Stokes. Etant donné la présence d'une couche limite à la paroi solide, le maillage a été raffiné au voisinage de la paroi. Enfin, aucune solution analytique étant

disponible pour ce cas, nous avons comparé nos résultats au cas fluide parfait, et nous avons également comparé les résultats obtenus pour différentes conditions aux limites de parois solides.

Le dernier cas test consiste en une double réflexion d'une onde acoustique. Ce problème, inspiré des cas §2.1.1 et §2.1.3, implique la présence de deux parois solides, en bas et à droite du domaine, formant ainsi un coin. Une solution analytique a été calculée afin de la comparer aux résultats obtenus.

Les cas tests §2.1.1, §2.1.3 et §2.1.5 ont été réalisés en collaboration avec l'Université de Leicester sur un programme concernant l'étude de schémas d'ordre élevé pour l'aéroacoustique numérique, et les resultats ont été publiés dans Rona et al. [149].

Cas tests visqueux

Le but de ces tests était de valider le code de calcul dans le cas de fluide visqueux. Nous nous sommes en particulier intéressés aux conditions aux limites de sortie d'écoulement et de paroi solide.

Le premier problème considéré est celui d'une couche limite sur une paroi plane sans gradient de pression. L'écoulement est considéré compressible avec un nombre de Mach de $M = 0.2$, et le régime de l'écoulement est laminaire avec un nombre de Reynolds basé sur l'épaisseur de couche limite de $Re_\delta = 516$. Le domaine de calcul est rectangulaire, avec un maillage uniforme dans la direction principale de l'écoulement, et raffiné à la paroi suivant la direction normale. Les résultats ont été comparés à la solution numérique de l'équation de similarité de Blasius.

Le second problème considéré est celui d'un écoulement de Poiseuille en canal plan avec un nombre de Mach de $M = 0.1$. Le nombre de Reynolds basé sur la demi-hauteur de canal h est de $Re_h = 15$, l'écoulement est donc laminaire et les effets visqueux sont par conséquent importants. Le canal considéré pour cette étude a une longueur de $10h$, et le maillage est uniforme. Les résultats obtenus sont comparés aux profils analytiques de vitesse u et de température, ainsi qu'au gradient de pression analytique.

Cas tests multi-blocs

Dans tous les cas tests précédents nous avons simulé des écoulements dans des géométries de type mono-bloc. Afin de parfaire la validation de notre code de simulation numérique, une dernière étape consiste donc à simuler un écoulement dans une géométrie multi-blocs, et de tester ainsi la dérivation inter-blocs et le traitement des coins. Nous avons pour celà considéré un écoulement 2D de fine couche limite laminaire à nombre de Mach de $M = 0.1$, qui arrive sur une marche descendante. Le maillage est raffiné au voisinage de la marche dans les deux directions horizontale et verticale, ainsi qu'au voisinage des parois. Une zone 'buffer', composée d'un maillage étiré et d'un filtre tel que proposé par Lele [119], a été ajouté en limite de sortie d'écoulement.

La couche limite incidente se sépare au coin supérieur de la marche descendante formant, à l'arrière de la marche, une zone de recirculation primaire et un plus petit vortex secondaire au coin inférieur de la marche. Le vortex primaire devient de plus en plus grand, jusqu'à ce qu'il se détache du coin supérieur et soit convecté en aval. A ce moment là, le second vortex est attaché à la couche limite incidente, devenant le vortex primaire alors qu'un nouveau vortex secondaire est apparu au coin inférieur de la marche. Et le processus continue ainsi de manière périodique. Les résultats obtenus ont été comparés à ceux obtenus dans la même configuration 2D de marche descendante par le logiciel commercial FLUENT (cas Navier-Stokes incompressible).

Résultats et conclusions

Nous avons montré les propriétés non dispersive et non dissipative des schémas numériques utilisés, grace aux tests §2.1.1, §2.1.2, §2.1.3 et §2.1.5. Dans tous ces cas tests, les résultats obtenus coïncident parfaitement avec les solutions analytiques à l'intérieur du domaine de calcul, même dans le cas d'ondes qui se propagent dans une direction faisant un certain angle avec la grille cartésienne du maillage. Aucun filtrage supplémentaire n'a été nécessaire.

Les conditions aux limites non réfléchissantes ont été également testées au travers des problèmes §2.1.1, §2.1.2 et §2.2.2. La condition aux limites caractéristique de Giles [73, 74] a donné de très bons résultats, en particulier dans le cas d'ondes traversant perpendiculairement les frontières du domaine de calcul (paragraphe §2.1.1), avec cependant de très petites déviations en présence d'un écoulement moyen tangentiel à la frontière (§2.1.2). La condition aux limites de type asymptotique de Tam et Dong [168], testée uniquement pour le problème §2.1.1, présente des résultats identiques à ceux obtenus avec une formulation de type caractéristique.

La formulation de condition aux limites caractéristique de Poinsot et Lele [140] donne les mêmes résultats que la formulation de Giles pour les cas tests aéroacoustiques §2.1.1 et §2.1.2. L'écoulement de canal plan du cas test §2.2.2 a été utilisé pour étudier l'influence du coefficient de relaxation σ, et nous avons trouvé que $\sigma = 0.58$ est le coefficient qui donne les profils de vitesse les plus proches des profils de Poiseuille avec un gradient de pression correct. L'efficacité de la condition aux limites est ainsi validée, mais la valeur du coefficient σ optimum nécessite une nouvelle étude à chaque nouveau cas étudié.

Les conditions aux limites aux parois solides ont été testées pour des applications aéroacoustiques dans les cas tests §2.1.3, §2.1.4 et §2.1.5. Deux formulations, celle de Gloerfelt [75] et celle des points de maillage 'fantômes' ('ghost cells' de 2^{nd} et $4^{ème}$ ordre), ont été validées, les résultats obtenus étant quasi identiques aux solutions analytiques. Pour le cas §2.1.4, nous avons pu expliquer physiquement les différences avec la solution analytique du cas Euler par les effets visqueux. Enfin, la double réflexion de paroi testée au paragraphe §2.1.5 montre la bonne performance du code de calcul dans le traitement des coins.

Les problèmes §2.2.1 et §2.2.2 ont été utilisés pour tester l'efficacité de la condition aux parois solides pour des écoulements à très faible nombre de Reynolds. La condition aux limites de Gloerfelt doit être appliquée sur les flux convectifs uniquement, plutôt que sur la totalité des flux, et il a été en effet prouvé dans §2.2.1 qu'elle donne ainsi des résultats plus précis. Les deux types de conditions aux limites, Gloerfelt et 'ghost cells', donnent de bons résultats. Cependant, dans le cas d'un écoulement de canal plan, il est à noter que le schéma décentré du $4^{ème}$ ordre utilisé dans la méthode des 'ghost cells' crée des oscillations de très petites amplitudes de la composante normale de vitesse.

Pour la simulation d'un écoulement au-dessus d'une cavité rectangulaire, nous avons donc choisi la formulation de Giles pour les limites d'entrée d'écoulement et de radiation, et la formulation de Poinsot et Lele pour la limite de sortie d'écoulement. Des conditions aux limites de type 'ghost cells' avec un schéma du $4^{ème}$ ordre seront utilisées pour les parois solides. Toutes ces conditions aux limites ont été testées dans la configuration multi-blocs du paragraphe §2.3.2, qui consiste en un écoulement au-dessus d'une marche descendante, où nous avons obtenu une bonne prédiction des champs instantannés d'écoulement ainsi que de la fréquence d'oscillation. La méthode numérique semble donc appropriée à la simulation d'écoulements instationnaires au-dessus de surfaces solides discontinues, de type cavité.

Introduction

During the implementation and improvement of the code it is of extreme importance to validate, step by step, the numerical method. The aim is to have a numerical tool appropriate for the study of the noise emitted by a laminar flow over a cavity, in which several aspects are involved: aeroacoustics, viscous effects, and multi-block geometries. For each of these aspects several validation test cases have been performed, which are outlined in table 2.1 and presented in the next sections.

2.1 Aeroacoustic test cases

Five test cases of increasing complexity have been implemented to test the suitability of the code to acoustic studies. Their objective is to validate the non-dissipative and non-dispersive properties of the discretization scheme, as well as the non-reflecting and solid boundary conditions, and the treatment of the corner.

2.1.1 Propagation of waves in a uniform flow

This is the first Aeroacoustic test case, consisting of an acoustic wave, a vorticity wave and an entropy wave propagating in a uniform flow at a Mach number $M = 0.5$ with no solid boundary, as shown in figure 2.1. On the left plot, the acoustic and the entropy waves are displayed by the density isocontours. The acoustic wave is placed in the center of the domain, while the entropy wave is closer to the outflow boundary, at the same location as the vorticity wave as shown on the right plot. The acoustic wave expands radially and propagates at the speed $(u_\infty + c)$ downstream and $(u_\infty - c)$ upstream, whereas the other two waves are convected at the flow speed u_∞. As a consequence of this setting, the three waves reach the outflow boundary simultaneously.

	Aeroacoustic test cases	**Validation**
§2.1.1	Propagation of waves in a uniform flow	Schemes, non-reflecting boundaries
§2.1.2	Propagation of waves in a uniform diagonal flow	Non-reflecting boundaries
§2.1.3	Single wall reflection in a uniform flow	Wall boundary conditions
§2.1.4	Single wall reflection in a boundary layer	Wall, viscous effects
§2.1.5	Multiple wall reflection	Wall, corner treatment
	Viscous test cases	**Validation**
§2.2.1	Blasius boundary layer	Viscous effects, wall
§2.2.2	Poiseuille channel flow	Viscous effects, wall, outflow
	Multi-block test case	**Validation**
§2.3.2	Backward-facing-step with incoming boundary layer	Multi-block geometry

Table 2.1 - *Overview of the validation test cases.*

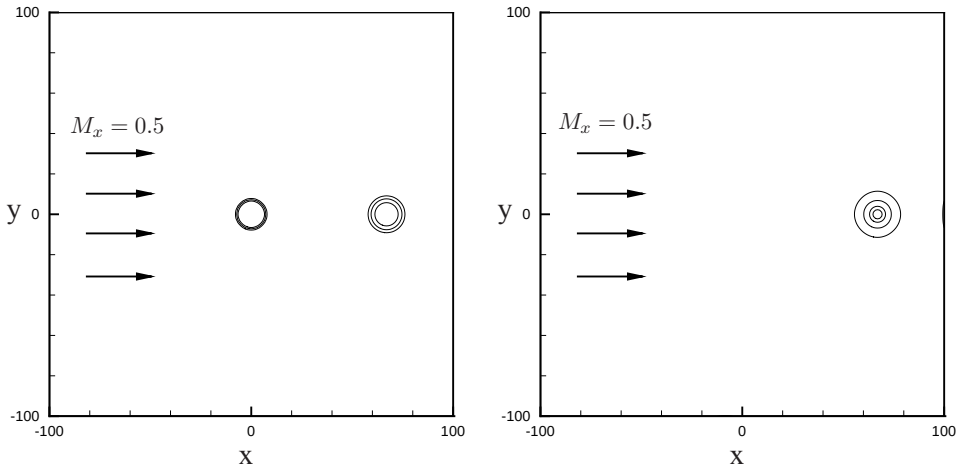

(a) Density contours (acoustic and entropy waves) (b) Vorticity contours (vorticity wave)

Figure 2.1 - *Initial conditions for the propagation of waves in an homogeneous media.*

This is problem 1, category 3 of the First Workshop on Benchmark Problems in Computational Aeroacoustics [89]. Its objective is to test the effectiveness of the radiation, the inf ow and the outf ow boundary conditions and the isotropy property of the computational algorithm in a complex problem. This test case has been done in collaboration with the University of Leicester, as part of a joint study of high-order schemes for computational aeroacoustics, and has been published as an AIAA conference proceedings in Rona *et al.* [149].

The computational domain is $-100 \leq x \leq 100$, $-100 \leq y \leq 100$, discretized with an equidistant mesh of 201×201 points. The equations solved are the non-linear Euler equations in dimensional form and the initial f ow conditions are:

$$
\begin{aligned}
p &= p_\infty \left[1 + \varepsilon \, e^{\left[-(\ln 2) \left(\frac{x^2+y^2}{9} \right) \right]} \right] \\
\rho &= \rho_\infty \left[1 + \frac{\varepsilon}{\gamma} e^{\left[-(\ln 2) \left(\frac{x^2+y^2}{9} \right) \right]} + 0.1 \, \frac{\varepsilon}{\gamma} \, e^{\left[-(\ln 2) \frac{(x-67)^2+y^2}{25} \right]} \right] \\
u &= u_\infty \left[1 + 0.04 \, y \, \varepsilon \, e^{\left[-(\ln 2) \frac{(x-67)^2+y^2}{25} \right]} \right] \\
v &= -0.04(x-67) \, \varepsilon \, u_\infty \, e^{\left[-(\ln 2) \frac{(x-67)^2+y^2}{25} \right]}
\end{aligned}
$$

where the reference values are $p_\infty = 10^5$ Pa, $T_\infty = 298$ K and $u_\infty = M_x c_\infty$, where $M_x = 0.5$, $c_\infty = \sqrt{\gamma p_\infty / \rho_\infty} = 346$ m/s is the ambient speed of sound, and $\varepsilon = 0.01$.

The three boundary conditions detailed in section §1.4 are used at the non-ref ecting boundaries:

Giles: Characteristics of Giles at all the non-ref ecting boundaries

Poinsot and Lele: Characteristics of Poinsot and Lele with $\sigma = 0.25$ at the outf ow, and characteristics of Giles at the inf ow and radiation boundaries

Tam and Dong: Asymptotic formulation of Tam and Dong at all the non-ref ecting boundaries

Firstly the results using Giles are shown. After that, they are compared with the other two formulations.

The computations are performed in dimensional form, but the values of density, pressure, and time are normalized in order to validate the results. The normalization is done using the following scales: length scale $\Delta x = \Delta y$, time scale $\Delta x/c_\infty$ and density scale $\varepsilon\rho_\infty/\gamma$. From these, the velocity and pressure are scaled by c_∞ and $\varepsilon\rho_\infty c_\infty^2$, and hence the non-dimensional values of the perturbations $\tilde{\rho}'$ and $\tilde{p}'$ are: $\tilde{\rho}' = \tilde{\rho} - \gamma/\varepsilon$ and $\tilde{p}' = \tilde{p} - 1/\varepsilon$.

The results are validated against the non-dimensional analytical solution given in the First Workshop on Benchmark Problems in Computational Aeroacoustics [89], which is derived from the linearized Euler equations:

$$\tilde{p}' = \frac{1}{2\alpha_1}\int_0^\infty e^{-\xi^2/4\alpha_1}\cos(\xi t)J_0(\xi\eta)\xi\, d\xi$$
$$\tilde{\rho}' = \tilde{p}' + e^{-\alpha_2\left[(x-67-M_x t)^2+y^2\right]}$$

where $\alpha_1 = [(\ln 2)/9]$, $\alpha_2 = [(\ln 2)/25]$, $\eta = [(x - M_x t)^2 + y^2]^{1/2}$ and J_0 is a Bessel function of order 0. The evaluation in the integral has been done numerically with MATLAB®7.3.0 using the adaptive Lobatto quadrature with an absolute error tolerance of $1.0e-9$.

The computed results for non-dimensional density $\tilde{\rho}$ are shown in f gure 2.2, corresponding to the adimensional times $\tilde{t} = 30$, 60 and 120. The four contour levels $\tilde{\rho}' = (-0.02, 0.01, 0.02, 0.04)$ are selected according to the First Workshop on Benchmark Problems in CAA.

Figure 2.2(a), on the left, shows the adimensional density contours for the combined convected acoustic, vorticity and entropy waves at an adimensional time $\tilde{t} = 30$. The waves are approaching the right computational boundary, but they have not crossed it yet. The numerical prediction, shown by the black dashed line, overlaps the analytical solution, which is shown by the continuous blue line. The acoustic wave is expanding radially at the same time that is convected by the f ow, and the entropy wave is convected downstream without distortion. Both of them are perfectly circular, proving that there is no degradation due to the propagation at an angle respect to the Cartesian mesh.

In f gure 2.2(a), on the right, a cross-section of the non-dimensional density distribution along the *x*-axis, i.e. at $y = 0$, is given. The location of this cross-section is taken as in the benchmark problem solution guideline. The numerical solution, represented by the squares ■, shows very good agreement with the analytical solution, displayed by the solid line. Particularly, there are no appreciable discrepancies near the computational boundaries between the two solutions.

The acoustic, entropy, and vorticity waves impinge simultaneously against the right computational boundary at the non-dimensional time $\tilde{t} = 60$, as it can be seen in f gure 2.2(b). There is a good

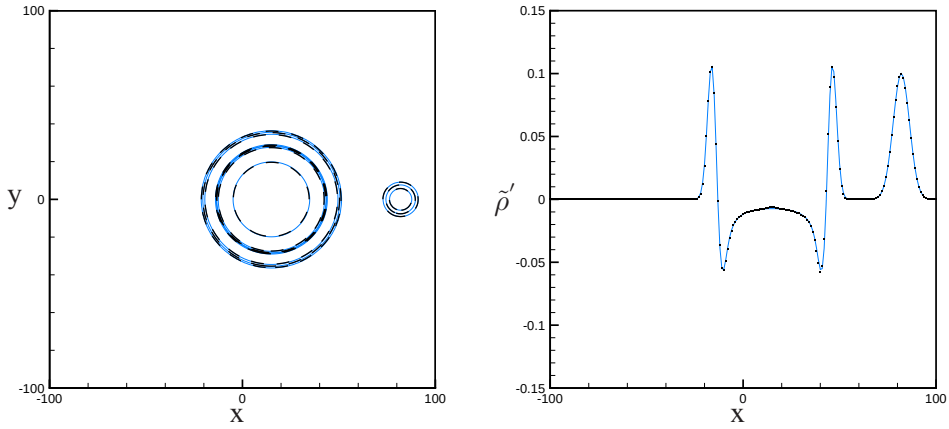

(a) time = 30

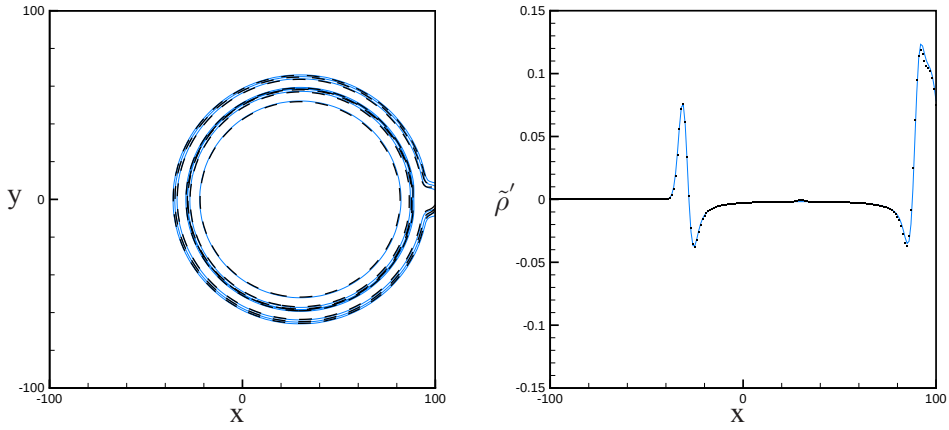

(b) time = 60

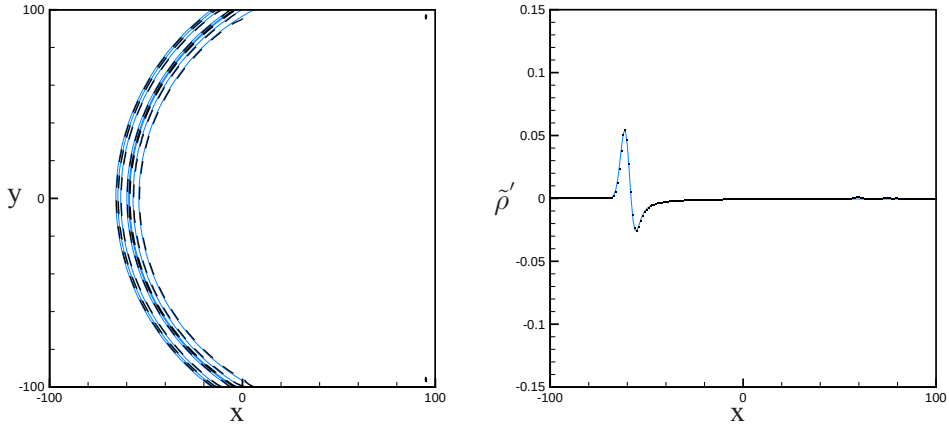

(c) time = 120

Figure 2.2 - *Results for the propagation of 3 waves in a uniform flow. Left plots: non-dimensional density contours* $\tilde{\rho}'$*, contour levels -0.02, 0.01, 0.02, 0.04;* $(-)$ *analytical solution,* $(--)$ *numerical prediction. Right plots: normalized density distribution* $\tilde{\rho}'$ *at* $y = 0$*,* $(-)$ *analytical solution,* $(\blacksquare)$ *numerical prediction*

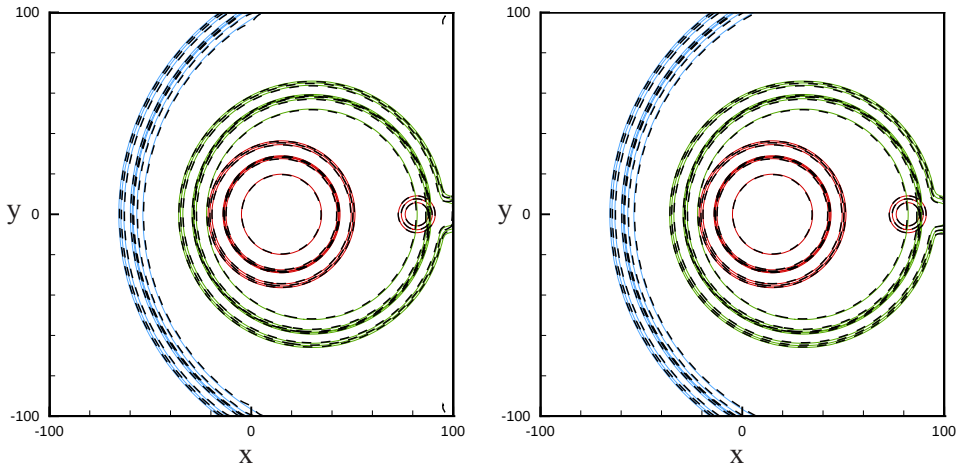

(a) Poinsot and Lele (b) Tam and Dong

Figure 2.3 - *Results for the propagation of 3 waves in a uniform flow. Non-dimensional density contours* $\tilde{\rho}'$*, contour levels -0.02, 0.01, 0.02, 0.04;* $(-)$ *analytical solution,* $(--)$ *numerical prediction at different times. Red for* $\tilde{t} = 30$*, green for* $\tilde{t} = 60$ *and blue for* $\tilde{t} = 120$

overlap of the analytical solution by the numerical prediction. More information about the interaction between the three waves is obtained from the waveform along the *x*-axis. As the waves coalesce onto one another at the right computational boundary, the density perturbation constructively interfere, creating a normalized density peak of about $\tilde{\rho}' \sim 0.125$. The numerical solution slightly underestimates the maximum, since the maximum is located between two points of the discretized computational domain.

At the last represented adimensional time, $\tilde{t} = 120$, the entropy and vorticity waves have escaped the domain, and only the acoustic wave remains in the interior domain, as represented in f gure 2.2(c). Even at the lowest non-dimensional density contour level of 0.01 there are no ref ections due to the boundary conditions. The non-dimensional density distribution along the *x*-axis, plotted to the right of the contour map, shows a good agreement between the numerical prediction and the analytical solution.

The results obtained using the other two non-ref ecting boundary conditions are shown in f gure 2.3. In both cases the non-dimensional density contours collapse very well with the analytical solution, proving the good performance of the characteristic formulation of Poinsot and Lele and the asymptotic solution of Tam and Dong.

2.1.2 Propagation of waves in a uniform diagonal f ow

In the previous problem §2.1.1, the non-ref ecting boundary conditions have been validated. However, as explained in section §1.4, characteristic boundary conditions are known to be good for waves travelling in a direction normal to the boundary, but might present problems when they impact the boundary with a certain angle or in the presence of a tangential mean f ow. It is for this reason that a more complex case is implemented: an acoustic, an entropy and a vorticity wave propagating in a Mach $M = 0.5$ f ow moving at 45° with respect to the boundaries, as displayed in f gure 2.4. This is problem 2, category 3 of the First Workshop on Benchmark Problems in Computational Aeroacoustics [89].

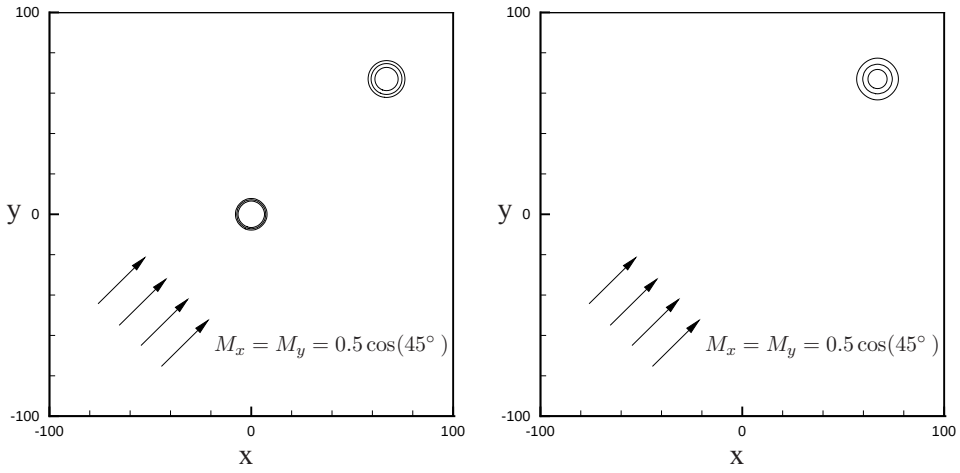

(a) Density contours (acoustic and entropy waves) (b) Vorticity contours (vorticity wave)

Figure 2.4 - *Initial conditions for the propagation of waves in the presence of a mean flow in x- and y-directions.*

The computational domain is $-100 \leq x \leq 100$, $-100 \leq y \leq 100$, discretized with an equidistant mesh of 201×201 points. The equations solved are the non-linear Euler equations in dimensional form and the initial f ow conditions are:

$$
\begin{aligned}
p &= p_\infty \left[1 + \varepsilon\, e^{\left[-(\ln 2)\left(\frac{x^2+y^2}{9}\right)\right]}\right] \\
\rho &= \rho_\infty \left[1 + \frac{\varepsilon}{\gamma} e^{\left[-(\ln 2)\left(\frac{x^2+y^2}{9}\right)\right]} + 0.1\,\frac{\varepsilon}{\gamma}\, e^{\left[-(\ln 2)\frac{(x-67)^2+(y-67)^2}{25}\right]}\right] \\
u &= u_\infty \left[1 + 0.04\,(y-67)\,\varepsilon\, e^{\left[-(\ln 2)\frac{(x-67)^2+(y-67)^2}{25}\right]}\right] \\
v &= -0.04(x-67)\,\varepsilon\, u_\infty\, e^{\left[-(\ln 2)\frac{(x-67)^2+(y-67)^2}{25}\right]}
\end{aligned}
$$

where the reference values are $p_\infty = 10^5$ Pa, $T_\infty = 298$ K and $u_\infty = M_x c_\infty$, where $c_\infty = \sqrt{\gamma p_\infty/\rho_\infty} = 346$ m/s is the ambient speed of sound, $M_x = M_y = 0.5\cos(45^\circ)$ and $\varepsilon = 0.01$.

Since there is a mean f ow in both *x*- and *y*-directions, the bottom and left boundaries are implemented as an inf ow, using the characteristic boundary conditions of Giles. On the other hand, the top and right boundaries are def ned as outf ow, for which two formulations are compared: Giles, and Poinsot and Lele with $\sigma = 0.25$.

As in the previous case §2.1.1, the simulations are done in dimensional form but the results are normalized for validation. The normalization is done using the same scales as §2.1.1.

The results are validated against the non-dimensional analytical solution of the linear Euler equations given in the First Workshop on Benchmark Problems in Computational Aeroacoustics [89]:

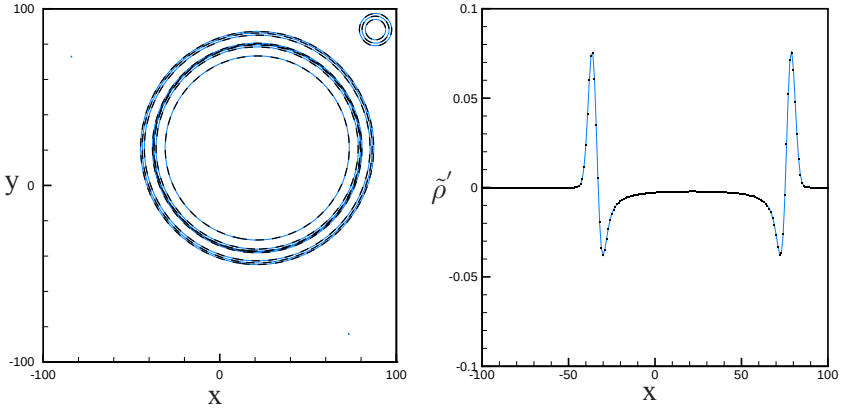

(a) time = 60

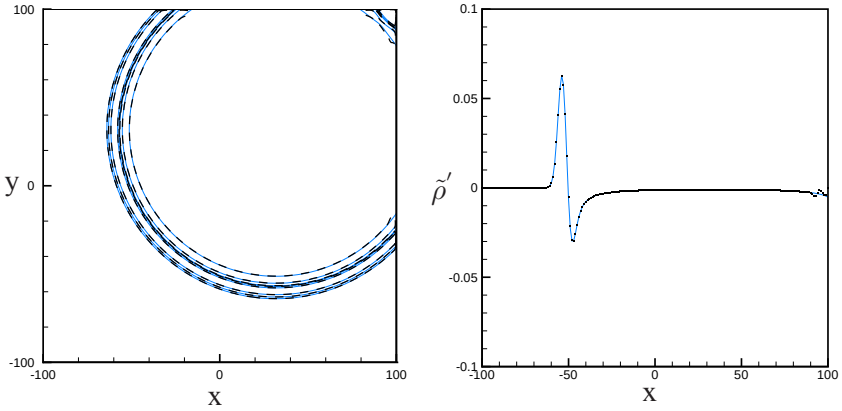

(b) time = 90

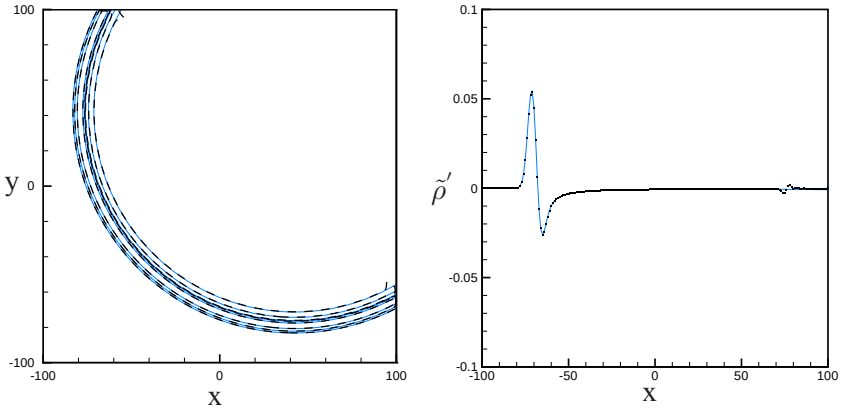

(c) time = 120

Figure 2.5 - *Results for the propagation of 3 waves in a uniform flow at 45° . Left plots: non-dimensional density contours $\tilde{\rho}'$, contour levels -0.02, 0.01, 0.02, 0.04;* $(-)$ *analytical solution,* $(--)$ *numerical prediction. Right plots: normalized density distribution $\tilde{\rho}'$, along the x-axis,* $(-)$ *analytical solution,* $(\blacksquare)$ *numerical prediction*

$$\tilde{p}' = \frac{1}{2\alpha_1}\int_0^\infty e^{-\xi^2/4\alpha_1}\cos(\xi t)J_0(\xi\eta)\xi\, d\xi$$
$$\tilde{\rho}' = \tilde{p}' + e^{-\alpha_2\left[(x-67-M_x t)^2+(y-67-M_y t)^2\right]}$$

where $\alpha_1 = [(\ln 2)/9]$, $\alpha_2 = [(\ln 2)/25]$, $\eta = [(x - M_x t)^2 + (y - M_y t)^2]^{1/2}$ and J_0 is a Bessel function of order 0. The MATLAB subroutine used for the previous case §2.1.1 has been adapted to this problem.

Figure 2.5 shows the results of non-dimensional density perturbations at different times. The levels $\tilde{\rho}' = (-0.02, 0.01, 0.02, 0.04)$ of the 2D density contour maps on the left have been selected in accordance to the guidelines of the First Workshop on Benchmark Problems in CAA [89]. On the right, the cross-section of the non-dimensional density distribution along the *x*-axis is given, as suggested by the benchmark problem solution guideline.

The plots show the results obtained with the outf ow formulation of Poinsot and Lele. The use of Giles characteristic boundary conditions gives identical results.

Figure 2.5(a) corresponds to the time $\tilde{t} = 60$, when the waves have not yet reached any computational boundary. The acoustic wave is expanding radially and being convected at the same time as the entropy and the vorticity waves. The waves do not present any distortion and overlap perfectly the analytical solution.

In f gure 2.5(b), where $\tilde{t} = 90$, the waves are crossing the outf ow boundaries. The contours near the upper corner correspond to the combination of the entropy and the acoustic wave, who are leaving the domain simultaneously. The overall agreement between analytical and numerical solutions is good. At the time $\tilde{t} = 120$, displayed in f gure 2.5(c), the entropy and vorticity waves have left the domain without ref ections. The acoustic wave which is still inside the computational domain gives good agreement with the reference solution, but some distortion of the wave is observed near the boundaries.

On the right plot of f gure 2.5(b), the waveform along the *x*-axis shows a general good overlap and a good prediction of the maxima and minima. Only near the outf ow boundary there is a small deviation, in the order of $\mathcal{O}(10^{-3})$ respect to the analytical solution. As proved in the following f gure 2.5(c), this slight deviation does not increase with time nor it expands, it is only convected back without contaminating the rest of the domain, so it can be considered negligible.

2.1.3 Single wall ref ection of an acoustic wave in a uniform f ow

This problem aims to test the wall boundary conditions in an acoustic problem, where the accuracy of the pressure prediction is of high importance. It consists of an acoustic wave convected by a uniform f ow at $M = 0.5$ that impacts against an horizontal wall located at the south of the perturbation source as shown in f gure 2.6.

This test case has been done in collaboration with the University of Leicester, and has been published as an AIAA conference proceedings in Rona *et al.* [149]. This the problem 1, category 4 of the First Workshop on Benchmark Problems in Computational Aeroacoustics [89].

The computational domain is $-100 \leq x \leq 100$, $0 \leq y \leq 200$, discretized with an equidistant

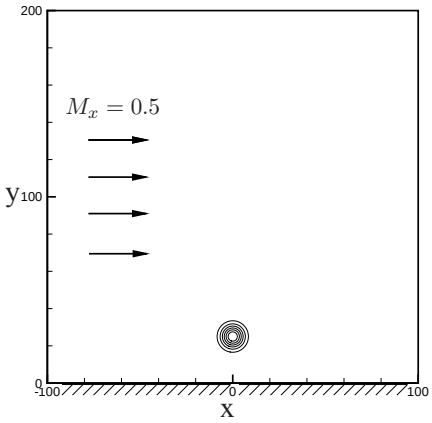

Figure 2.6 - *Initial density conditions for a single wall reflection of an acoustic pulse.*

Cartesian grid of 201×201 points. The equations solved are the non-linear Euler equations and the initial f ow conditions are:

$$
\begin{aligned}
p &= p_\infty \left[1 + \varepsilon\, e^{\left[-(\ln 2)\left(\frac{x^2+(y-25)^2}{25}\right)\right]}\right] \\
\rho &= \rho_\infty \left[1 + \frac{\varepsilon}{\gamma} e^{\left[-(\ln 2)\left(\frac{x^2+(y-25)^2}{25}\right)\right]}\right] \\
u &= u_\infty \\
v &= 0
\end{aligned}
$$

where the reference values are $p_\infty = 10^5$Pa, $T_\infty = 298$K and $u_\infty = Mc_\infty$ where $c_\infty = \sqrt{\gamma p_\infty/\rho_\infty} = 346$m/s is the ambient speed of sound, the Mach number is $M = 0.5$ and $\varepsilon = 0.01$.

Two boundary conditions have been used for the wall: Gloerfelt's boundary conditions, and the ghost cells method with a 2^{nd} order scheme. For the other boundaries, the non-ref ecting characteristic boundary conditions of Giles have been used. Both solid boundary conditions gave similar results. For clarity, only the results obtained using ghost cells (2^{nd} order) are shown.

As in the previous sections, the computations are done in dimensional form but the results are normalized for validation. The scales used for the normalization are described in §2.1.1.

The validation has been done against the analytical solution given in the f rst NASA Workshop on Benchmark Problems in CAA [89]:

$$
\tilde{p}' = \tilde{\rho}' = \frac{1}{2\alpha} \int_0^\infty e^{-\xi^2/4\alpha} \cos(\xi t)[J_0(\xi\eta) + J_0(\xi\zeta)]\xi \, d\xi
$$

where $\alpha = [(\ln 2)/25]$, $\eta = [(x - Mt)^2 + (y - 25)^2]^{1/2}$, $\zeta = [(x - Mt)^2 + (y + 25)^2]^{1/2}$ and J_0 is a Bessel function of order 0.

Figure 2.7 shows the results for density perturbations at the non-dimensional times $\tilde{t} = 30$, 60 and 120. The levels 0.01 and 0.05 of the two-dimensional density contour maps have been selected in ac-

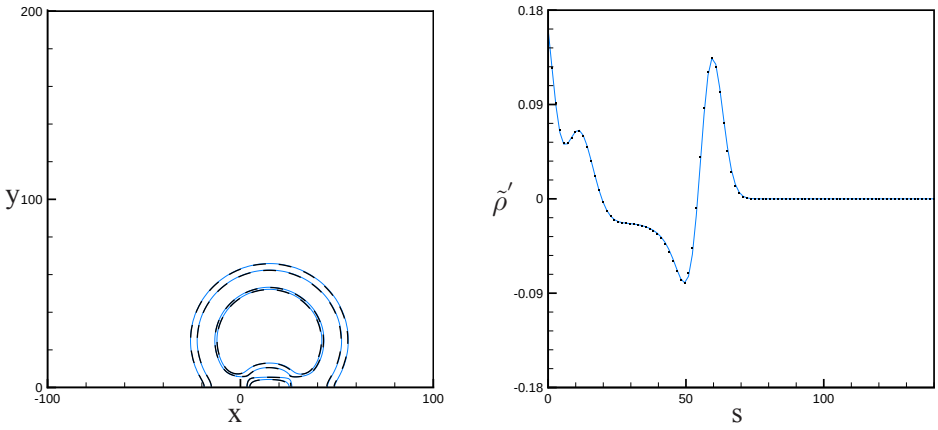

(a) time = 30

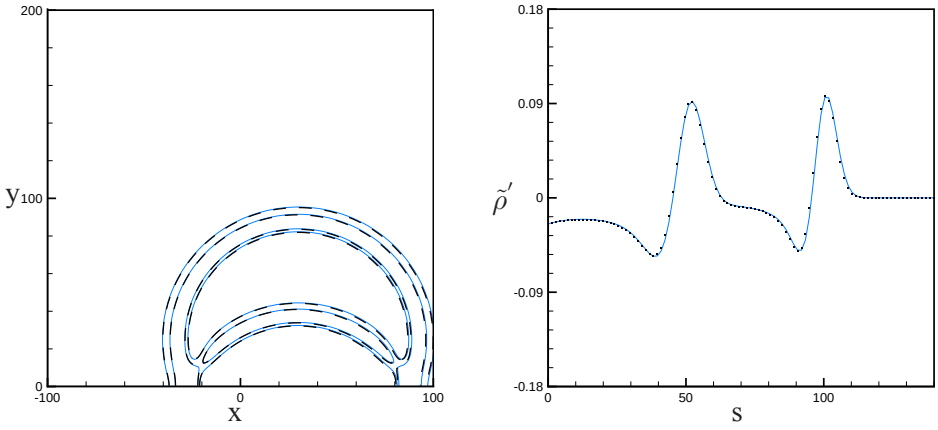

(b) time = 60

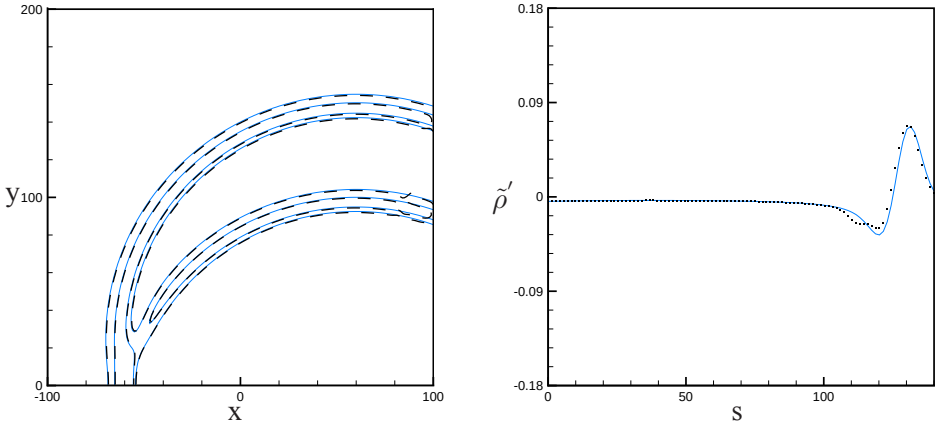

(c) time = 120

Figure 2.7 - *Results for a single wall reflection in a uniform flow. Left plots: non-dimensional density contours* $\tilde{\rho}'$*, contour levels 0.01, 0.05;* $(-)$ *analytical solution,* $(--)$ *numerical prediction. Right plots: normalized density distribution* $\tilde{\rho}'$*, along the line* $x = y$*,* $(-)$ *analytical solution,* $(\blacksquare)$ *numerical prediction*

cordance to the guidelines of the workshop. The same guideline has been followed in order to chose the mono-dimensional cross-section along the $x = y$ line.

At the time $\tilde{t} = 30$ the density pulse has just reached the wall. Figure 2.7(a) proves that the predicted results of the early stages of the ref ected wave give a good agreement with the analytical solution, both in the two-dimensional contour f eld and the density prof le along the $x = y$ line. Figure 2.7(b) shows the ref ected acoustic wave at $\tilde{t} = 60$, just before it goes through the downstream non-ref ecting computational boundary. The density perturbations cross-section to the right of the contour map shows two similar peaks, the peak at $s = 50$ is the pulse ref ection from the wall and its shape is similar to the incident wave, which is centered at $s \sim 100$. The numerical prediction overlaps the reference analytical solution.

Finally, f gure 2.7(c) shows the acoustic pulse after it has crossed the right computational boundary, corresponding to $\tilde{t} = 120$. In general the agreement between the predicted and analytical solutions is good, even though there is a small difference next to the non-ref ecting boundary which can be slightly observed in the two-dimensional contour f eld and is highlighted by the waveform. At $s > 100$ the predicted density perturbation minimum is slightly under-estimated by the numerical method and there is a difference between reference and numerical solutions in the order of $\mathcal{O}(10^{-3})$. The density perturbation maximum is instead well-captured by the numerical prediction.

2.1.4 Single wall ref ection of an acoustic wave in a boundary layer f ow

In order to study the viscous effects in an acoustic problem, the single wall ref ection problem from §2.1.3 is repeated but the whole Navier-Stokes equations are solved. Due to the non-slip condition at the wall a uniform f ow cannot be imposed, and so the propagation of the pulse is done in the presence of a boundary layer f ow. The Mach number is maintained at $M = 0.5$, and the Reynolds number of the f ow based on the boundary layer thickness at the inf ow is $Re_\delta = 516$.

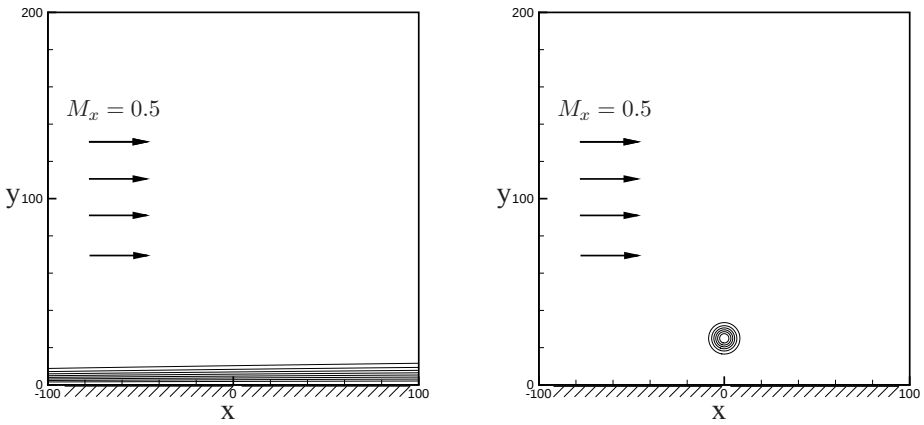

(a) Streamwise velocity (b) Density

Figure 2.8 - *Initial conditions for a single wall reflection of an acoustic pulse in the presence of a boundary layer flow.*

The computational domain is square to match the previous test case §2.1.3, but of smaller physical dimensions in order to obtain a laminar flow, and to keep the Mach number the same as before. To compare the results with the Euler case, the dimensions of the domain (the axis x and y) are re-scaled in order to get a domain of $-100 \leq x \leq 100$ and $0 \leq y \leq 200$. In this case the grid is equidistant in the *x*-direction, whereas it is non-uniform in *y*-direction. The grid is refined near the wall, and it contains around 35 points inside the boundary layer. In total there are 290×140 points, and $\Delta x_{min} = 2.5\Delta y_{min}$.

The velocity field is initialized with a very thin boundary layer as shown in figure 2.8(a). The simulation is run until a steady state for all the variables is obtained. After that, an acoustic wave as in §2.1.3 is added, as displayed by figure 2.8(b). The acoustic pulse is placed at the same non-dimensional distance from the wall as in §2.1.3, which corresponds to $1/8$ of the computational domain.

The characteristic boundary conditions of Giles are used at the non-reflecting boundaries. In addition, a numerical solution of the Blasius similarity equation for a laminar boundary layer is imposed at the inflow. At the walls, the boundary conditions of Gloerfelt and ghost cells with a 2^{nd} order scheme are used and compared.

Since there is no analytical solution for this problem, the two numerical predictions are compared, and then they are both compared to the analytical solution for the Euler equations, where the observed differences are justified. The computations are performed in dimensional form, and from the resulting values the base boundary layer flow is subtracted. After that, the results are normalized as in §2.1.1: time by $\Delta x/c_\infty$, density by $\varepsilon\rho_\infty/\gamma$, velocity by the sound speed c_∞ and pressure by $\varepsilon\rho_\infty c_\infty^2$.

Figure 2.9(a) shows the moment when the pulse first reaches the wall. The non-dimensional density contour levels $\tilde{\rho}' = (0.01, 0.05)$ have been selected as the previous test case §2.1.3, corresponding to the problem 1, category 4 of the First Workshop on Benchmark Problems in CAA [89]. On the left, the results for the two wall boundary conditions are compared, Gloerfelt in green solid line, and the ghost cells in black dashed line. Both results overlap perfectly, giving confidence on the cross-validation of these numerical predictions. On the right, the results predicted using the Navier-Stokes equations are compared to the Euler analytical solution. In order to plot them together, the axis of the boundary layer results have been re-scaled, and hence the boundary layer thickness has become around $\delta_{re-scaled} \approx 13$. It is interesting to see that in the region outside the boundary layer, where the viscous effects are not important, both results are exactly the same. On the other hand, inside the boundary layer, where the viscous effects are relevant, there is a slight difference between them.

In figure 2.9(b), the wave has already been reflected from the wall, and the incident wave (upper) and the reflected wave (lower) can be distinguished. The left figure shows again the comparison between Gloerfelt and ghost cells methods. Still, both of them overlap very well, even next to the wall, where the boundary condition could create some deviations. The right figure shows the ghost cells results compared to the Euler analytical solution. Here the difference inside the boundary layer is more enhanced. It is easy to see that the Navier-Stokes prediction propagates upstream faster than the Euler case. The reason for this is the speed of propagation of the acoustic wave, which is $(u - c)$, that is to say, the difference between the flow and the sound speed. In the Euler case, there is a uniform flow propagating at $M = 0.5$, which means that the acoustic wave propagates at $M = 0.5$ as well in the whole domain. In the Navier-Stokes case, the velocity near the wall is almost zero, which implies that the acoustic wave in this region will move close to the sound speed. The same phenomenon explains why, in the direction of the flow, the wave propagates faster in the Euler case than in the Navier-Stokes case.

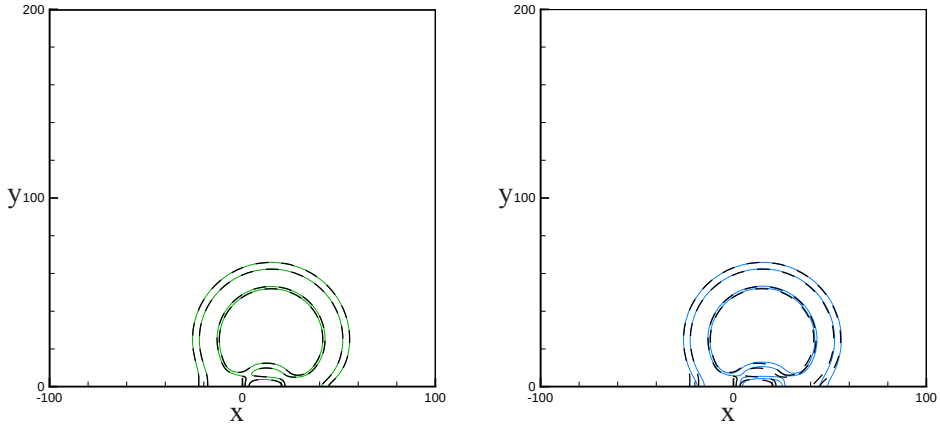

(a) time = 30

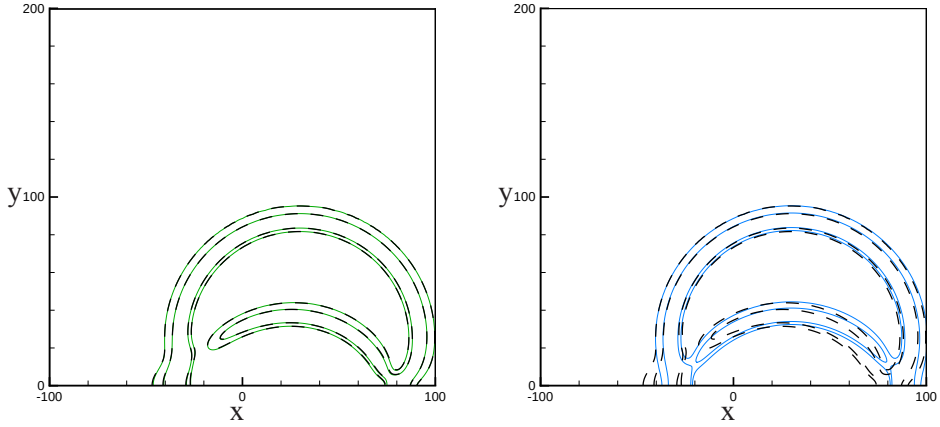

(b) time = 60

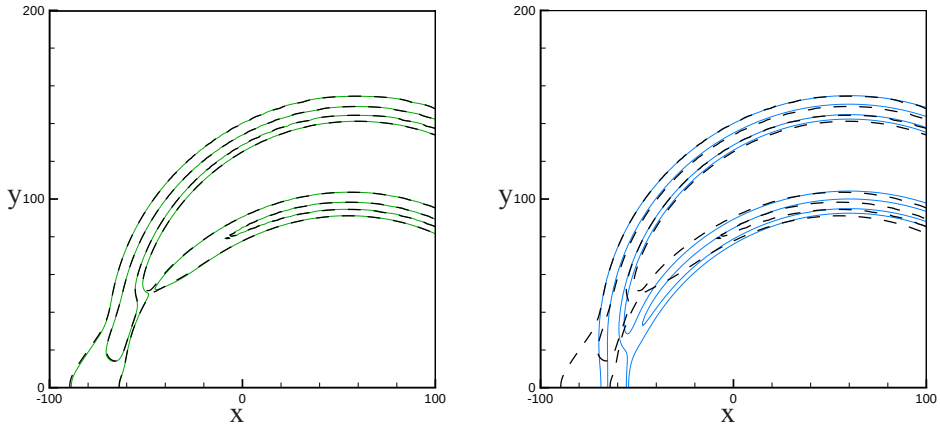

(c) time = 120

Figure 2.9 - *Results for a single wall reflection in a boundary layer flow. Density contours 0.01, 0.05. Left plots: green solid line: Gloerfelt boundary condition; black dashed line: ghost cells. Right plots: blue solid line: Euler analytical solution; black dashed line: Navier-Stokes numerical prediction.*

Finally, in figure 2.9(c) the waves have crossed the non-reflecting boundaries. The left plot shows the results for both solid boundary conditions, which are perfectly matched. The right plot displays the comparison between Euler and Navier-Stokes, where the differences between the two cases are highlighted. The results for the incident wave (the upper wave in the plot) overlap perfectly each other. On the other hand, even outside the boundary layer, the reflected wave presents some differences between the two cases. This is the effect that the difference of viscous conditions near the wall have caused in the reflected wave.

2.1.5 Multiple wall reflection of an acoustic wave

This is the last test case done in collaboration with the University of Leicester and published as an AIAA conference proceedings in Rona *et al.* [149]. This problem is inspired by the benchmark cases §2.1.1 and §2.1.3. The innovation is the presence of two walls, on the bottom and right boundaries, forming a corner. It is aimed to test the ability of the solid boundary conditions of section §1.5 to handle multiple acoustic wave reflections.

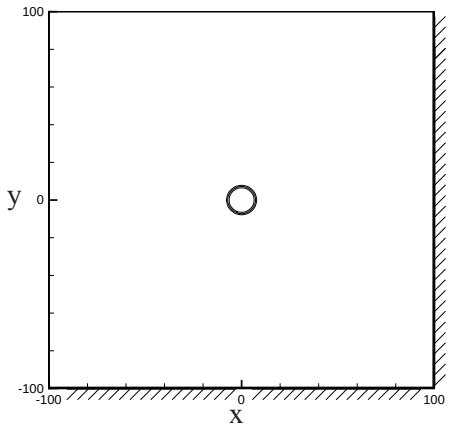

Figure 2.10 - *Initial density conditions for a multiple wall reflection of an acoustic pulse.*

This problem consists on an acoustic pulse located at the center of the domain which impacts against a corner as shown in figure 2.10. The computational domain is $-100 \leq x \leq 100$, $-100 \leq y \leq 100$, and the spatial discretization is an equidistant Cartesian grid of 201×201 points. In this problem there is no incoming flow, the governing equations are the non-linear Euler equations and the initial flow conditions are a simplification of problem 1, category 3 in [89]:

$$
\begin{aligned}
p &= p_\infty \left[1 + \varepsilon \, e^{\left[-(\ln 2) \left(\frac{x^2+y^2}{9} \right) \right]} \right] \\
\rho &= \rho_\infty \left[1 + \frac{\varepsilon}{\gamma} \, e^{\left[-(\ln 2) \left(\frac{x^2+y^2}{9} \right) \right]} \right] \\
u &= 0 \\
v &= 0
\end{aligned}
$$

where the reference values are $p_\infty = 10^5$Pa, $T_\infty = 298$K and $\varepsilon = 0.01$.

Two boundary conditions have been used for the wall: Gloerfelt's boundary conditions and the 2^{nd} order ghost cells method. For the other boundaries, the non-ref ecting characteristic boundary conditions of Giles have been used. Both solid boundary conditions gave similar results. For clarity, only the results obtained using 2^{nd} order ghost cells are shown.

The results have been normalized as for the test case §2.1.1. An analytical solution has been derived by mirroring the solution of the single-wall ref ection problem §2.1.3 about the right wall and by adding the original and the mirrored pressure and density f elds. This gives:

$$\tilde{p}' = \tilde{\rho}' = \frac{1}{2\alpha}\int_0^\infty e^{-\xi^2/4\alpha}\cos(\xi t)[J_0(\xi\eta) + J_0(\xi\zeta) + J_0(\xi\phi) + J_0(\xi\mu)]\xi\, d\xi$$

where $\alpha = [(\ln 2)/9]$, $\eta = [x^2 + y^2]^{1/2}$, $\zeta = [x^2 + (y + 200)^2]^{1/2}$, $\phi = [(x - 200)^2 + y^2]^{1/2}$, $\mu = [(x - 200)^2 + (y + 200)^2]^{1/2}$ and J_0 is a Bessel function of order 0.

Figure 2.11 shows the propagation of the density perturbation at the non-dimensional times $\tilde{t} = 60$, 120 and 180. Contour levels have been selected as the guideline given in the f rst workshop on benchmark problems in CAA [89] for the problem 1, category 3, which are $\tilde{\rho}' = (-0.02, 0.01, 0.02, 0.04)$. To the right of the contours, the density perturbation distribution along the *x*-axis at $y = 0$ is shown. This mono-dimensional prof le is selected since it has a non-ref ecting boundary on the left and a solid boundary on the right.

At the time $\tilde{t} = 60$ the acoustic pulse has not reached yet any of the boundaries as seen in f gure 2.11(a). Due to the absence of an incoming f ow, it presents symmetric contour f eld and cross-section prof le. The numerical prediction overlaps the analytical solution, proving the good dispersive and dissi-pative properties of the numerical scheme in the interior of the computational domain.

Figure 2.11(b) shows the acoustic wave at the non-dimensional time $\tilde{t} = 120$. The density pulse has already impacted against the two walls and has gone through the non-ref ecting boundaries. The impact against the walls has caused local ref ections, which are apart from one-another and behave in a way similar to the previous case §2.1.3. The agreement between the predicted results and the reference analytical solution is good. In reference to the cross-section f gure, it is important to mention that the right hand side normalized density perturbation features a maximum followed by a minimum, while in f gure 2.11(a) a density perturbation minimum is followed by a maximum. This fact conf rms that this is a ref ection from an incident wave.

The last f gure 2.11(c) shows the density perturbation at the time $\tilde{t} = 180$, where the ref ected waves from the bottom and right walls have intersected. The wave branch close to the corner results from the combined wall conditions at the corner. As observed in the contour f eld, there is no evidence that such condition generated any spurious numerical feature as the numerical predictions well match the reference solution along this wave branch. Where the waves goes through the non-ref ecting boundaries, there is a small deviation of order $\mathcal{O}(10^{-3})$ between predicted and analytical solutions, as previously observed in f gure 2.7(c).

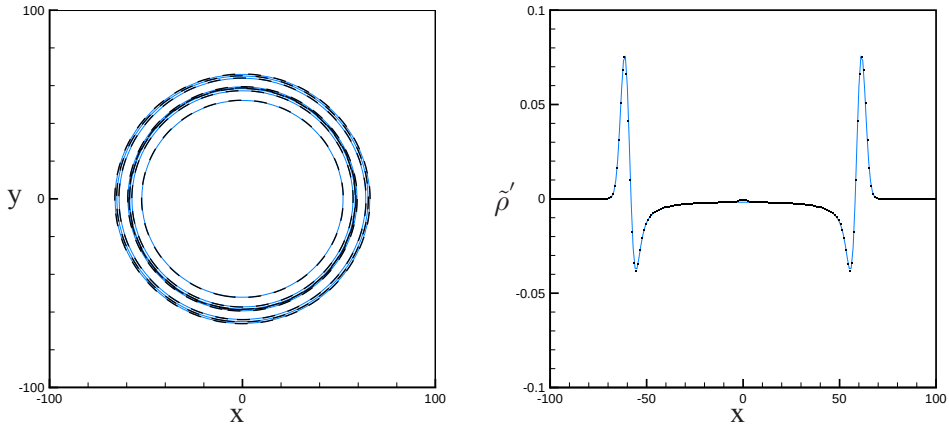

(a) time = 60

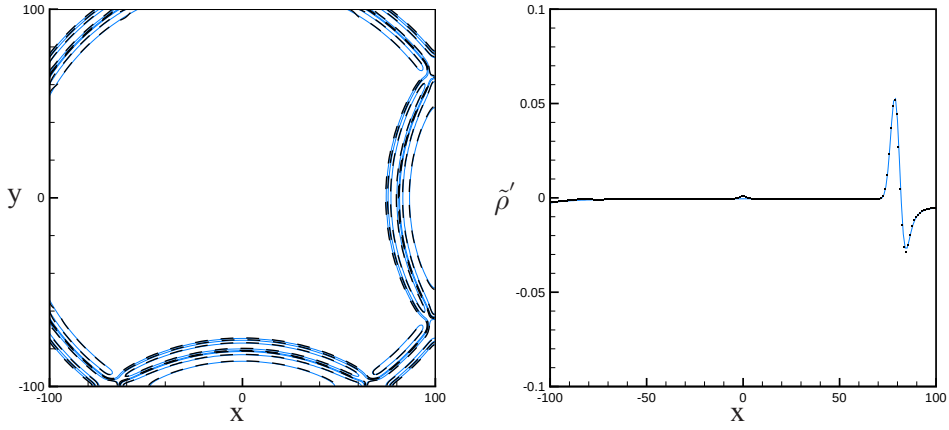

(b) time = 120

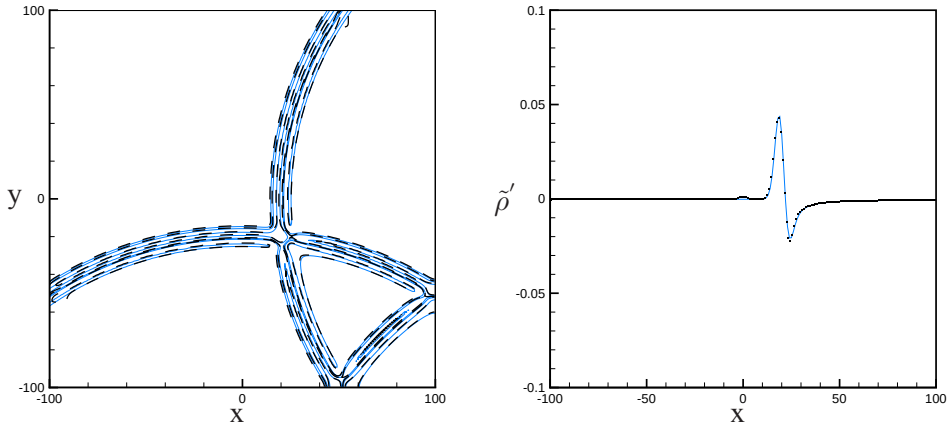

(c) time = 180

Figure 2.11 - *Results for multiple wall reflection. Left plots: non-dimensional density contours* $\tilde{\rho}'$*, contour levels -0.02, 0.01, 0.02, 0.04;* $(-)$ *analytical solution,* $(--)$ *numerical prediction. Right plots: normalized density distribution* $\tilde{\rho}'$ *at* $y = 0$*,* $(-)$ *analytical solution,* $(\blacksquare)$ *numerical prediction*

2.2 Viscous test cases

The following test cases aim the validation of the code in the presence of a viscous flow. For this reason, low Reynolds number wall-bounded flows are selected: a boundary layer over a flat plate, and a plane channel flow. Both configurations have been computed using the Navier-Stokes equations in a single block geometry.

2.2.1 Blasius boundary layer

This test case, proposed in the PhD thesis of Gloerfelt [75], was first implemented by Guaus [82] during the development of the code. It was done to test the Gloerfelt wall boundary conditions [75], which were originally applied over the total fluxes (convective and viscous fluxes). Those results were improved by applying the wall conditions only over the convective fluxes. In this investigation the ghost cells method is tested using the two discretization schemes to calculate the pressure gradient described in §1.5.2: the 4^{th} order scheme derived for this purpose and a classic 2^{nd} order scheme.

This problem consists on a boundary layer over a flat plate without any pressure gradient. The flow is considered compressible with a Mach number $M = 0.2$. The regime of the flow is laminar, with a Reynolds number based on the boundary layer thickness at the inflow $Re_\delta = 516$. The velocity is initialized with a numerical solution of the Blasius similarity equation; while pressure and temperature are initialized as homogeneous fields at $p_\infty = 10^5 Pa$ and $T_\infty = 298K$, and density is computed using the equation of state for ideal gases $\rho_\infty = p_\infty / rT_\infty$.

The computational grid is rectangular with 121 nodes in *x*- and 81 nodes in *y*-direction. In the flow direction the mesh is equidistant with an increment $\Delta x = 2.8 \cdot 10^{-6} m$. In the normal direction the mesh is stretched near the wall with a 2% of geometric ratio increment to better capture the boundary layer, with a minimum value $\Delta y_{min} = 1.4 \cdot 10^{-6} m$ which corresponds to $y^+ = 0.27$ at the inflow. The time step is calculated according to the CFL stability criterion described in §1.3.2; for this geometry and for a Courant number of 0.65 it is found to be $\Delta t = 2.625 \cdot 10^{-9} s$. The inflow is located at $\approx 20\delta$ from the origin of the boundary layer, and it extends to $\approx 9\delta$ from the inflow to the outflow.

A buffer zone is added after the outflow of the domain to avoid noise from numerical origin. This buffer zone contains 50 points and it is about 5 times the length of the domain, and consists on a very stretched mesh (with 2.5% of geometric ratio increment) and a filter proposed by Lele [119]. Since there are no large eddies convected downstream, this buffer zone is not required, but it is added in order to test its implementation for future applications in more complex flows (e.g. in section §2.3).

At the inflow, a numerical solution of the Blasius similarity equation for a laminar boundary layer is imposed. Furthermore, in order to avoid numerical reflections, the characteristic boundary conditions of Giles [73, 74] described in §1.4.1 are used at the inflow, outflow and radiation boundaries. Four different boundary conditions (b.c.) have been used at the wall: Gloerfelt b.c. applied over the total fluxes, Gloerfelt b.c. applied over the convective fluxes, 2^{nd} order ghost cells and 4^{th} order ghost cells. The simulation is computed until a stationary solution is obtained, which for all cases is after 30000 iterations.

The computed results have been validated with a reference solution (the numerical solution of the

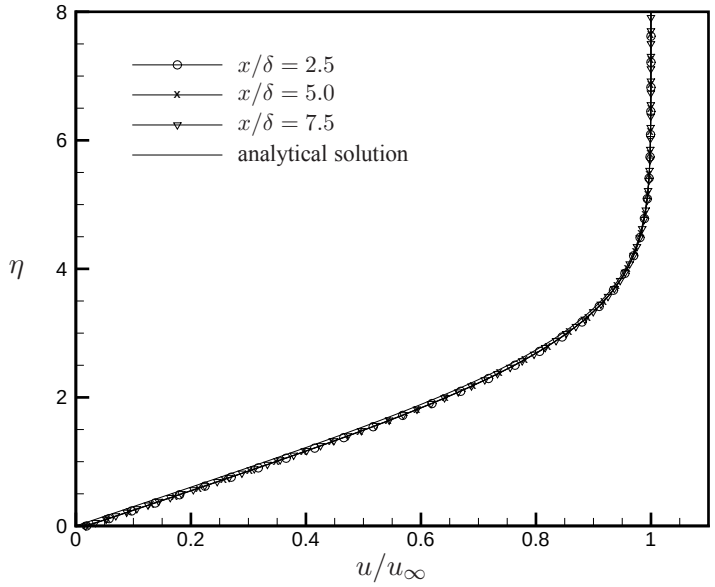

(a) Streamwise velocity

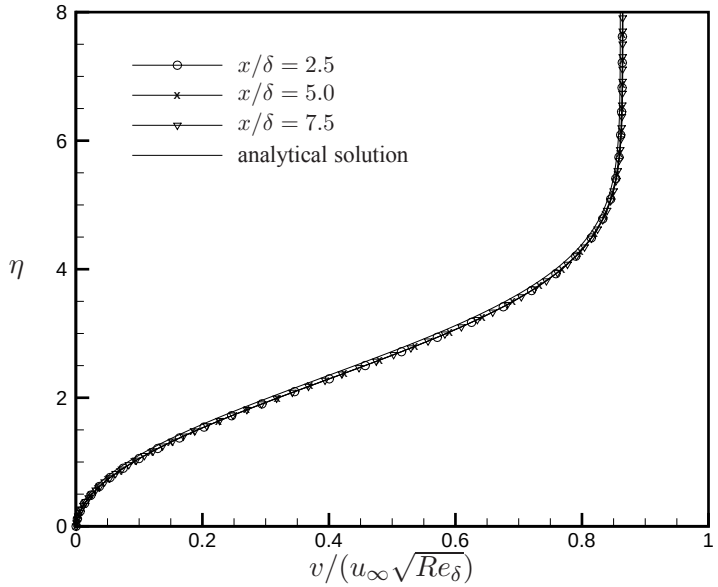

(b) Normal velocity

Figure 2.12 - *Results for a Blasius boundary layer. Adimensional velocity profiles with 2^{nd} order ghost cells at different x/δ from the inflow*

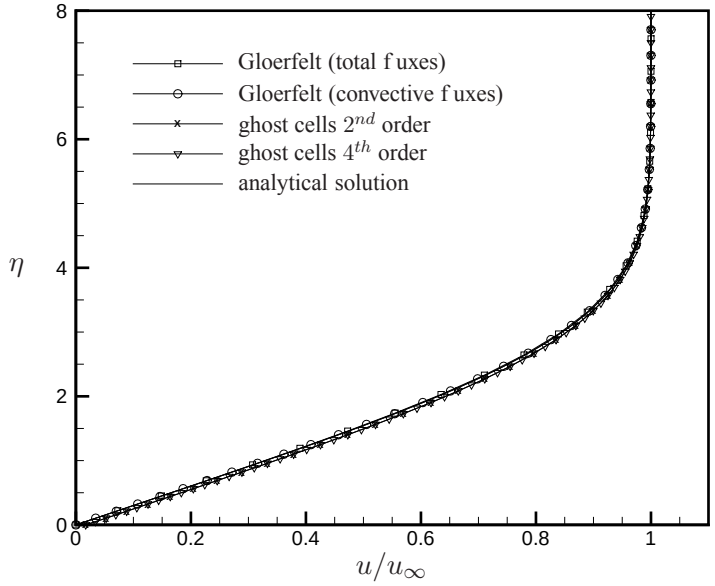

(a) Streamwise velocity

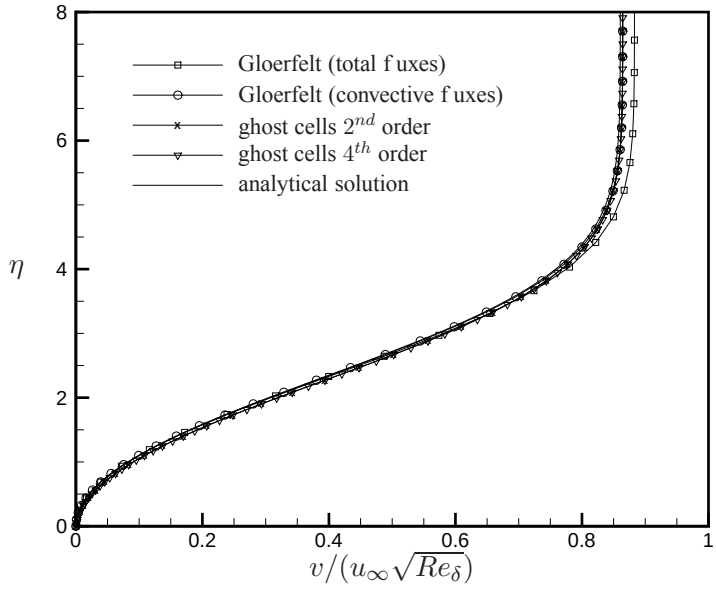

(b) Normal velocity

Figure 2.13 - *Results for a Blasius boundary layer. Adimensional velocity profiles at $x/\delta = 7.5$ from the inflow for different wall boundary conditions*

Blasius similarity equation) given for the velocity profiles. Streamwise velocity has been normalized by the mean freestream velocity u_∞, normal velocity has been adimensionalized with $u_\infty Re^{1/2}$, and η represents the adimensional normal coordinate:

$$\eta = y\sqrt{\frac{u_\infty \rho}{\mu(x + x_{origin})}}$$

where x_{origin} is the horizontal coordinate of the origin of the boundary layer. Profiles at different distances from the inflow, where the analytical solution is imposed, have been checked to observe the influence of the non-reflecting boundary condition. The results obtained with the different wall boundary conditions are compared.

Figure 2.12 shows the results obtained with the 2^{nd} order ghost cells method at several locations: $x/\delta = 2.5$, $x/\delta = 5.0$ and $x/\delta = 7.5$. These results are compared to the reference solution. Streamwise velocity corresponds to figure 2.12(a), while normal velocity, which is more sensitive to numerical errors, is shown in figure 2.12(b). All profiles collapse very well with the analytical solution, proving that there is no numerical influence from the boundary conditions. Moreover, it proves that pressure is constant through the field, i.e. there are no pressure gradients in both *x*- and *y*-directions.

Figure 2.13(a) shows the velocity profiles at $x/\delta = 7.5$ for the four different boundary conditions. These results are validated with the reference solution, and it is observed that the analytical solution is overlapped by the numerical predictions. Figure 2.13(b) shows the normal velocity profiles at the same location. Normal velocity is more sensitive to pressure fluctuations and numerical errors. In this figure, it is shown that the Gloerfelt boundary condition applied over the total fluxes presents some discrepancies with respect to the analytical solution. The other three wall boundary conditions collapse very well with the analytical solution.

2.2.2 Poiseuille channel flow

This problem was implemented during the first development of the code [82], being taken from the PhD thesis of Gloerfelt [75] and inspired by a study of Poinsot and Lele [140]. This case has been used to test, firstly, the wall boundary conditions, and secondly, the characteristic boundary conditions at the outflow. As the configuration of the previous case §2.2.1, the results of the simulation are validated with a reference solution, being in this case the analytical solution for a Poiseuille channel flow.

This test case consists of a Poiseuille channel flow moving at a Mach number $M = 0.1$. The Reynolds number based on the half-width of the channel h is $Re_h = 15$, so the flow is laminar and the viscous effects are important. The streamwise velocity is initialized with an approximation to the analytical solution, normal velocity as zero and pressure and temperature as homogeneous fields:

$$\begin{aligned} u &= u_\infty \left[\cos\left(\frac{\pi}{2}\frac{y}{h}\right)\right]^2 \\ v &= 0 \\ p &= p_\infty \\ T &= T_\infty \end{aligned}$$

where $u_\infty = Mc$, c is the ambient speed of sound, the initial reference values are $p_\infty = 10^5 Pa$ and $T_\infty = 298.15K$, and density is calculated as $\rho_\infty = p_\infty / rT_\infty$.

The channel considered for the study has a length equal to 10 times the half-width of the channel, where $h = 6.5 \cdot 10^{-6} m$. The computational domain is an equidistant grid of 101×101 points, with a space increment of $\Delta x = 6.5 \cdot 10^{-7} m$ and $\Delta y = 1.3 \cdot 10^{-7} m$ (so $\Delta x = 5\Delta y$). The time step is calculated according to the stability criterion described in §1.3.2; for this geometry and for a Courant number of 0.65 it is found to be $\Delta t = 2.44 \cdot 10^{-8} s$.

Wall boundary conditions

The streamwise velocity and the temperature at the inflow and outflow are imposed to be the analytical solution for a Poiseuille flow, while normal velocity is imposed to be zero. In addition, there is a pressure gradient imposed in the direction of the flow. Furthermore, the characteristics of Giles described in §1.4.1 are used at the inflow and outflow boundaries in order to avoid numerical reflections. For the wall boundary conditions, Gloerfelt wall boundary conditions and ghost cells with 2^{nd} and 4^{th} order approximations are used and compared. The simulation is computed until a stationary solution is obtained, after 20000 iterations.

In order to validate the results the analytical profiles for u velocity and temperature are used. Three different locations are selected, at different distances from the inflow. The values of velocity are normalized by the freestream mean velocity u_∞ and temperature is normalized by the reference temperature T_∞. The half-width of the channel h is used to normalize the *x*- and *y*-coordinates.

The results are shown in figure 2.14, where it is possible to see the profiles for the three wall boundary conditions. In the case of the u velocity, the agreement between predicted and analytical solutions is very good. On the other hand, the predicted results for the temperature differ from the analytical solution. The location where the error is smaller is at $x/h = 10$, the outflow, as shown in figure 2.14(c). Figures 2.14(a) show the profiles at the center of the channel and figure 2.14(b) between the center and the outflow, where the bigger difference compared to the analytical data might be due to the influence of the inflow boundary condition. These results show that the establishment of the temperature profile is approximately achieved after $10h$.

Respect to the different boundary conditions, no difference can be appreciated in the velocity profiles. However, the temperature profiles obtained with Gloerfelt wall boundary conditions are slightly closer to the analytical solution than those from the ghost cells method, both for the 2^{nd} and 4^{th} order approximations.

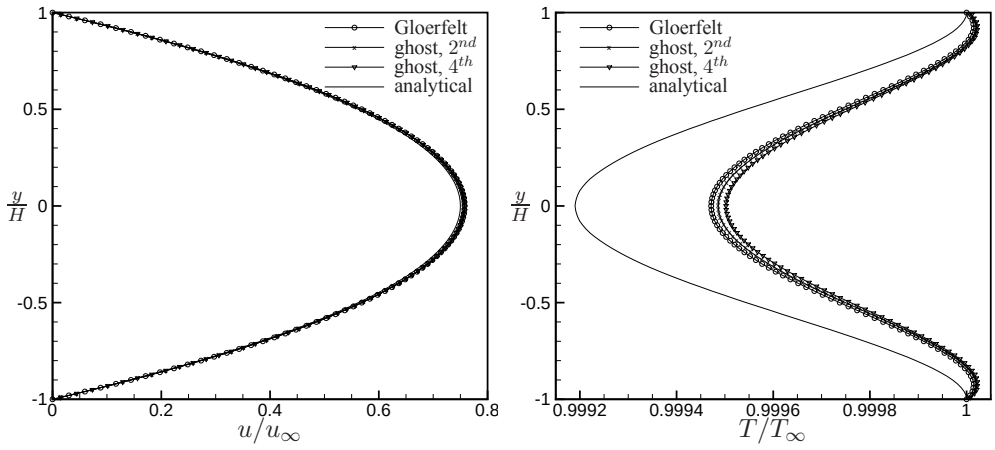

(a) x/h = 5

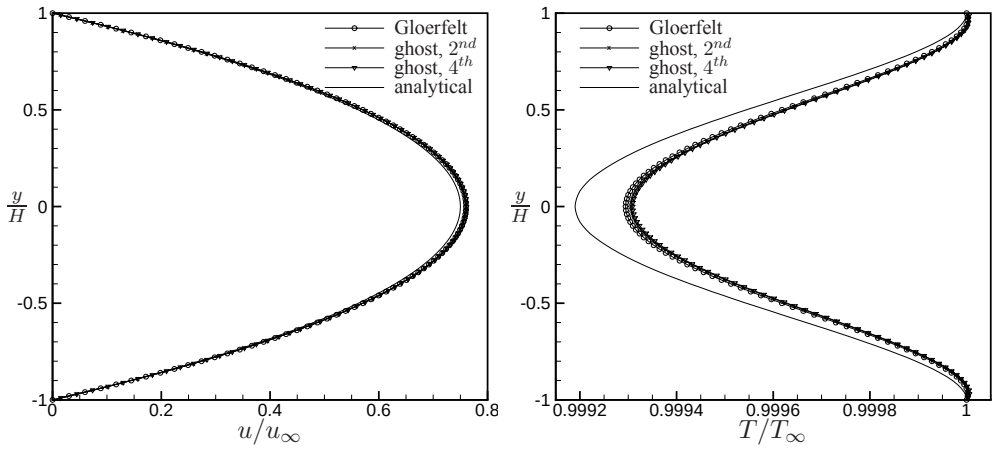

(b) x/h = 7.5

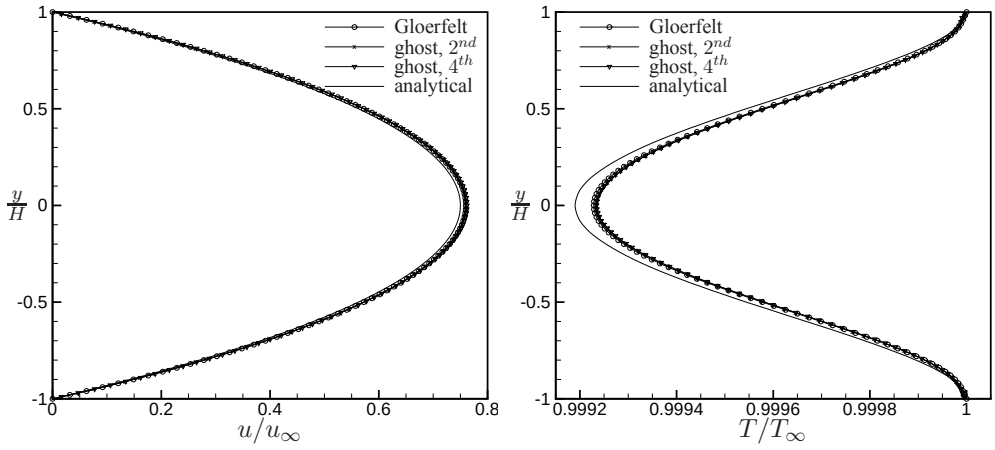

(c) x/h = 10

Figure 2.14 - *Results for a Poiseuille channel flow of length* $= 10h$*. Comparison of Gloerfelt boundary condition with ghost cells method at different distances from the inflow. Left plots: adimensional streamwise velocity profile. Right plots: adimensional temperature profile*

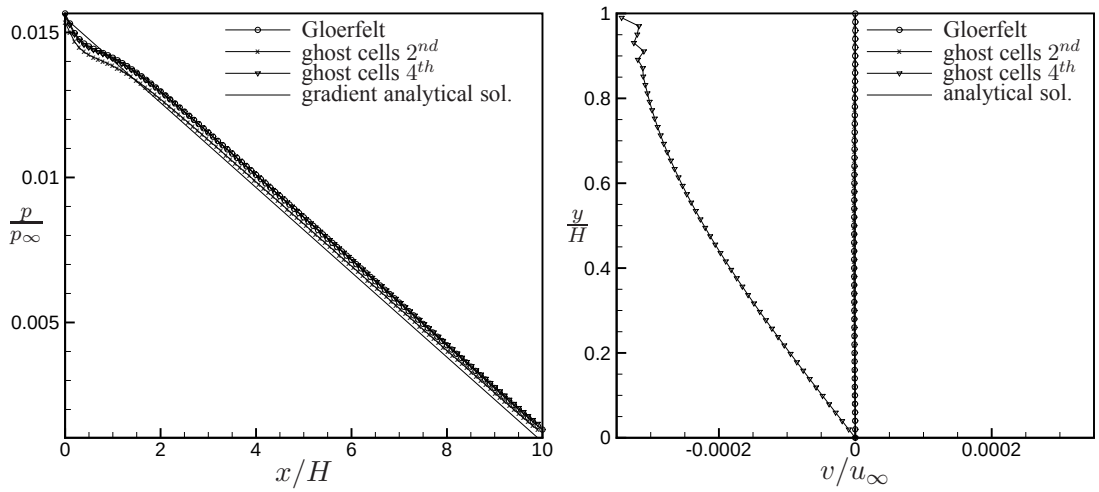

(a) Pressure (b) Normal velocity

Figure 2.15 - *Results for a Poiseuille channel flow of length* $= 10h$*. Adimensional profiles. Left: Pressure along the centerline of the channel* ($y = 0$)*. Right: Normal velocity at* $x/h = 7.5$ *for half of the channel* ($0 < y < 1$)*.*

The pressure gradient has been compared with the analytical solution $\frac{3}{2}\frac{\mu_\infty u_\infty}{h^2}x$. The results are shown in figure 2.15(a), where it is observed that all boundary conditions give good agreement with the theoretical gradient.

Results for the normal velocity profiles have been checked and shown at the location $x/h = 7.5$ in figure 2.15(b). The analytical solution for the normal velocity in a channel flow is zero, but numerically an asymmetrical profile of low-order-magnitude is obtained. For more clarity, only half of the channel is shown in figure 2.15(b). It is observed that the magnitude of the velocity values obtained with the 4^{th} order ghost cells method is higher than those of the other two boundary conditions. Furthermore, these results present small numerical oscillations near the walls. Note that the last point for this case (represented by a triangle ∇) does not correspond to the wall but to the first interior point, that is why its value is not zero.

In wall-bounded flows numerical oscillations may appear, specially with the use of a non-symmetric scheme at the boundary. It is believed that the origin of the oscillations in this case is due to the non-symmetric 4^{th} order scheme used to compute the pressure at the ghost cells, and the absence of a radiation boundary which would allow the small pressure oscillations leave the domain. Nevertheless, the value of the v velocity in this worst case is in the order of $\mathcal{O}(10^{-4})$, and in the other cases is in the order of $\mathcal{O}(10^{-6})$.

On the other hand, it is observed that these oscillations are not propagated inside the computational domain. Moreover, they do not contaminate the solutions of the other variables, since these oscillations are not appreciated in the streamwise velocity and temperature profiles shown in figure 2.14. The reason of this fact might have two explanations. First, since these two profiles are symmetric (which is not the case for normal velocity) the oscillations created at both walls might cancel each other. Second, the magnitude of the values of u velocity and temperature are higher, making more difficult the identification of small numerical fluctuations.

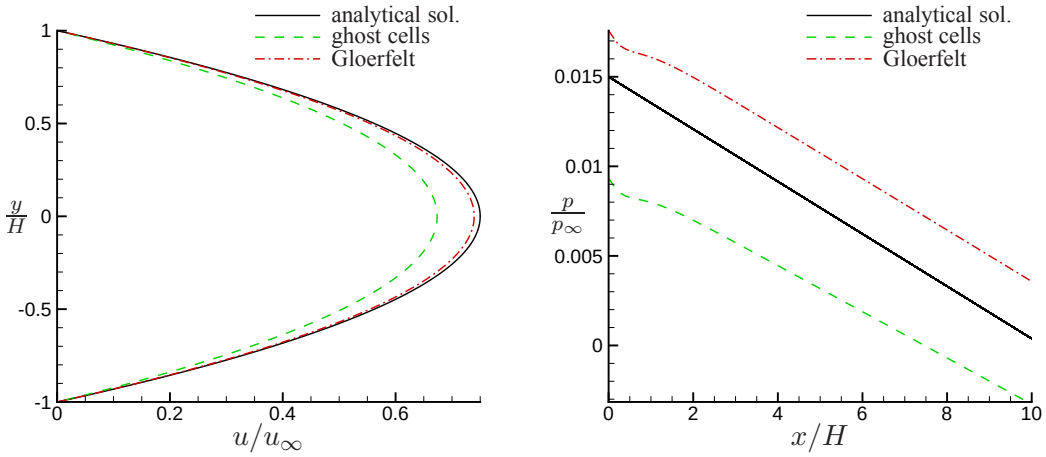

(a) Streamwise velocity at x/h = 2/3

(b) Pressure at y/h = 0

Figure 2.16 - *Results for a Poiseuille channel flow of length* $= 10h$*. Adimensional profiles. Outflow: Poinsot and Lele with* $\sigma = 0.58$*. Comparison of Gloerfelt boundary condition with ghost cells method and analytical solution*

Outf ow boundary conditions

The streamwise velocity and the temperature at the inf ow are imposed to be the analytical solution for a Poiseuille f ow, while normal velocity is imposed to be zero. Giles characteristic boundary conditions are added to avoid ref ections. At the outf ow, the two characteristic formulations described in section §1.4 are used. For the Giles boundary condition, streamwise velocity and the temperature at the outf ow are imposed to be the analytical solution for a Poiseuille f ow. The Poinsot and Lele boundary condition does not need a reference prof le at the outf ow. For both formulations, a pressure gradient is imposed in the direction of the f ow.

At the walls, both the Gloerfelt condition and the ghost cells method are tested. After that, the Gloerfelt boundary condition is selected to study the inf uence of the relaxation parameter σ from equation (1.27). All the simulations are computed during 45000 iterations, in which a stationary solution is obtained.

As before, the computed prof les for u velocity and temperature are used for validation, as well as the pressure gradient. The same adimensional values are utilized: u/u_∞ for velocity, T/T_∞ for temperature, p/p_∞ for pressure and x/h and y/h for the geometrical coordinates.

Firstly the two wall boundary conditions are compared, using the characteristics of Poinsot and Lele with a coeff cient $\sigma = 0.25$. This value is chosen as in the article of Poinsot and Lele [140]. In f gures 2.16(a) and 2.16(b) the two wall boundary conditions are compared. It is clearly shown that Gloerfelt condition gives a velocity prof le much closer to the analytical solution than the ghost cells method, in contrast to the f gures 2.14. In the previous case, where Giles linear characteristics were used at the outf ow, the difference between the two wall treatments was not so pronounced. In that case, a reference prof le is imposed at the outf ow and hence the inf uence of the solid boundaries is smaller. In the formulation of Poinsot and Lele no values are imposed at the outf ow, that is why the effect of the walls on the solution is enhanced.

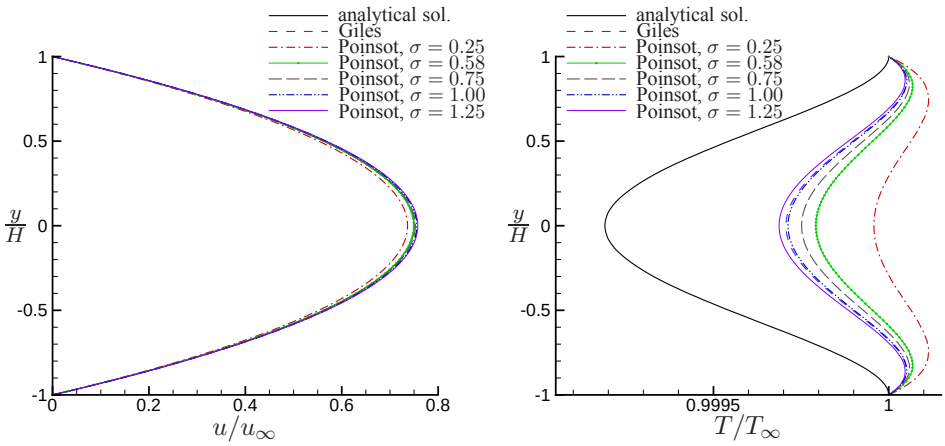

(a) x/h = 1/3

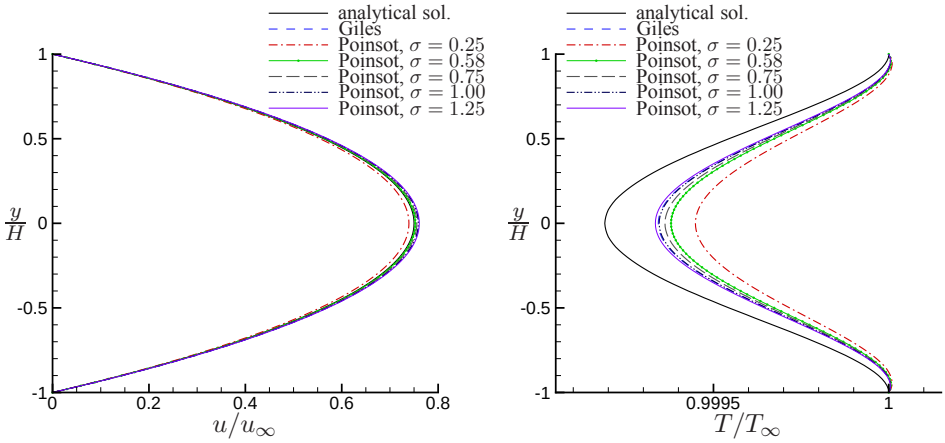

(b) x/h = 2/3

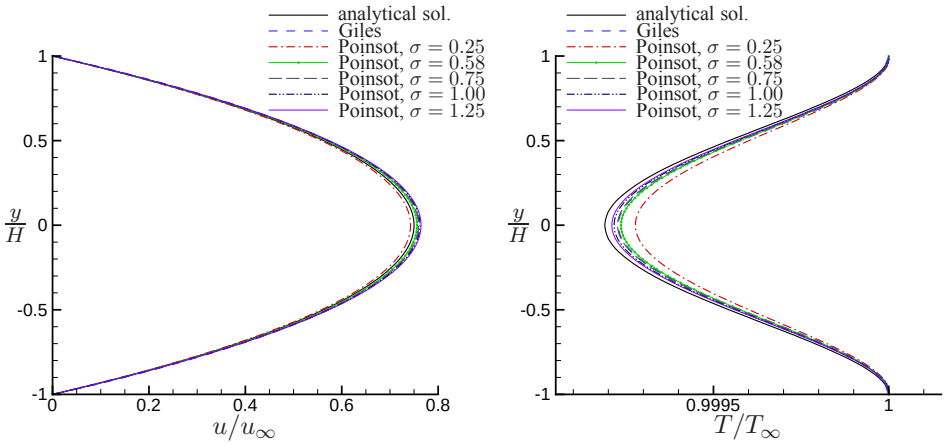

(c) x/h = 10

Figure 2.17 - *Results for a Poiseuille channel flow of length* $= 10h$*. Gloerfelt wall bc. Comparison of Giles boundary condition with Poinsot and Lele using different values for* σ*. Left plots: adimensional streamwise velocity profile. Right plots: adimensional temperature profile*

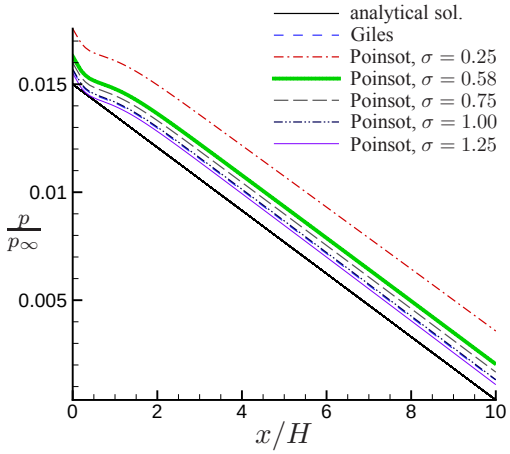

Figure 2.18 - *Results for a Poiseuille channel flow of length* $= 10h$*. Gloerfelt wall bc. Comparison of Giles boundary condition with Poinsot and Lele using different values for* σ*. Adimensional pressure along y/h = 0.*

Since the Gloerfelt wall shows better agreement with the analytical solution than the ghost cells, it is selected to perform the study of the relaxation coeff cient σ. Several runs have been performed using different values: $\sigma = 0.25$ as in the study by Poinsot and Lele [140], $\sigma = 0.58$ as used by Rudy and Strikwerda [154], and three higher values which allow a larger relaxation $\sigma = 0.75, 1.00, 1.25$. These results are compared to the reference solution as well as the prediction obtained using Giles boundary conditions.

Figure 2.17 show the streamwise velocity and temperature prof les for the different values of sigma, at three locations. It is observed that in the interior of the channel, $\sigma = 1.00$ gives the most similar result to the Giles prediction, while at the outf ow this equivalence is achieved by $\sigma = 0.75$. This statement is valid for both u velocity and temperature. By comparison to the analytical solution, $\sigma = 0.58$ gives the best agreement for the velocity prof le. Regarding the temperature prof les, it is observed that the agreement increases with σ, so it is the higher one, $\sigma = 1.25$, the one which approaches more the reference solution.

Finally, f gure 2.18 displays the pressure gradient along the centerline of the channel, i.e. $y/h = 0$. It is diff cult to appreciate in the plot, but $\sigma = 0.25$ gives a gradient slightly different from the analytical solution. However, the deviation is not very signif cant since it is extremely small. All the other values of the coeff cient give excellent agreement with the reference gradient, as it did the Giles outf ow boundary.

In summary, regarding the pressure coeff cient, $\sigma = 0.58$ gives the best agreement for velocity prof les and no signif cant effect is found for the pressure gradient.

2.3 Multi-block test case

All the previous test cases involved single-block geometries. The last step in order to fully validate the code is to compute a problem involving a multi-block geometry. With this aim, the study of a f ow over a surface discontinuity was selected since it is a good preliminary test before simulating a cavity f ow.

2.3.1 Small review

Cavity flow simulations are very complex mainly due to the two corners. The first one presents numerical difficulties due to the sudden flow separation and the creation of a recirculation zone, which can lead to numerical diffusion. The second one receives the impact of the flow which separates again from the horizontal wall creating another recirculation bubble.

The implementation of a backward-facing-step is the first test of the multi-block treatment and multi-block derivation. At the same time, the first corner is investigated in isolation, without the difficulties of having a recirculating flow impacting against a second corner. Flows over a step have been widely used to study flow separation and numerous publications can be found in the literature. The length of the primary recirculation region is often used for comparison between different numerical and experimental studies.

In the case of a backward-facing-step with an incoming boundary layer the flow separates at the leading edge and creates a recirculation zone, whose length depends on the Reynolds number, flow regime (laminar or turbulent) and the geometry. Several authors have investigated this flow with a turbulent boundary layer [103, 109, 118, 162].

Another common step configuration is a laminar channel flow with a sudden expansion. This problem has been commonly used in the literature to evaluate the performance of numerical codes, and hence several numerical and experimental results are available for validation [9, 68, 101, 106]. In this problem, when the channel flow reaches the expansion section, the velocity is suddenly reduced and hence there is a pressure increase. Fluid particles near the lower wall create a recirculation bubble downstream from the step, and one or several small recirculation zones are created at the upper wall.

The final aim of this investigation is the simulation of a cavity flow with an incoming boundary layer. As a consequence, in order to match the characteristics of the cavity flow, an incoming laminar boundary layer upstream from the step is desired. The effects of turbulence are out of the scope of this study, and the simulation of an expansion inside a channel presents some extra difficulties due to the numerical instabilities created inside the asymmetric bounded geometry.

After an extensive literature research, only two publications concerning flows over a backward-facing-step with an incoming laminar boundary layer were found. They are a three-dimensional (3D) numerical investigation by Kaltenbach *et al.* [102] and an experimental and numerical study by Wengle *et al.*[180], who used the same test case. As a consequence, the flow and geometric parameters are selected accordingly to these two studies.

2.3.2 Backward-facing-step with an incoming boundary layer

This study consists on a thin boundary layer which suddenly faces a backward-facing-step, getting separated from the horizontal wall and creating a recirculation zone. The streamwise velocity field is initialized as a Blasius boundary layer as the problem from §2.2.1, with a Mach number $M = 0.1$. The Reynolds number based on the step height D and inlet freestream velocity is $Re_D = 2900$, and based on the boundary layer thickness at the step is $Re_\delta = 580$, and the ratio between the boundary layer thickness δ and the step height is $\delta/D = 0.2$. Normal velocity is initialized as zero, pressure as an homogeneous

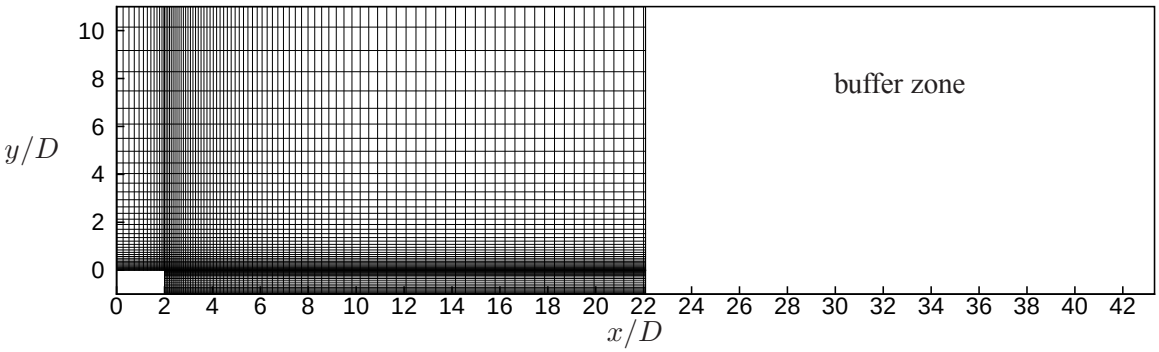

Figure 2.19 - *Backward-facing-step: computational domain and grid. For clarity, only 1 every 5 points is displayed.*

f eld at $p_\infty = 10^5 Pa$ and density as an homogeneous f eld calculated from $\rho_\infty = p_\infty / rT_\infty$, where $T_\infty = 298K$.

The computational domain, shown in f gure 2.19, consists on an inlet section of $2D$ upstream from the step, a section of $20D$ downstream of the step and a buffer zone. The expansion ratio $\text{height}_{outflow}/\text{height}_{inflow}$ is 1.09, where the inlet height is $11D$. The grid is not equidistant, it is ref ned near the step in both the vertical and horizontal directions and close to the walls.

The domain is composed of 3 blocks: the inlet $x \leq 2$ is block 1, and for $x \geq 2$ and above $y = 0$ is block 2 and below $y = 0$ is block 3. Block 1 is composed of 61×200 points with a 2% of geometric ratio increment in both directions. Block 2 contains 387×200 points, and the geometric ratio increments are 0.7% and 2% in *x*- and *y*-directions respectively. The grid in the f ow direction of block 3 is as block 2, and in the normal direction the number of points is 100 with 2.5% of geometric ratio increment.

The buffer zone is constructed in an equivalent way to the problem §2.2.1, i.e. a stretched mesh with a 2.5% geometric ratio increment and a f lter proposed by Lele [119]. It contains 50 points in the f ow direction.

The inf ow and radiation boundary conditions are the characteristics of Giles. Moreover, a numerical solution of the Blasius similarity equation for a laminar boundary layer is imposed at the inf ow. Since the mean velocity prof les at the outf ow are unknown, the characteristic formulation of Poinsot and Lele with $\sigma = 1$ is used at the outf ow. The 4^{th} order ghost cells method has been used for the solid boundaries, which are considered isothermal and non-slip.

The time step is calculated according to the stability criterion described in §1.3.2; for this simulation a Courant number of 0.65 is used. The simulation is computed for a non-dimensional time of $\tilde{t} \simeq 450D/u_\infty$, where u_∞ is the mean freestream velocity in x-direction, calculated as $u_\infty = Mc_\infty$, with c_∞ being the ambient speed of sound calculated as $c_\infty = \sqrt{\gamma p_\infty / \rho_\infty}$. A residence time of $\tilde{t}_r \simeq 220D/u_\infty$ is necessary to get a stationary solution and this data is not used for statistics.

The instantaneous vorticity contours ω during one period $\mathcal{T}$ are shown in f gure 2.20, where vorticity has been normalized by u_∞/D and the absolute value has been taken. The incoming boundary layer separates at the leading edge forming a primary recirculating zone, and a smaller secondary vortex at

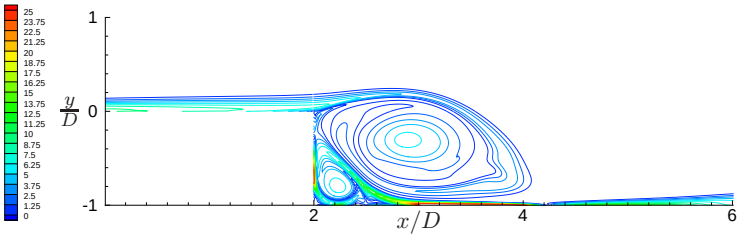

(a) t = 0

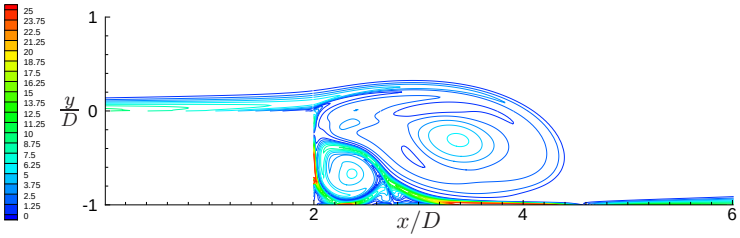

(b) t = 0.2 $\mathcal{T}$

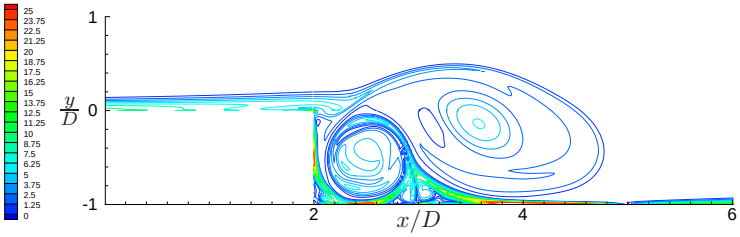

(c) t = 0.4 $\mathcal{T}$

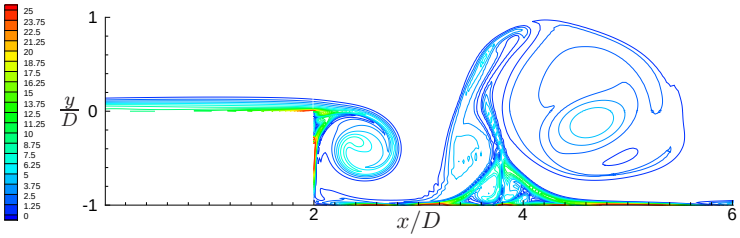

(d) t = 0.6 $\mathcal{T}$

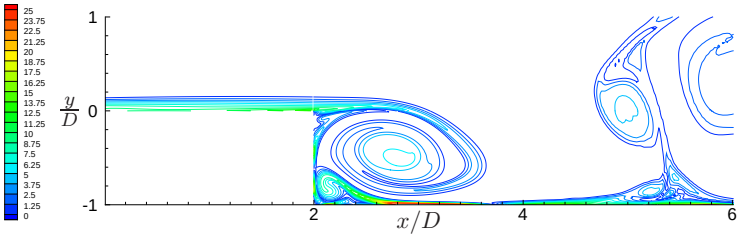

(e) t = 0.8 $\mathcal{T}$

Figure 2.20 - *Instantaneous adimensional vorticity contours $\omega D/u_\infty$ during one period. 21 equidistant isocontours from 0 to 25. DNS prediction*

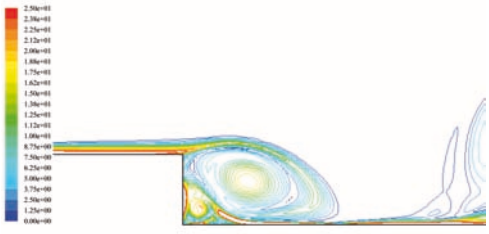

(a) t = 0

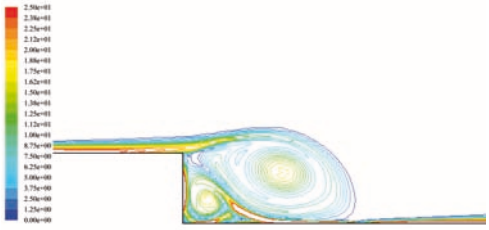

(b) t = 0.2 $\mathcal{T}$

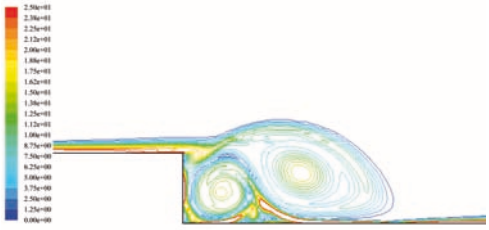

(c) t = 0.4 $\mathcal{T}$

(d) t = 0.6 $\mathcal{T}$

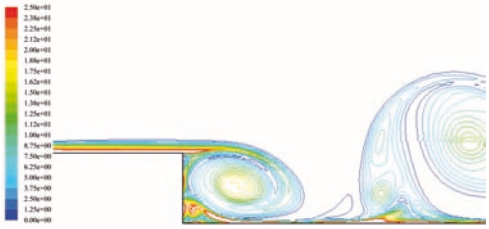

(e) t = 0.8 $\mathcal{T}$

Figure 2.21 - *Instantaneous adimensional vorticity contours $\omega D/u_\infty$ during one period. 21 equidistant isocontours from 0 to 25. FLUENT prediction*

the corner. The primary vortex becomes larger and larger, until it detaches from the leading edge and it is convected downstream. At that moment, the secondary vortex is attached to the incoming boundary layer, becoming the primary vortex and a new one is created at the corner, completing the period.

These results, however, cannot be validated with the studies of Kaltenbach *et al.* [102] and Wengle *et al.*[180]. The former consists of experimental and 3D DNS simulations, and the latter is a 3D numerical investigation. Consequently, both of them involve three-dimensional effects which cannot be compared with the present 2D computation. Both publications report a free shear layer emanating from the leading edge, which for a long distance divides a turbulent separation region below and a non-turbulent above. Finally, the shear layer undergoes transition to turbulence prior to re-attachment to the horizontal wall.

It is for this reason that another 2D numerical simulation, using the commercial software FLUENT, has been performed. Numerical Simulation of low-order accuracy of the incompressible Navier-Stokes equations has been used. The computational domain for this case is of the same size as the high-order-scheme DNS, with a grid ref ned in *y*-direction near the walls and in the shear layer, while the grid in *x*-direction is equidistant. In total there are around 165000 points, in which the step is discretized with 30 points. The inf ow is def ned as a polynomial approximation of a laminar boundary layer [75]:

$$u(y) = u_\infty \left(\frac{y}{\delta}\right)\left[2 - 2\left(\frac{y}{\delta}\right)^2 + \left(\frac{y}{\delta}\right)^3\right] \tag{2.1}$$

where u_∞ is the freestream velocity and δ is the boundary layer thickness at each streamwise position. The results have been normalized in order to be compared to the compressible DNS results, and they are shown in f gure 2.21. It is seen that the agreement between both numerical predictions is very good.

To further cross-validate the results, a time history of the vorticity at $(x, y) = (3D, 0)$ has been recorded to f nd the frequency of oscillation. The results of the Fast Fourier Transform (FFT) of the adimensional vorticity are displayed in f gure 2.22. As shown, the predicted frequencies of oscillation are $St_D = fD/u_\infty = 0.068$ from the DNS and $St_D = 0.058$ from FLUENT. It must be noted that the FLUENT results are much less accurate, and the FFT has been done using a less number of points, which might explain the slight difference of values.

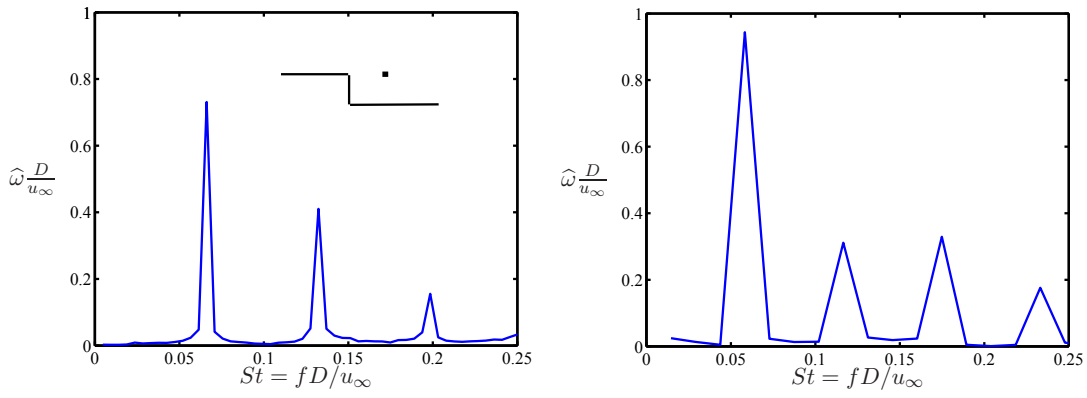

(a) DNS (b) FLUENT

Figure 2.22 - *Results for backward-facing-step. Spectrum of vorticity fluctuations at* $(x, y) = (3D, 0)$.

As it is to be described in chapter §3, cavity flows present two modes of oscillation: shear layer mode, and wake mode. The presented flow over a backward-facing-step behaves like a cavity flow on wake mode: creating large vortices downstream from the step, which become larger and larger and separate from the incoming boundary layer. Cavity flows on wake mode at low Mach number have been reported to oscillate at a Strouhal number $St_D = 0.064$ [151], giving good agreement with the obtained DNS results. This fact confirms that they show the same phenomena, and it validates the results for the backward-facing-step.

Furthermore, as it is to be discussed in chapter §3, the wake mode of a cavity is extremely difficult to observe in experiments and 3D simulations, which tend to lead to a shear layer mode. This might be the reason why the studies of Kaltenbach *et al.* [102] and Wengle *et al.* [180] report different flow physics than the present 2D investigation.

2.4 Conclusions

In this chapter several test cases have been performed in order to validate different parts of the code.

The non-dispersive and non-dissipative properties of the scheme are good, as proved by the aeroacoustic test cases §2.1.1, §2.1.2, §2.1.3 and §2.1.5. In all of them the results in the interior points perfectly overlap the analytical solutions, even with the waves propagating with a certain angle respect to the Cartesian grid. No extra filtering is needed.

The non-reflecting boundary conditions have been tested in problems §2.1.1, §2.1.2 and §2.2.2. The characteristic boundary conditions of Giles have been found to give very good results when the waves cross the boundaries perpendicularly (§2.1.1), and present only small deviations when there is a tangential mean flow (§2.1.2). The asymptotic boundary conditions of Tam and Dong have been used only in the first problem §2.1.1, for which the results obtained are identical to those from the characteristic formulation.

The characteristic formulation of Poinsot and Lele gives the same results as the method of Giles in the aeroacoustic problems §2.1.1 and §2.1.2. The channel flow in §2.2.2 has been used to study the influence of the relaxation coefficient σ, where it is found that $\sigma = 0.58$ gives the best agreement for velocity profiles and no significant effect is found for the pressure gradient. The effectiveness of the boundary condition is validated, but a separate investigation of σ is required for each particular case.

The solid boundary conditions have been tested in §2.1.3, §2.1.4 and §2.1.5 for aeroacoustic applications. Both formulations, Gloerfelt and ghost cells (with a 2^{nd} and 4^{th} order schemes), have been validated, since all the results match very well with the analytical solutions. For the test case §2.1.4 there is no reference solution, but the results have been cross-validated and the differences observed due to the viscosity effects have been physically explained. Moreover, the multiple wall reflection in problem §2.1.5 shows the good performance of the corner treatment.

The viscous test cases §2.2.1 and §2.2.2 have been used to test the effectiveness of the wall boundary conditions in very low Reynolds number flows. Gloerfelt boundary conditions are designed to be applied over the convective fluxes, and it has been proved in §2.2.1 that they do give better accuracy than when they are applied over the total fluxes. Both kinds of boundary conditions (Gloerfelt and ghost cells) give

satisfactory results. Only in the case of a channel, where the flow is enclosed and there is no radiation boundary, the 4^{th} order non-centered scheme used in the ghost cells method creates oscillations of a very small magnitude in the normal velocity.

For the simulation of a cavity flow, the Giles formulation is selected for the inflow and radiation boundaries, and the method of Poinsot and Lele is to be used at the outflow. The ghost cells boundary condition with a 4^{th} order scheme is chosen for the walls. All these conditions are integrated in a multi-block problem §2.3.2, consisting of a flow over a backward-facing-step. The results show a good prediction of the instantaneous flow field as well as the frequency of oscillation. Consequently, the numerical method is suitable for the simulation of unsteady flows over surface discontinuities, such as a cavity.

Chapter 3

Cavity f ow simulation analysis

Ecoulements de cavité : résultats

L'augmentation du transport aérien combiné à une préoccupation grandissante pour la préservation de l'environnement ont suscité l'intérêt pour les études aéroacoustiques des écoulements instationnaires autour des avions, ces écoulements produisant à la fois de fortes forces de trainées ainsi que de forts bruits aérodynamiques. Dans les configurations de type cavité, présentes dans de nombreuses applications industrielles, le développement de stratégies de contrôle d'écoulement pour la réduction de la trainée et du bruit est tout particulièrement intéressant.

Or, dans la simulation numérique de ce type d'écoulement au-dessus de cavité, l'influence de la condition initiale a été peu étudiée mais pourrait jouer un rôle important quant aux résultats numériques obtenus. L'objectif de ce chapitre est d'étudier l'effet de cette condition initiale dans des simulations d'écoulement bidimensionnel au-dessus de cavités rectangulaires. Nous nous sommes tout particulièrement intéressés aux modes d'oscillation de l'écoulement, que l'on doit bien connaître si l'on veut plus tard contrôler l'écoulement.

Ecoulements de cavité

Les oscillations de l'écoulement au-dessus d'une cavité apparaissent au delà de nombres critiques de Mach M et de longueur adimensionnelle de la cavité L/θ, où θ est l'épaisseur de quantité de mouvement de la couche limite à l'entrée de la cavité.

Le mode d'oscillation de type 'couche de cisaillement', appelé aussi mode de Rossiter, se caractérise par une séparation de la couche limite au premier coin supérieur de la cavité formant une couche de cisaillement oscillante qui impacte sur le mur vertical de la cavité en aval. Pour des nombres de Mach subsoniques suffisamment élevés, l'interaction entre les petites instabilités dans la couche de cisaillement avec la marche ascendante de la cavité génère des ondes de pression : une partie de ces ondes se propage vers l'amont, renforçant ainsi le lâcher tourbillonnaire dans le couche de cisaillement, et une autre partie s'échappe de la cavité en étant perçue au loin comme du bruit. Ce mécanisme est un mécanisme de résonance aéroacoustique auto-entretenu dans lequel les modes d'oscillation dépendent du nombre

de Mach. Dans leur article de revue, Rockwell et Naudascher [146] le nomme le 'fluid-resonant mode'.

Pour des nombres de Mach plus bas, les oscillations de l'écoulement sont dûes à l'instabilité de la couche de cisaillement au-dessus de la cavité, et les modes d'oscillation ne dépendent alors pas du nombre de Mach. Ce mécanisme est appelé un 'fluid-dynamic mode' par Rockwell et Naudascher [146].

Quand les paramètres L/D, M, Re et/ou L/θ augmentent, l'écoulement n'oscille alors plus suivant un mode de couche de cisaillement mais suivant un mode de 'sillage'. Le mode de sillage se caractérise par le ré-attachement de l'écoulement à la paroi du fond de la cavité, et par une forte augmentation de la trainée. Des tourbillons de grande taille (environ la même taille que la hauteur de la cavité) sont créés au coin supérieur le plus en amont de la cavité, et éjectés en aval de la cavité. Ce lâcher tourbillonaire est très similaire à celui produit à l'arrière d'un culot, d'où le terme de sillage. C'est un phénomène auto-entretenu où la fréquence d'oscillation est pratiquement indépendante du nombre de Mach [151], démontrant ainsi son caractère hydrodynamique et non de résonance aéroacoustique.

Les cavités peuvent être qualifiées de profondes, 'deep', ou peu profondes, 'shallow', suivant leur rapport largeur sur profondeur L/D. Rossiter [150] définit comme profondes les cavités pour lesquelles $L/D < 4$, et peu profondes celles pour lesquelles $L/D > 4$, tandis que Sarohia [156] utilise lui le seuil limite de 1 comme critère de discrimination des cavités. Etant donné que dans le cas subsonique les cavités avec $L/D < 4$ oscillent en mode couche de cisaillement, tandis que celles avec $L/D > 4$ peuvent osciller soit en mode couche de cisaillement soit en mode de sillage, c'est le critère de Rossiter que nous utiliserons.

Validation

La méthode numérique a été validée en reproduisant un cas test étudié par plusieurs auteurs [21, 76, 151, 152], et qui consiste à simuler un écoulement de couche limite arrivant au-dessus d'une cavité profonde de rapport largeur sur profondeur $L/D = 2$. L'écoulement est compressible de nombre de Mach $M = 0.6$, son régime est laminaire avec un nombre de Reynolds basé sur la profondeur de cavité de $Re_D \approx 1500$.

Cette configuration oscille en mode couche de cisaillement. La figure 3.9 montre les iso-contours de vorticité instantannée à deux instants différents de la période d'oscillation. La figure 3.10(a) représente quant à elle les iso-contours de dilation, et montre que la propagation des ondes acoustiques se fait dans une direction faisant un angle de 135° par rapport à la direction aval. Ces résultats sont en bon accord avec ceux de Rowley et al. [152, 151].

Un maximum d'intensité acoustique de 154dB a été trouvé au voisinage du côté aval de la cavité, ce qui est en bon accord avec les résultats de Brès [21]. L'écoulement oscille à des nombres de Strouhal de $St_1 = f_1 L/u_\infty = 0.39$ et $St_2 = f_2 L/u_\infty = 0.75$, ce qui correspond aux modes de la formule de Rossiter [150] de l'équation 3.1, ainsi qu'aux prédictions de Gloerfelt [76].

Résultats pour une cavité profonde

Deux configurations différentes ont ensuite été sélectionnées afin d'étudier l'influence des conditions initiales : une cavité profonde et une autre peu profonde. Pour chacune de ces configurations, différentes conditions initiales ont été testées afin d'observer leur influence sur le changement de mode d'oscillation.

La première partie de cette étude concerne une cavité profonde de rapport largeur sur profondeur de

$L/D = 2$ et à nombre de Mach $M = 0.6$. Les écoulements laminaires au-dessus des cavités profondes oscillent en mode de couche de cisaillement, mais il y a désaccord entre les auteurs sur le mode dominant. La figure 3.13 montre que l'amplitude des modes d'oscillation change dans le temps. Au début de la simulation nous trouvons deux modes de Rossiter (St_1 et St_2), mais ensuite l'amplitude du premier mode décroît jusqu'à complètement disparaître.

La vitesse d'écoulement à l'intérieur de la cavité est initialisée à zéro, et cinq conditions initiales différentes ont été implémentées au-dessus de la cavité : écoulement de couche limite de Blasius d'épaisseur δ croissante, écoulement de couche limite de Blasius d'épaisseur δ constante, approximation polynomiale d'une couche limite, écoulement uniforme de vitesse u_∞, et enfin vitesse initiale nulle. Dans tous les cas nous convergeons vers la même fréquence d'oscillation correspondant au second mode de Rossiter. Cependant, avec la dernière condition initiale (vitesse initiale nulle), c'est le premier mode de Rossiter qui domine au début de la simulation. Nous avons également observé que la directivité de la radiation acoustique était plus prononcée quand le mode dominant est le second mode de Rossiter. Quant à l'intensité acoustique, la condition initiale ne semble avoir aucun effet sur elle.

Résultats pour une cavité peu profonde

La cavité peu profonde choisie pour cette étude a un rapport largeur sur profondeur de $L/D = 4$ et l'écoulement est à faible nombre de Mach $M = 0.15$. Pour cette configuration Rowley et al. [151] ont trouvé une oscillation en mode de couche de cisaillement pour des nombres de Mach inférieur à 0.3 quand $L/\theta = 102$, tandis que Larsson et al. [116] ont trouvé une oscillation en mode de sillage pour les mêmes conditions d'écoulement et de géométrie pour un nombre de Mach de 0.15. Ces deux études ont été réalisées par simulation numérique directe des équations bidimensionnelles compressibles de Navier-Stokes, en utilisant des schémas d'ordre élevé et des conditions aux limites non réfléchissantes. La seule différence apparente entre les deux simulations est la condition initiale. Rowley et al. a initialisé le champ de vitesse par un écoulement de couche limite de Blasius au-dessus de la cavité et nul à l'intérieur de la cavité [151], tandis que Larsson et al. a initialisé à zéro la totalité du champ d'écoulement (communication privé de l'auteur).

Nous avons donc considéré trois types de conditions initiales au-dessus de la cavité : écoulement uniforme, écoulement nul et écoulement de couche limite de Blasius. La première condition initiale (écoulement uniforme) conduit à un mode de couche de cisaillement oscillant suivant le second mode de Rossiter. La seconde condition initiale (écoulement nul) conduit à un mode de sillage, où le nombre de Strouhal est $St_D = fD/u_\infty = 0.061$, la même valeur que celle trouvée par Larsson et al. [116]. La dernière condition initiale (écoulement de couche limite) conduit à un mode de couche de cisaillement avec une modulation de basse fréquence.

Plusieurs simulations ont été réalisées en modifiant le nombre de Mach ou l'épaisseur de couche limite. Les résultats suggèrent que quand le nombre de Mach ou L/θ augmente l'ambiguité concernant le mode d'oscillation disparaît avec la dépendance de l'écoulement à la condition initiale.

Conclusions

Différentes configurations d'écoulement au-dessus d'une cavité ont été simulées. Pour les cavités profondes, les résultats de cette étude ainsi que d'études précédentes montrent que le mode dominant de l'oscillation de la couche de cisaillement peut être difficile à prédire. Suivant la condition intiale et le temps de simulation, le mode dominant trouvé est soit le premier soit le second mode de Rossiter.

Ceci suggère que pour le contrôle de ce type d'écoulement les fréquences ciblées devraient être les deux premiers modes de Rossiter, la focalisation sur la suppression/diminution d'un seul d'entre eux pouvant sans doute conduire à l'augmentation en amplitude de l'autre.

L'effet de la condition initiale est encore plus important sur la cavité peu profonde, puisqu'elle peut conditionner le régime d'oscillation. Ceci implique donc de choisir avec précaution la condition initiale. Ainsi, dans le cas particulier d'une cavité avec $L/D = 4$, $M = 0.15$ et $L/\theta = 96$, une initialisation avec un écoulement uniforme conduit à un écoulement oscillant en mode de couche de cisaillement, alors qu'une initialisation avec une vitesse nulle conduit à un écoulement oscillant en mode de sillage. Un écoulement oscillant en mode de sillage produisant une trainée et un bruit plus important qu'en mode de couche de cisaillement, il peut être intéressant dans ce cas de forcer l'écoulement en régime de couche de cisaillement si l'on veut réduire trainée et bruit. Les paramètres d'écoulement pour lesquelles les résultats sont ambigus ont été identifiés, montrant que dans le cas de nombre de Mach plus grand ou de couche limte plus épaisse l'influence de la condition initiale disparaît.

Introduction

The unsteady flow over a surface cut-off produces the emission of acoustic waves. Flow control strategies for noise and drag reduction are being developed, especially in wall-bounded configurations with an industrial application such as cavities.

At the beginning of this chapter a literature review of cavity flow physics is given (§3.1), with a particular emphasis to shear layer and wake mode oscillations. Aeroacoustics and three-dimensional effects are also discussed.

It is observed that the influence of the initial condition is an issue to which has been given little attention in previous studies, but which might play an important role in the numerical results found for the cavity flow oscillations. The objective of this chapter is to investigate the effect of the initial condition in 2D numerical simulations, relating the results to other 2D and 3D numerical studies as well as experimental results. The investigation is mainly focused on the oscillation modes, since they are of special interest for future applications of flow control. Due to the importance of noise emission from cavities in the aeronautical and automotive industries, the aeroacoustics of rectangular cavities is also discussed.

A test case from the literature is repeated in order to validate the numerical method, boundary conditions and grid (§3.2). After that, the influence of the initial condition on DNS simulations of laminar flows over cavities is addressed.

For this aim, two different configurations are selected: a cavity of $L/D = 2$ and moderate Mach number $M = 0.6$, clearly oscillating in shear layer mode (§3.3); and a cavity of $L/D = 4$ and low Mach number $M = 0.15$, whose results respect to the flow regime are contradictory (§3.4). For each configuration different initial conditions are used, keeping all the other parameters constant, in order to observe the changes in oscillation modes due to the initial condition.
Part of these results have been submitted as an article to Computers and Fluids [133].

3.1 The physics of cavity f ows

Cavity f ows are very complex even though the geometry is very simple. They have been largely studied from the 50's, experimentally [71, 150], theoretically [96, 166] and by numerical simulations [151, 159]. Cavities are often referred as being *deep* or *shallow*, where the length-to-depth ratio L/D is used as a cut-off. Rossiter[150] def nes deep cavities as those with $L/D < 4$ while shallow cavities have $L/D > 4$, whereas according to Sarohia [156] the cut-off is 1.

There is a good agreement between numerical and experimental studies concerning cavities with $L/D < 4$, which show that they oscillate in shear layer mode (see, for example, the studies cited in tables 3.6 and 3.7 at the appendix of this chapter). On the other hand, results of cavities with $L/D \geq 4$ are ambiguous, since they oscillate in shear layer or wake mode depending on a wide range of parameters, as shown in table 3.8 (appendix of this chapter). It is for this reason that the cut-off of 4 used by Rossiter to def ne deep or shallow cavity is preferred for this work.

3.1.1 Classif cation of cavity f ows

Flows past rectangular cavities have been described previously by several authors. There are critical values of Mach number M, Reynolds number based on the cavity depth Re_D and length of the cavity with respect to the momentum thickness L/θ beyond which oscillations appear as shown in f gure 3.1. These parameters trigger the f ow into the supercritical region of stability where it oscillates.

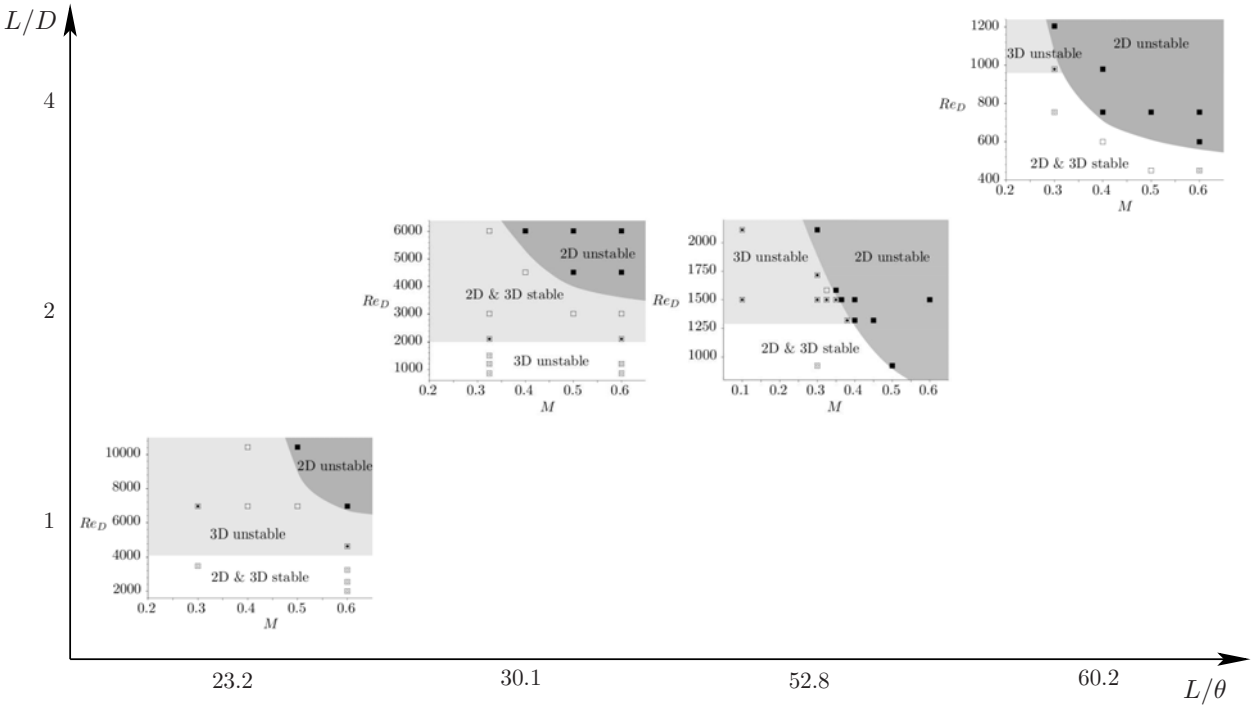

Figure 3.1 - *Schematic of the neutral stability curve for cavity flows. 2D stable □, 2D unstable ■, 3D stable ○, 3D unstable ●. Results from Brès [21].*

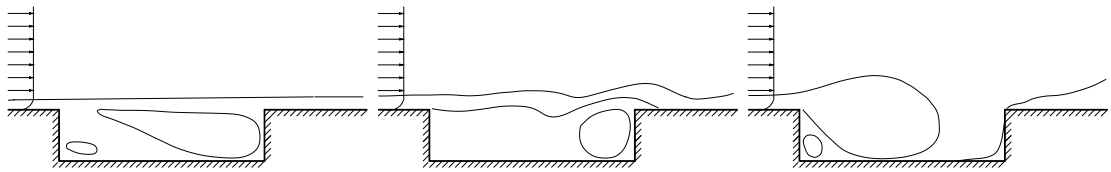

(a) Non-resonant (b) Shear layer mode (c) Wake mode

Figure 3.2 - *Classification of subsonic cavity flows*

The subsonic cavity flows can be classified into non-resonant cavities, cavities oscillating in shear-layer mode, and cavities oscillating in wake mode, as illustrated in figure 3.2.

Non-resonant cavities Grace *et al.* [81] compared experimentally a non-resonant cavity of $L/D = 4$ with a laminar and a turbulent incoming boundary layer at very low Mach number. It is shown by the streamlines that the turbulent case presents a single vortex, while in the laminar case there is a main vortex localized next to the trailing edge, and a smaller vortex, counter-rotating, at the corner of the upstream wall as shown in figure 3.2(a). On the other hand, Ukeiley and Murray [174] observed a similar counter-rotating vortex near the leading wall for a turbulent flow at $M = 0.17$ over a non-resonant cavity of $L/D = 5.16$. Hassan *et al.* [90] investigated by PIV experiments a deep cavity of $L/D = 0.2$ with an incoming turbulent boundary layer at $5\,m/s$, and found it to be non-resonant. Nonetheless, vortical structures are identified in the shear layer which are convected downstream and ejected over the trailing edge.

Shear-layer mode The shear layer mode, also called Rossiter mode and illustrated in figure 3.2(b), is characterized by an incoming boundary layer which separates at the leading edge of the cavity forming an oscillating shear layer which impacts at the downstream vertical wall. At high subsonic Mach numbers the interaction of the small instabilities in the shear layer with the forward-facing-step generate pressure waves: part of them are propagated upstream and reinforce the vortex shedding in the shear layer, and another part escape the domain being perceived far-field as noise. It is a self-sustained, flow-acoustic resonance mechanism in which the oscillation modes depend on the Mach number. This mechanism is referred to as fluid-resonant mode in the review done by Rockwell and Naudascher [146].

For lower Mach numbers, the oscillations of the flow are due to the instability of the shear layer spanning over the cavity, in which there is a periodic inflow and outflow. This mechanism is described as a fluid-dynamic mode by Rockwell and Naudascher [146], and the oscillation modes do not depend on the Mach number.

There is a third regime described in the review by Rockwell and Naudascher [146], called fluid-elastic mode, in which the oscillations are due to the elastic displacement of a solid boundary. This mode might be found, for example, when one part of the cavity is being actuated. This mode regime has attracted little attention and there are only a few studies available. For example, Cody *et al.* [36] performed an experimental investigation to study the fluid-elastic lock-in of a shallow cavity, and they found that it is indeed difficult to achieve.

Wake mode When the parameters L/D, M, Re and/or L/θ increase, the flow no longer oscillates in shear layer mode but in wake mode. The wake mode is characterized by the reattachment of the flow at the bottom wall of the cavity as displayed in figure 3.2(c) and by a high increase of the

drag. Large scale vortices (about the size of the cavity depth) are created at the leading edge and ejected downstream from the cavity. The shedding of vortices resembles those behind a bluff body, therefore its name. The system is self-sustained and the oscillation frequency becomes nearly independent of the Mach number [151], showing that it is of hydrodynamic nature and not a flow-acoustic resonant mechanism.

For transonic and supersonic flows where shocks form above the cavity another classification exists: open, closed, transitionally open, and transitionally closed [80]. In open cavities the shear layer spanning over the cavity reattaches at the downstream wall, like in the shear-layer mode. In closed cavities the shear layer reattaches to the bottom wall, and there is a secondary separation before reaching the downstream wall. Transitionally closed cavities present one single shock wave which is a coalescence of the impingement shock and the exit shock. Finally, in transitionally open cavities there is a series of expansion and compression wavelets.

The cut-off between open and closed cavities is not clearly defined. Plentovich *et al.* [138] and Tracy and Plentovich [172] investigated experimentally subsonic and transonic turbulent flows from $M = 0.2$ to $M = 0.95$ for cavities with $1 \leq L/D \leq 17$. By static pressure measurements it was found that the transition between non-oscillating and open cavity occurs for L/D ratios varying from 6 to 8, and from open to closed cavities from 9 to 15, depending on the flow and the Mach number [138]. From the unsteady pressure measurements it was concluded that open and transitional cavities are always resonant, but closed cavities might be resonant or not [172].

3.1.2 Shear layer mode

In the pioneer experimental work of Krishnamurty [111] a cavity with $L/D = 2$ was investigated by hot-wire measurements and the Schlieren technique. Laminar and turbulent transonic flows ranging from $M = 0.7$ to $M = 0.95$ were considered, and the results show that the laminar cases oscillated at a single frequency, while the turbulent cases presented two dominant frequencies.

Rossiter [150] performed an experimental investigation involving a wide range of Mach numbers ($0.4 \leq M \leq 1.2$) and cavity length-to-depth ratios ($1 \leq L/D \leq 10$). From the obtained results and the idea of a feedback cycle for the cavity, Rossiter derived an empirical formula to predict the oscillation frequency:

$$St_n = \frac{f_n L}{u_\infty} = \frac{n - \alpha}{M + \frac{1}{\kappa}}, \qquad n = 1, 2, ... \tag{3.1}$$

where St_n is the Strouhal number of the mode n corresponding to the frequency f_n, u_∞ is the mean flow velocity, L is the cavity length, M is the Mach number and α and κ are empirical parameters, defined experimentally by Rossiter as $\alpha = 0.25$ and $\kappa = 0.57$.

Tam and Block [166] proposed an alternative model in which the finite shear layer effects and the acoustic reflections from the bottom and upstream wall were taken into account. According to their description of the acoustic wave generation process, during the downward motion of the cycle there is an inflow of external fluid into the cavity, creating a compression wave which is propagated in all directions.

On the other hand, during the upward motion the shear layer shields the trailing edge from the external flow and no pressure waves are emitted.

Tam and Block validated their alternative formula against experimental data for Mach number flows from $M = 0.05$ to $M = 0.4$. The results show a very good agreement for Mach numbers greater than 0.2. Also the Rossiter formula has been shown to provide better agreement for high Mach number flows [165], when the fluid-resonant mode is present. Howe [96] studied theoretically very low Mach number flows in order to cover this range.

Experimental and numerical results from the past years show, in general, good agreement with the Rossiter formula for the oscillation modes. However, the formula does not predict which is the dominant mode, and the results concerning this point are still ambiguous. Rossiter [150] found that generally in deep cavities there is one peak much larger than others, showing that a periodic component predominates, while shallow cavities present two or more peaks, suggesting that the random component is more important.

Brès and Colonius [23] performed a wide range of numerical simulations using 2D DNS including cavities of $L/D = 1, 2, 4$, with laminar subsonic flows at $0.2 \leq M \leq 0.6$ and several L/θ, finding that, in general, higher Rossiter modes are found at higher Mach numbers and L/θ ratio. Previous results reported by Rowley *et al.* [151], who also performed 2D DNS simulations in similar configurations, agree that higher Mach number flows present a higher dominant mode.

Results from experiments and numerical simulations of a ducted cavity have suggested that the existence of an upper wall might create reflections which produce an acoustic coupling, promoting an amplification of the modes or the harmonics. This fact was observed in the wind tunnel experiments performed by Forestier *et al.* [65] of a turbulent flow at $M = 0.8$ over a very deep cavity of $L/D = 0.42$. The flow was found to be highly two-dimensional, but the dominant mode and its harmonics did not show good agreement with the Rossiter prediction. The same configuration was studied by 3D LES by Larchevêque *et al.* [115], who found the same phenomenon for a ducted cavity, and verified that there was indeed a coupling, since by removing the upper wall the harmonics were reduced, and the second, third and fourth modes were recovered. By modifying the value of α into the Rossiter formula (3.1) a good prediction of the modes was obtained. Emmert *et al.* [58] also found a coupling between the cavity flow and the pressure oscillations in a ducted cavity by 3D LES.

It is well understood that the number of shear layer oscillations spanning over the cavity is related to the dominant oscillation mode. The first Rossiter mode corresponds to one single wave, the second mode to two waves, etc., as displayed in figure 3.3. It was first observed by Gharib and Roshko [71] in their water experiments, and it has also been shown in the Schlieren images taken by Kegerise *et al.* [104] in a wind tunnel.

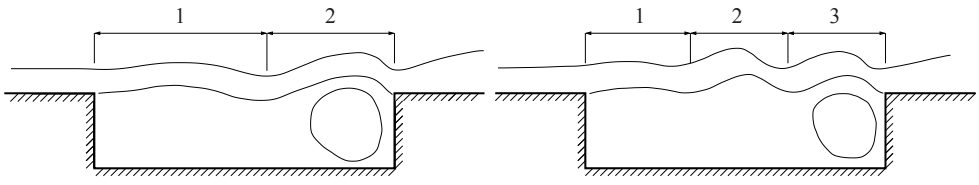

(a) St_2 (b) St_3

Figure 3.3 - *Number of waves of the shear layer related to the oscillation mode*

Recently a phenomenon called *mode-switching* has been investigated. *Mode-switching* refers to a process in which the dominant energy changes temporally from one Rossiter mode to another. It was observed for the first time by Cattafesta *et al.* [26] in their experiments with a turbulent flow over cavities of $L/D = 2$ and 4, and further described by the same team in Kegerise *et al.* [104]. Murray [136] reports as well *mode-switching* for turbulent flows at low and medium subsonic Mach numbers in a cavity with $L/D = 6$. *Mode-switching* has also been found by 3D LES for $M = 0.8$ and $L/D = 3$ by Gloerfelt *et al.* [78], $M = 0.85$ and $L/D = 5$ by Larchevêque *et al.* [114] and $M = 0.8$ and $L/D = 2$ by Larchevêque *et al.* [113] in turbulent flows. For the author knowledge, *mode-switching* between dominant modes has not been reported for laminar flows.

3.1.3 Wake mode

The wake mode was first observed experimentally by Gharib and Roshko [71] in an axisymmetric cavity in a water wind tunnel, where the flow was incompressible and laminar. However, it has been rarely found in experiments and 3D simulations, hence this mode seems to be related to axisymmetric or two-dimensional configurations.

The wake mode has been described for laminar flows by 2D DNS simulations using incompressible equations [10, 11] and compressible equations at low and medium subsonic Mach numbers [22, 46, 116, 151]. All these studies concern shallow cavities of $L/D = 4$, which oscillate at a Strouhal number in the range of $0.061 \leq St_D \leq 0.064$, proving that the oscillation frequency does not depend on the Mach number and so it is not related to acoustic feedback.

Shieh and Morris [159] investigated a turbulent flow at $M = 0.6$ over a shallow cavity of $L/D = 4.4$ by 2D and 3D Detached Eddy Simulation (DES). They found that the two-dimensional simulation leads to wake mode with $St_D = 0.05$, while the corresponding three-dimensional cavity oscillates in a shear layer mode. Brès [21] found by DNS simulations that the three-dimensional counterpart of a cavity oscillating in wake mode in 2D presents a shear layer mode if spanwise disturbances are introduced, and a wake mode if the flow is initialized only with the time-averaged 2D results. The considered cavity was shallow with $L/D = 4$ and the flow was laminar and subsonic. A similar result was found by Suponitsky *et al.* [164] in their incompressible 3D LES simulations. They found a wake mode in a 3D cavity when the flow is two-dimensional, and a shear layer mode when the flow is forced to be three-dimensional by introducing random sinusoidal disturbances at the inflow, regardless of their amplitude and shape.

Colonius *et al.* [46] and Rowley *et al.* [151] found that for an $L/D = 4$ and $M = 0.3$, the flow switches from the shear layer mode to the wake mode, being both present at different times. The same configuration leads to a shear layer mode for $M = 0.2$ and to a wake mode for $M = 0.4$.

To feed the debate, low Mach number simulations over a cavity of $L/D = 4$, with similar Reynolds number and boundary layer thickness at the upstream edge of the cavity, have been found to present a shear layer mode [151] *or* a wake mode [116] in two different simulations. Both studies have been performed by Direct Numerical Simulation of the 2D compressible Navier-Stokes equations, using high-order schemes and non-reflecting boundary conditions. The main apparent difference between both simulations is the initial condition, which motivated the idea of studying the oscillation modes depending on the numerical initial condition, which is presented in sections §3.3 and §3.4.

3.1.4 Three-dimensional effects

Cavity flows have been described as highly three-dimensional both by experimental methods and 3D numerical simulations.

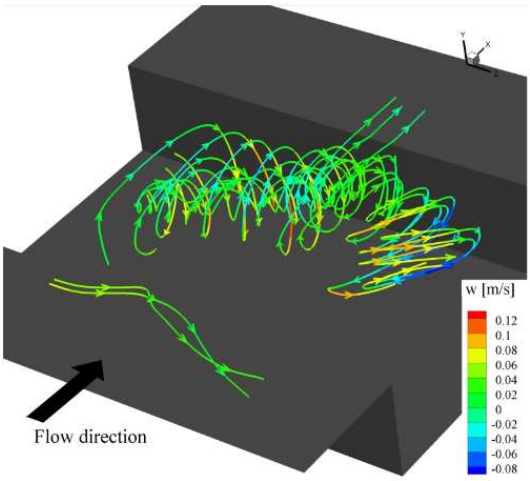

Figure 3.4 - *Three-dimensional effects in the form of a hairpin (Haigermoser et al.[86])*

Flow visualizations realized by Faure *et al.* [62] on deep cavities with $0.5 \leq L/D \leq 2$ and width-to-depth ratio $W/D = 6$ showed the development of spanwise structures for very low Mach number laminar flows. Similar results were obtained by Haigermoser *et al.* [86] and Haigermoser [85] who performed an experimental investigation using tomographic Particle Image Velocimetry (PIV) in laminar and turbulent low Mach number flows. For laminar cavity flows a distortion of the vortex tubes was observed near the downstream wall, whereas for the turbulent case three-dimensional structures in the form of a hairpin were distributed randomly inside the cavity as seen in figure 3.4. Three-dimensionality of a turbulent flow over a cavity of $L/D = 6$ was also studied experimentally by means of surface pressure measurements by Crook *et al.* [53], who found a spanwise variation of the pressure distribution.

Chang *et al.* [28] reports the three-dimensionality of incompressible laminar and turbulent flows over a cavity of $L/D = 2$ from their results from 3D LES. They describe how the spanwise vortices are disturbed in the spanwise direction as they approach the trailing edge, breaking into several hairpin-like vortices. Also from 3D LES results Larchevêque *et al.* [113] report a spanwise asymmetry of the mean flow in a cavity with $L/D = 2$ and $W/D = 4.8$ with an incoming turbulent flow at $M = 0.8$.

By means of 3D DNS using incompressible equations Yao *et al.* [182] investigated a laminar flow over several cavities ($L/D = 1, 2, 4$ and $W/D = 3$). Taylor-Görtler longitudinal vortices are found on the cavity bottom wall, and longitudinal vortex structures in the shear layer.

In order to explain these observations, Brès and Colonius [23] performed a linear stability analysis of a wide range of configurations ($L/D = 1, 2$ and $0.2 \leq M \leq 0.6$). Firstly 2D DNS simulations were performed and the steady cases were identified. The base steady flow was used for the 3D linear stability analysis to characterize the 3D mode.

The three-dimensional mode has a spanwise wavelength of about one cavity depth, and oscillates at a frequency lower than the Rossiter instabilities (about one order of magnitude lower). It does not depend on the Mach number, so it is an hydrodynamic mode and not an acoustic one like the 2D Rossiter instabilities. It is described as a generic centrifugal instability related to the recirculating flow near the downstream wall. 3D DNS simulations showed than when the centrifugal mode is present, the shear layer oscillations suffer a low frequency modulation [23].

3.1.5 Aeroacoustics of cavity f ows

The unsteady f ow over cavities produces high aerodynamic noise. Surface discontinuities are present in numerous industrial conf gurations, so the reduction of acoustic waves emissions becomes an important target. As a consequence, aeroacoustic studies involving cavity f ows are of interest.

The acoustics of a cavity can be investigated experimentally by means of several methods, for instance by the Schlieren technique (e.g. [65, 111, 184]), which is a f ow visualization method which displays the acoustic waves, or by recording the pressure signal (e.g. [32, 65]), method that allows a calculation of the Overall Sound Pressure Level (OSPL).

Two ways of analyzing aeroacoustics by numerical methods have been already described in section §1.1: by a computational aeroacoustics algorithm or by the use of an acoustic analogy. High-order-scheme methods have been used in DNS [23, 77, 151] and LES [79] for low and medium subsonic Mach number laminar f ows, and in LES [58, 78] and DES [159] for acoustic prediction of turbulent f ows.

Acoustic analogies have been used in DNS using the compressible equations [116] and incompressible equations [10, 11]. Both studies concern a shallow cavity of $L/D = 4$ at low Mach number (0.15), and it is concluded that the use of incompressible equations introduces differences in the results due to the rapid geometrical changes and strong structures of the f ow [11]. Acoustic analogies have been also used for higher subsonic f ows in DNS [77] and incompressible f ows in LES [164]. Recently, acoustic analogies have been applied to PIV data in order to extract the acoustic f eld of laminar [84] and turbulent [123] cavity f ows at very low Mach numbers.

As it has been described, the impingement of the shear layer into the trailing edge of the cavity produces pressure oscillations which escape the domain of the cavity and are perceived far-f eld as noise. In the early work of Krishnamurty [111] it was shown by the use of the Schlieren technique that the minimum L/D for which there is radiation of acoustic waves depends on the Mach number, proving that the minimum L/D decreases as Mach increases. A comparison of laminar and turbulent f ows showed that the radiated f eld is weaker for higher Reynolds numbers [111].

Krishnamurty observed that the acoustic waves propagate upstream for subsonic f ows as shown in f gure 3.5, and downstream for supersonic f ows [111]. This is in agreement with later deep cavity f ow investigations, which show a directivity of 130° respect to the downstream direction for a $M = 0.6$ laminar f ow [79], 135° at $M = 0.8$ [65], 150° at very low Mach number [84] or 145° at low and medium subsonic Mach numbers [46].

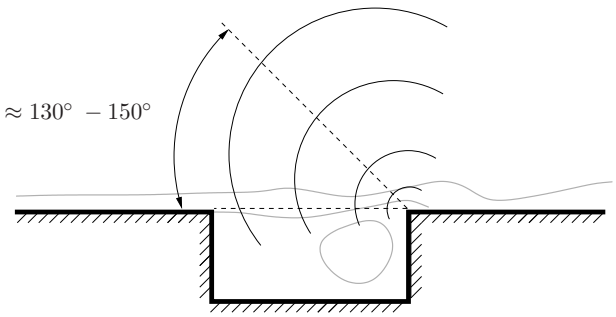

Figure 3.5 - *Directivity of the pressure waves emitted by a subsonic cavity flow oscillating in shear layer mode.*

On the other hand, shallow cavities are found to display a more uniform directivity for very low Mach numbers [84], and an intense upstream radiation for higher Mach numbers, but in which there is also a very sharp acoustic pulse emitted at the trailing edge [46]. Ahuja and Mendoza [2] also observed that shallower cavities produce a more uniform sound emission.

The numerical results obtained for a supersonic flow at $M = 1.5$ by Rona and Brooksbank [148] and Zhang *et al.* [184] display a directivity downstream, as observed by Krishnamurty [111].

The Overall Sound Pressure Levels are in general much higher than 100dB. For example, for a cavity of $L/D = 1$ and $M = 0.6$ the OSPL is found to be around 140-150dB at a distance of $3D$ from the cavity trailing edge, depending on the cavity width and the boundary layer thickness [79]. According to the results of Gloerfelt *et al.* [79], wide cavities are louder than narrow cavities, and they reason that it might be due to the higher spanwise coherence, which reinforces the feedback strength. The OSPL increase with the Mach number, finding for a cavity with $L/D = 2$ approximate values of 149dB for $M = 0.6$, 153dB for $M = 0.9$ and 154 for $M = 1.1$ over the cavity opening at $0.2L$ upstream from the trailing edge [87].

In the results by Shieh and Morris [158], where the 2D simulation leads to a wake mode and the 3D simulation to a shear layer mode, the acoustic levels between both flow regimes can be compared. At a distance of $3D$ from the cavity corner in the direction in which the pressure waves are propagated (135°), the shear layer presents 132dB whereas the wake mode produces 135dB. Also Brès and Colonius [23] observed higher OSPL values for 2D simulations, even though both 2D and 3D cavities were oscillating in shear layer mode.

3.2 Validation test case

The numerical method has been validated by reproducing a test case investigated by several authors [21, 76, 151, 152], consisting in a deep cavity of length-to-depth ratio $L/D = 2$ with an incoming boundary layer. The flow is compressible with a Mach number $M = 0.6$, and its regime is laminar with a Reynolds number based on the cavity depth of $Re_D \approx 1500$. More flow parameters are detailed in table 3.1, where δ is the boundary layer thickness and θ is the momentum thickness at the upstream cavity edge.

3.2.1 Configuration

The computational domain, shown in figure 3.6, consists of a non-equidistant mesh refined near the walls and around the shear layer spanning over the cavity. The length scales x and y are normalized by the cavity depth D. The number of grid points inside the cavity is 167×144, and over the cavity is 512×648,

L/D	M	δ/D	L/θ	Re_D	Re_θ	D[m]	U_∞[m/s]
2	0.6	0.28	52.8	1491	56.4	0.000111	207.6

Table 3.1 - *Flow parameters for the validation test case.*

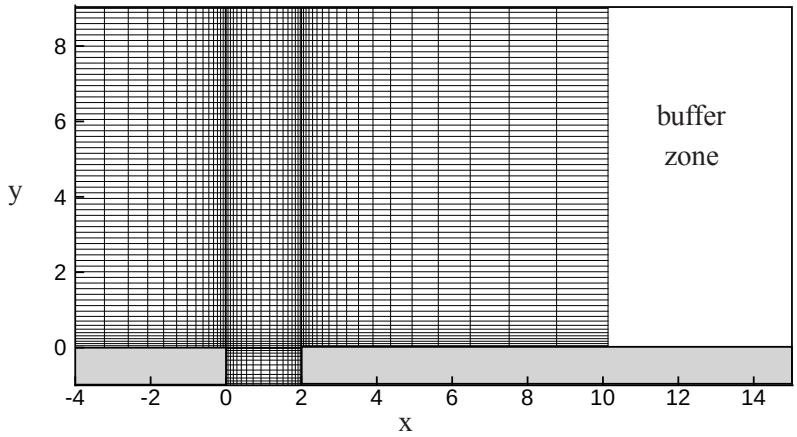

Figure 3.6 - *Computational domain and grid. For clarity, only 1 every 10 points is displayed.* $L/D = 2$.

from which 25×648 grid points belong to the buffer zone.

The y^+ at one cavity length unit upstream from the cavity is 0.3. Two other grids have been used in order to verify grid convergence, a f ner one with $y^+ = 0.2$ and a coarser one where $y^+ = 0.7$. The spectrum of the pressure f uctuations at the location $(x, y) = (D, 7D)$ is displayed in f gure 3.7 and used for comparison. The reference case $y^+ = 0.3$ is represented by the blue solid line, the grid with $y^+ = 0.2$ by a black dashed line and the grid with $y^+ = 0.7$ by a red dash dot line. All three grids provide very similar frequency and amplitude, proving that the results are indeed grid independent.

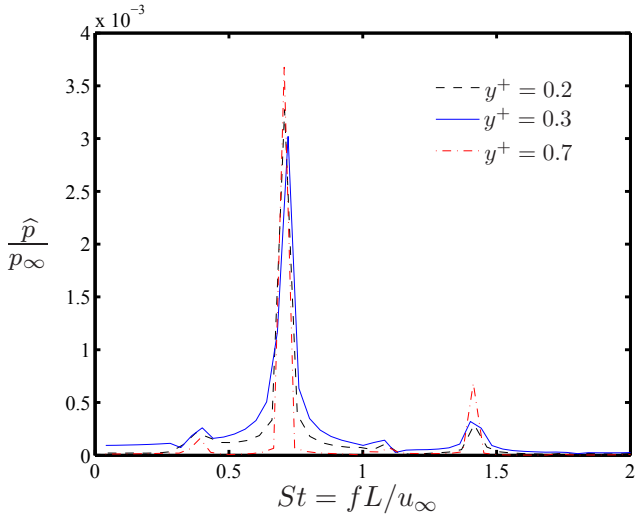

Figure 3.7 - *Spectrum of pressure fluctuations for several grids.* $L/D = 2$, $M = 0.6$.

The solid boundary conditions have been implemented with ghost cells, where the 4^{th} order scheme has been used to calculate the pressure gradient. The walls are considered isothermal and non-slip. The inf ow condition is a laminar boundary layer def ned as the numerical solution of the Blasius similarity equation. The characteristic boundary conditions of Giles are used at both the inf ow and radiation boundaries.

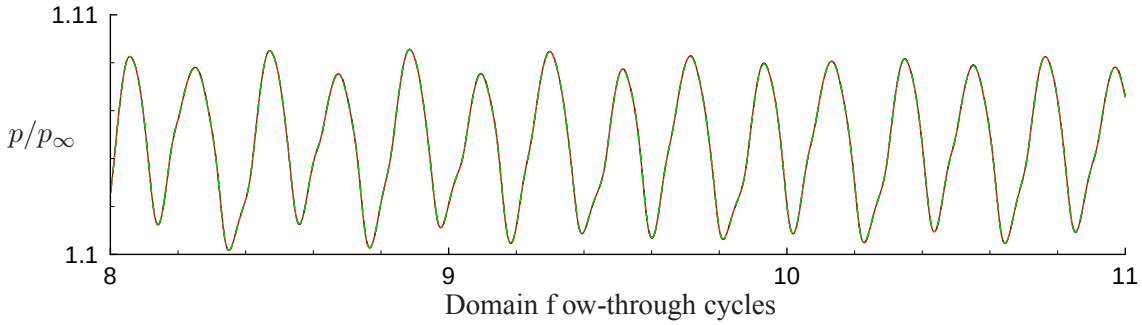

Figure 3.8 - *Pressure time history. L/D=2, M=0.6. Black dashed line:* $\sigma = 0.25$*, red solid line:* $\sigma = 1.00$*, green dash dot:* $\sigma = 3.00$*.*

At the outf ow, the characteristics of Poinsot and Lele [140] are used, where different values of the relaxation coeff cient from equation (1.27) are compared: $\sigma = 0.25$, $\sigma = 1.00$ and $\sigma = 3.00$. The pressure time history for the three simulations at the location $(D, 7D)$ is shown in f gure 3.8. All simulations give identical results, being the three lines perfectly overlapped, and proving the relaxation coeff cient independence.

3.2.2 Results

This conf guration oscillates in a shear layer mode. The incoming boundary layer separates at the leading edge forming an oscillating shear layer, where the small disturbances are amplif ed by the Kelvin-Helmholtz instability. Its interaction with the trailing edge produces feedback of pressure waves, which disturb the shear layer at the upstream wall. A part of these acoustic waves escapes the domain of the cavity and are perceived far-f eld as noise. Inside the cavity, a recirculation region is generated next to the downstream wall, of about the same scale as the cavity depth.

Figure 3.9 shows the instantaneous isocontours of vorticity at two different times of the oscillation period $\mathcal{T}$, displaying the incoming boundary layer and the recirculating region near the downstream wall.

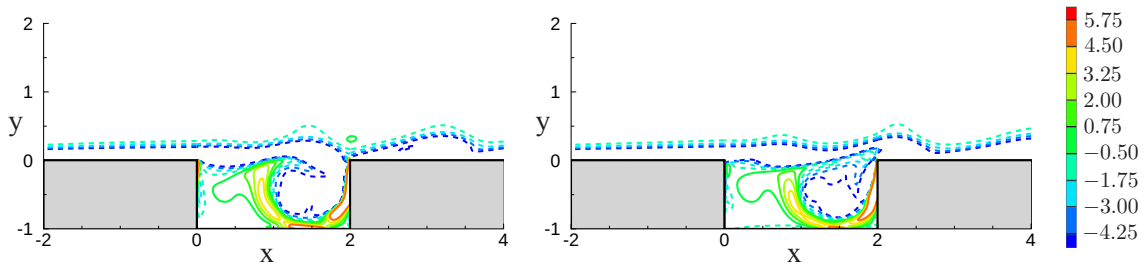

(a) t = 0 (b) t = 0.5 $\mathcal{T}$

Figure 3.9 - *Instantaneous vorticity isocontours* $\omega D/u_\infty$*, dashed negative values.* $L/D = 2$*,* $M = 0.6$*. Blasius initial condition, dominant mode* St_2*.*

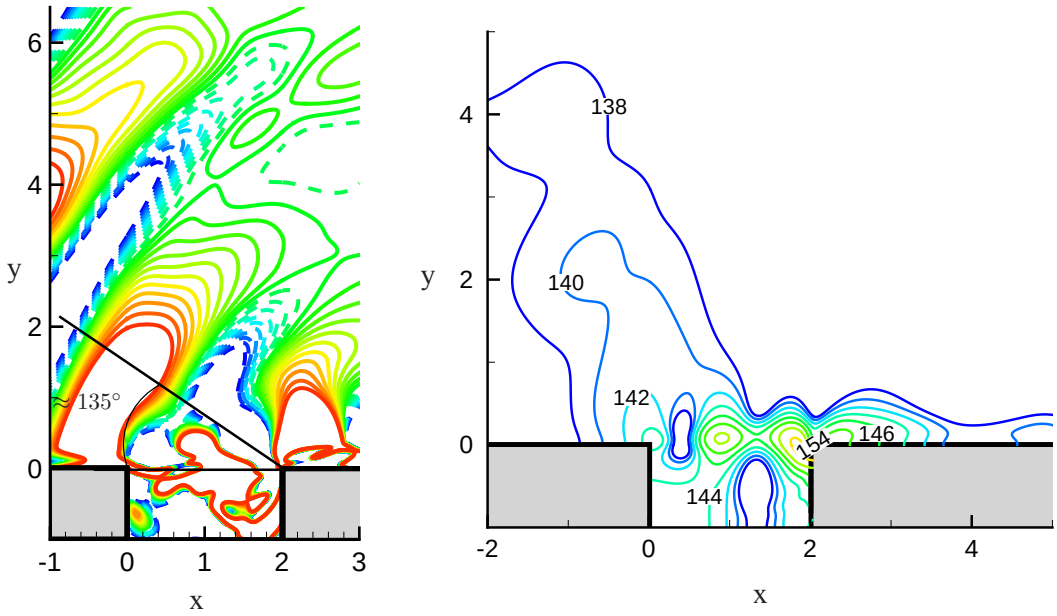

(a) Instantaneous dilatation.

(b) OSPL.

Figure 3.10 - *Directivity of the acoustic waves. (a) Instantaneous dilatation, 21 equidistant isocontours from* $\Theta D/u_\infty$ *= -0.1 to 0.1, dashed negative values. (b) Overall Sound Pressure Levels from 138 to 154. L/D=2, M=0.6. Blasius initial condition, dominant mode* St_2

The acoustic waves can be observed from the dilatation f eld:

$$\Theta = \frac{\partial u}{\partial x} + \frac{\partial v}{\partial y} = -\frac{1}{\rho}\frac{\partial \rho}{\partial t} \tag{3.2}$$

Figure 3.10(a) represents the dilatation isocontours which shows that the acoustic propagation occurs at an angle of approximately 135° with respect to the downstream direction. These results are in good agreement with the studies of Rowley *et al.* [152, 151].

Both vorticity and dilatation f elds have been computed using several schemes for the derivatives of velocity. 2^{nd}, 4^{th}, 6^{th} order explicit and 6^{th} order compact schemes have been compared and gave the same results.

The directivity of the acoustic waves can also be observed in f gure 3.10(b), where the Overall Sound Pressure Levels (OSPL) are represented:

$$OSPL = 20\log_{10}\left(\frac{P_{rms}}{P_{ref}}\right) \tag{3.3}$$

where P_{rms} is the root mean square pressure and P_{ref} is the reference sound pressure value, commonly $2 \cdot 10^{-5}$Pa for air. It is observed that a maximum OSPL of 154dB is found near the trailing edge of the

cavity. This value is in agreement with the results obtained by Brès [21], whose numerical predictions estimate a maximum of 162dB by 2D simulations and 160dB by 3D simulations.

Pressure fluctuations at the location $(D, 7D)$ are used to perform a Fast Fourier Transform in order to obtain the frequency of oscillation. It is found that the flow oscillates at a Strouhal number $St_2 = f_2 L/u_\infty = 0.75$, corresponding to the second Rossiter mode. The first peak in the spectra shown in figure 3.11 is $St_1 = f_1 L/u_\infty = 0.39$ corresponding to the first Rossiter mode. These values are in good agreement with the values $St_1 = 0.39$ and $St_2 = 0.72$ predicted by Gloerfelt [76], as well as by the Rossiter formula [150] from equation (3.1), which predicts $St_1 = 0.32$ and $St_2 = 0.74$ for a Mach number 0.6.

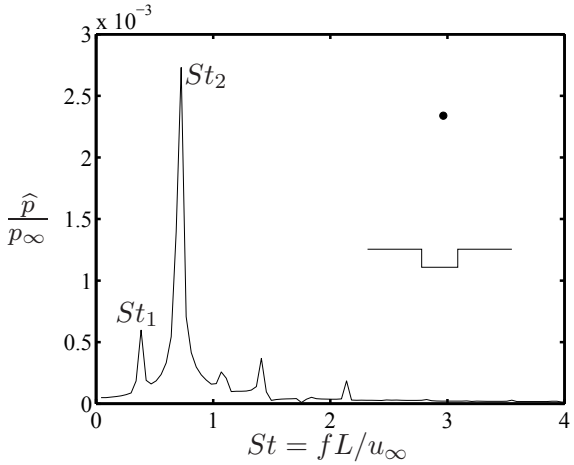

Figure 3.11 - *Spectrum of pressure fluctuations.* $L/D = 2$, $M = 0.6$. *Blasius initial condition.*

3.3 Deep cavities

Laminar flows over deep cavities with a length-to-depth ratio of 2 are found to oscillate in a shear layer regime. The oscillation modes have been widely described as the first and second Rossiter modes, yet there is still disagreement about which is the dominant one. The knowledge of the dominant mode is fundamental for the analysis of sound generation and for the application of flow and noise control.

In general, numerical investigations in 2D report that the dominant mode is the first Rossiter mode for Mach numbers up to 0.6, while the second mode is found to be dominant for Mach numbers higher than 0.6, as detailed in table 3.6 in the appendix of this chapter. Nevertheless, Gloerfelt [76] finds in a 2D DNS simulation at Mach 0.6 that the second mode is dominant, increasing the confusion.

To further investigate this phenomena at a Mach number 0.6, the same configuration as in the validation section is taken, whose main parameters are shown in table 3.1 and whose main features have been described. Especially, the influence of the initial condition is to be studied, as well as the temporal evolution of the dominant mode.

3.3.1 Evolution of the oscillation modes

The initial condition considered here as the base case is the numerical solution of the Blasius similarity equation shown in the validation section §3.2. Three probes were located in the computational domain as displayed in f gure 3.12. P1 is placed above the cavity at $(x, y) = (D, 7D)$, P2 inside the oscillating shear layer at $(D, 0)$ and P3 at the bottom wall of the cavity at $(1.5D, -D)$. The time history of pressure and vorticity f uctuations were taken at these three locations, and the wall shear stress was recorded by P3 (situated at the bottom wall).

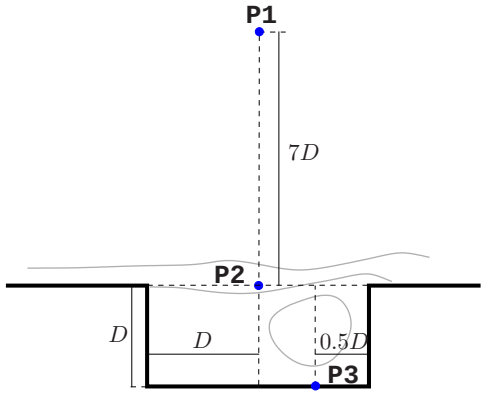

Figure 3.12 - *Probes to record time-history.* $L/D = 2$

The computation was run during 18 domain f ow-through cycles, in which three windows were used in order to perform the Fast Fourier Transform, corresponding to the cycles 6 to 9, 9 to 12, and 14.5 to 18. It was found that the pressure, vorticity and wall shear stress spectra change with time, as illustrated by the pressure spectra in f gure 3.13.

At the initial stages of the simulation, between the cycles 6 and 9, two oscillation frequencies are found, St_2 (dominant) and St_1, as shown in f gure 3.13. While the second Rossiter mode keeps a

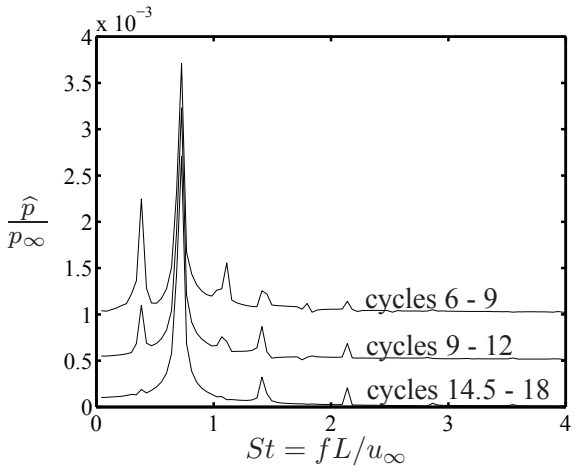

Figure 3.13 - *Spectrum of pressure fluctuations at* P1 *using 3 different windows. Translation of 0.5 of the y-axis for clarity.* $L/D = 2$, $M = 0.6$. *Blasius initial condition.*

constant amplitude in time, the first mode decreases in amplitude until its disappearance, and only the second mode remains after 12 cycles, as shown in figure 3.13. A similar phenomena was observed by Brès and Colonius [23], but in their two-dimensional DNS simulations only the first Rossiter mode remained.

In brief, the dominant oscillation mode changes with time. However, it does not seem that there is a periodically *mode-switching* as it has been described in several turbulent flow investigations [78, 104], since only the second mode remains and the others are not recovered. Then, the sensitivity of the dominant oscillating mode to the initial condition is to be investigated.

3.3.2 Effect of the initial condition

Several simulations have been computed with different initial conditions of velocity. It is important to mention that all the other physical parameters (Reynolds number, Mach number, boundary layer at the inflow) and numerical conditions (grid, boundary conditions) remain constant. In all the cases pressure is initialized as $p = p_\infty = 1.01325 \cdot 10^5 Pa$ and temperature as $T = T_\infty = 298K$ throughout the domain, including the interior of the cavity. Density is calculated from the equation of state for ideal gases $\rho_\infty = p_\infty / rT_\infty$. Inside the cavity the velocity is initialized as zero.

The following initial conditions of velocity over the cavity have been tested:

BLAS Both velocities are defined from the numerical solution of the Blasius similarity equation, with boundary layer thickness δ increasing downstream.

CONS Both velocities are defined from the numerical solution of the Blasius similarity equation, with boundary layer thickness constant from the inflow, $\delta = \delta_{inflow}$.

POLY The normal velocity is initialized as $v = 0$, and streamwise velocity is calculated from a polynomial approximation of a laminar boundary layer [75]:

$$u(y) = u_\infty \left(\frac{y}{\delta}\right) \left[2 - 2\left(\frac{y}{\delta}\right)^2 + \left(\frac{y}{\delta}\right)^3\right] \tag{3.4}$$

where u_∞ is the freestream velocity and δ is the boundary layer thickness at each streamwise position.

UINF The streamwise velocity is initialized as $u = u_\infty$, and normal velocity as $v = 0$.

ZERO Both velocities are initialized as $u = v = 0$, like the interior of the cavity.

For all the cases the inflow condition is kept constant, being the numerical solution of the Blasius similarity equation which gives $\delta/D = 0.28$ at the upstream edge of the cavity. The three first initial conditions consist on boundary layers of different boundary layer thickness δ_0 at the upstream edge of the cavity, being $\delta_0/D = 0.28$ for BLAS, $\delta_0/D = 0.12$ for CONS and $\delta_0/D = 0.23$ for POLY. Furthermore, the initial condition POLY has a shape factor different from the Blasius value $H = 2.59$ of the other two cases. The last two test cases, UINF and ZERO, do not have an initial boundary layer thickness or shape factor.

	BLAS	POLY	CONS	UINF	ZERO	Rossiter
St_1	0.39	0.41	0.41	0.39	0.41	0.32
St_2	0.75	0.73	0.73	0.75	0.75	0.74

Table 3.2 - *Oscillation modes obtained for different initial conditions compared to the Rossiter predictions.*

The simulations performed with the initial conditions POLY, CONS and UINF present a behavior similar to the test case BLAS. That is to say, there are two modes of oscillation during the first cycles, being the second one dominant, and after some cycles the first mode decreases in amplitude and only the second mode remains. However, it is observed that the amplitude of the first mode is smaller in these three cases than in the simulation using BLAS, and it decreases faster and it disappears earlier in the computation, approximately after 10 domain flow-through cycles.

On the other hand, the computation using the initial condition ZERO presents a different evolution. Initially, during the cycles 6 to 9 the flow oscillates with the first mode dominant and the second is of smaller amplitude. As before, the first mode decreases in amplitude, becoming smaller than the second mode after several cycles and finally vanishing after 18 cycles (this simulation has been run for 21.5 cycles).

Table 3.2 shows the Strouhal numbers obtained from the different initial conditions and the values predicted by the Rossiter formula. All initial conditions give similar results, being in agreement with the predictions obtained from the Rossiter formula, especially for the second mode. BLAS and UINF give a slightly better agreement for the first mode than the other cases.

Figure 3.14 shows the instantaneous vorticity isocontours of the simulation ZERO while it is oscillating at the first Rossiter mode. It presents the same contour level values than the flow oscillating at the second Rossiter mode, obtained with the initial condition BLAS and shown in figure 3.9, but there is a slight difference between both figures. It is known that the waves spanning over the cavity are related to the oscillation mode. In figure 3.9 two waves can be seen along the shear layer, while figure 3.14 shows a longer wave alone. This results suggest that the spectrum obtained for the ZERO case is not due to a numerical transient time of the simulation, but the physics of a cavity flow oscillating at the first Rossiter mode are represented.

Figure 3.15 shows the dilatation isocontours of the simulation ZERO while it is oscillating at the first Rossiter mode. It presents lower contour values than those from a cavity oscillating at the second

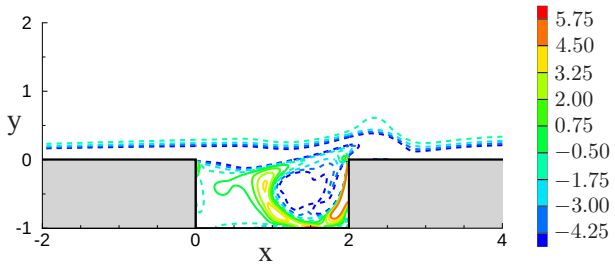

Figure 3.14 - *Instantaneous vorticity isocontours $\omega D/u_\infty$, dashed negative values. $L/D = 2$, $M = 0.6$. ZERO initial condition, dominant mode St_1.*

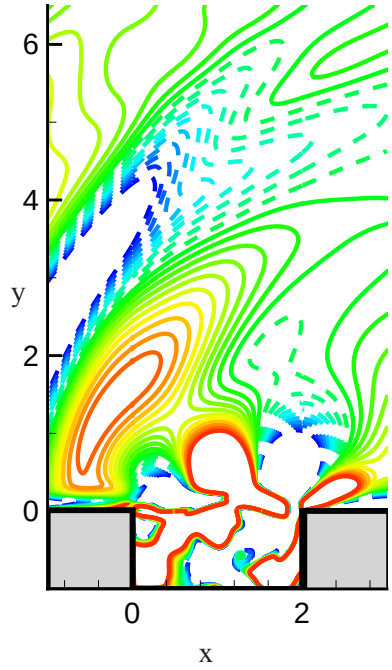

Figure 3.15 - *Instantaneous dilatation, 21 equidistant isocontours from* $\Theta D/u_\infty$ *= -0.1 to 0.1, dashed negative values. L/D=2, M=0.6. ZERO initial condition, dominant mode* St_1.

Rossiter mode, as shown in figure 3.10(a). Colonius *et al.* [45] show in their investigation that the acoustic radiation in shear layer regime is dominated by the second Rossiter mode, which could explain why the dilatation levels when the first mode is dominant are lower than when the dominant mode is the second. On the other hand, the directivity of the acoustic waves is the same.

As a conclusion, all initial conditions lead to the same final result, i.e. a flow oscillating at the second Rossiter mode. Most of the initial conditions present the same evolution, yet BLAS keeps the first mode for longer time before damping. The initial condition ZERO converges to the same solution, even though at the beginning the flow presents different physics, oscillating at the first Rossiter mode. Since the transient time is much longer, this simulation is computationally more expensive.

This cavity flow configuration has been previously investigated, giving different results regarding the dominant mode. Rowley *et al.* [151], Brès and Colonius [23] and Hamed *et al.* [87] find in their 2D numerical simulations the first Rossiter mode to be dominant. On the other hand, Krishnamurty [111] found the second Rossiter mode in his experiments, as well as Brès and Colonius [23] in their 3D DNS simulations and Gloerfelt [76] in his 2D numerical investigation.

The linear stability analysis by Brès and Colonius [23] shows that a cavity with an $L/D = 2$ and $L/\theta = 52.8$, with $Re_D = 1500$ and $M = 0.6$ is unstable. This result and the present investigation suggest that a flow over this specific cavity configuration can oscillate at the first or second Rossiter modes, depending on the numerical initial conditions.

Regarding other deep cavity studies (e.g. list in table 3.7), experimental results and three-dimensional

numerical simulations of laminar flows show, in general, that the dominant mode is St_2 for length-to-depth ratios higher than 0.8, and St_1 for $L/D < 0.8$. On the other hand, turbulent flows seem to be much less predictable, since different authors find the dominant mode to change with the L/D ratio and/or Mach number, with similar inflow conditions.

3.3.3 Overall Sound Pressure Levels

The Overall Sound Pressure Level has been computed for all the cases using 20 samples over 1 period at the end of the computation, where the second Rossiter mode is dominant. All initial conditions provide the same contours as BLAS, shown in figure 3.10(b). A maximum OSPL level of 154dB is found at the trailing edge of the cavity. Both the distribution and the maximum OSPL are in good agreement with the results obtained by Brès [21] in his 3D simulations, for which a maximum of 160dB is estimated.

Since the oscillation modes change in time, the OSPL has been computed at different stages of the computation for the cases BLAS and ZERO. The early stages of the simulation BLAS show the same maximum levels and directivity than at the end of the computation, so the OSPL levels do not change while the second Rossiter mode is dominant, either if the first mode is present or not.

On the other hand, the distribution of the early stages of ZERO is a bit different, more similar to the 2D results of Brès[21], where there is a broadening of the isocontours, as shown in figure 3.16. At the beginning of the ZERO computation the first mode is dominant, as it is in the 2D simulation of Brès[21]. These results suggest that the differences observed between several studies do not depend on the two- or three-dimensionality of the investigation, but on the dominant oscillation mode.

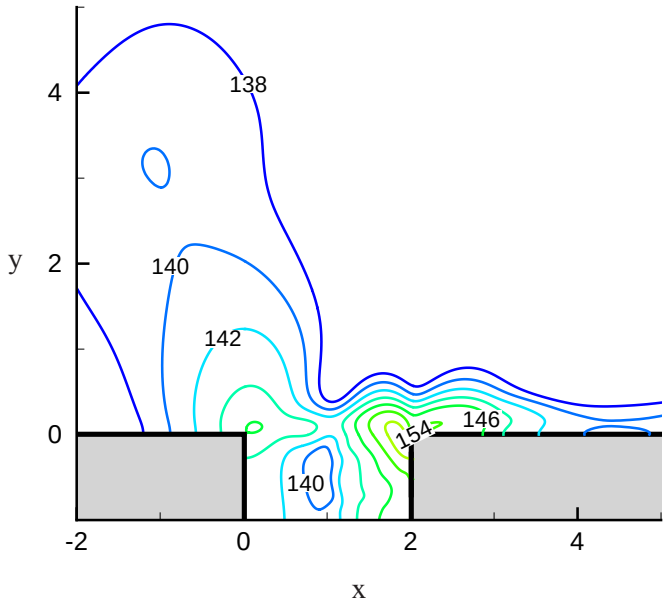

Figure 3.16 - *Overall Sound Pressure Levels from 138 to 154. $L/D = 2$, $M = 0.6$. ZERO initial condition, dominant mode St_1.*

There are other available results in the literature for the OSPL values of this conf guration which are worth mentioning here. By the use of 2D DNS simulations, Rowley *et al.*[151] found a maximum of 180dB at the cavity edge, and Hamed *et al.* [87] estimated 149dB at the cavity opening. Regarding experimental studies, for a similar conf guration but with a Reynolds number about 5 times higher, Krishnamurty [111] estimates 163dB based on def ections from f nite-fringe interferometry.

3.3.4 Effect of Mach number and boundary layer thickness

The results obtained from the 2D numerical simulations show that a $M = 0.6$ laminar f ow over a cavity of $L/D = 2$ oscillates at the frequency corresponding to the second Rossiter mode, but that in the f rst stages of the simulation the f rst Rossiter mode is also found. It has been mentioned as well that there is no agreement in the literature concerning the dominant mode in this particular test case. In general, as shown in table 3.6, cavity f ows at Mach numbers higher than 0.6 oscillate at St_2 whereas smaller Mach number f ows oscillate at St_1.

According to the linear stability analysis of Brès and Colonius [23], higher Rossiter modes are found for higher M and larger L/θ. From f gure 2 in [23] (reproduced here in f gure 3.1) is also observed that this case is far from the stability zone. Consequently, it is thought that by approaching the stability zone (i.e. by reducing the Mach or the Reynolds number) the f ow will oscillate at the f rst Rossiter mode. For this reason another test case with $M = 0.4$, whose main parameters are detailed in table 3.3 has been performed. It is expected as well to f nd the f rst Rossiter mode in cavity f ows with a higher boundary layer thickness (i.e. smaller L/θ), since they are more stable. Two test cases, described in table 3.3, have been computed to observe the oscillation response.

Mach	δ/D	L/θ	Re_D	Re_θ	dominant mode
0.6	0.28	52.8	1491	56.4	St_2
0.4	0.28	52.8	1489	56.4	St_2
0.6	0.45	33.3	941	56.4	St_1
0.6	0.37	41.0	1155	56.4	St_1

Table 3.3 - *Flow parameters and results of the different test cases of cavity L/D=2.*

These new test cases have been computed with the same computational domain, grid and boundary conditions as the reference case.

To implement the test case with $M = 0.4$ the boundary layer thickness has been maintained, so $L/\theta = 52.8$ as for the reference case. The simulation has been initialized with the condition `UINF`. The time history of pressure f uctuations has been recorded at the location `P1` (above the cavity), and the three windows have been used to perform the FFT as before. The results are very similar to those from the reference case, in which between the cycles 6 and 9 both Rossiter modes are found, the f rst one reduces its amplitude in cycles 9 to 12, and f nally only the second Rossiter mode is found between the cycles 15 and 18. The value of the Strouhal number is $St_2 = 0.77$, in good agreement with the value $St_2 = 0.81$ predicted by the Rossiter formula.

For the next simulation, the Mach number is kept at $M = 0.6$ and the boundary layer thickness is increased so $L/\theta = 41.0$, being closer to the stability zone. The simulation has been initialized with

the condition UINF. The frequency of oscillation has been calculated as before, from the time history of pressure fluctuations over the cavity. Three windows corresponding to the cycles 6 to 9, 9 to 12 and 15 to 18 have been used, but in this case no differences are observed. All the FFT show only one frequency of oscillation, corresponding to the first Rossiter mode with $St_1 = 0.41$.

The boundary layer thickness has been increased even more in the last test case, where $L/\theta = 33.3$ and $M = 0.6$. This case is in the limit of the stability zone, and two initial conditions have been used: UINF and ZERO. Both initial conditions give the same results. The time history of pressure fluctuations at P1 is displayed in figure 3.17, where it is observed that the amplitude of the oscillations decays in time. The FFT of the pressure signal shows that the flow oscillates at the first Rossiter mode and $St_1 = 0.40$. Brès and Colonius [23] also found the first Rossiter mode for a case where the amplitude decreased in time until reaching a steady state. In their simulation, the parameters were $L/\theta = 53$ and $M = 0.325$.

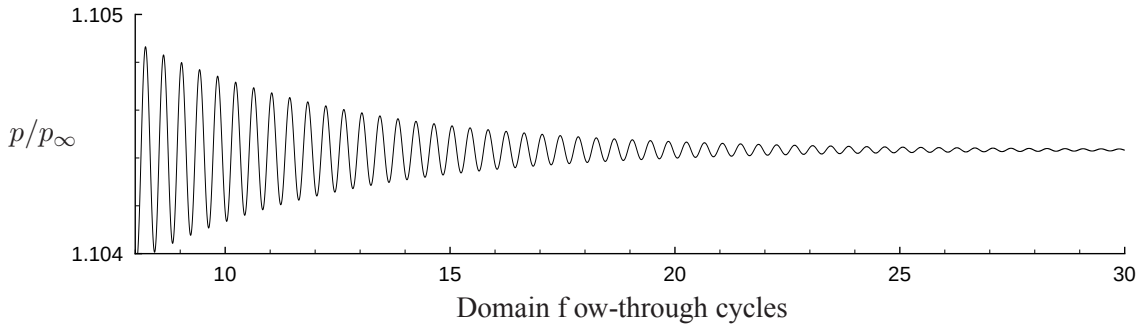

Figure 3.17 - *Pressure time history at* P1. $L/D = 2$, $M = 0.6$, $L/\theta = 33.3$.

These results prove that for larger boundary layer thickness, which correspond to more stable flows, the main frequency of oscillation is the first Rossiter mode. A change of Mach number, from 0.6 to 0.4 has not shown any significant difference.

3.4 Shallow cavities

The flow regime in shallow cavities of $L/D = 4$ is more complex to predict, since it can either present a shear layer mode or a wake mode, or even non oscillating mode depending on the geometry and inflow conditions. Previous investigations show that shallow cavities, in general, oscillate in a shear layer mode for low Mach numbers or large momentum thickness, while they oscillate in a wake mode for high velocities or thin boundary layers.

However, the limit is not clear. Rowley *et al.* [151] predicts shear layer mode for Mach numbers smaller than 0.3 when $L/\theta = 102$, while Larsson *et al.* [116] found a wake mode for the same flow and geometry conditions at a Mach number 0.15. Both studies have been performed by Direct Numerical Simulation of the 2D full compressible Navier-Stokes equations, using high-order schemes and non-reflecting boundary conditions. The main apparent difference between both simulations is the initial condition. Rowley *et al.* initialized the velocity field as a laminar Blasius boundary layer over the cavity, and zero inside [151], while Larsson *et al.* initialized the whole field as zero (private communication with the author).

L/D	Mach	δ/D	L/θ	Re_D	Re_θ	D[m]	U_∞[m/s]
4	0.15	0.31	96.8	1511	62.5	0.00045	51.9

Table 3.4 - *Flow parameters of the shallow cavity test case.*

3.4.1 Conf guration

For this study, the case proposed by Larsson *et al.* [116] is selected, consisting on a shallow cavity of $L/D = 4$, $M = 0.15$ and $L/\theta = 96.8$. Other f ow parameters can be seen in table 3.4.

The computational domain, shown in f gure 3.18, consists on a non-equidistant mesh ref ned near the walls and around the shear layer spanning over the cavity. The length scales x and y are normalized by D. The number of grid points inside the cavity is 311×106, and over the cavity is 1061×648. The y^+ at one cavity length unit upstream from the cavity is 0.3.

This cavity conf guration oscillates in wake mode, in which large eddies are convected downstream. In order to damp them before they reach the non-ref ecting downstream boundary, a large buffer zone is required. As displayed in f gure 3.18, this buffer zone is longer than the one for the deep cavity conf guration shown in f gure 3.6. In this case, the buffer zone is composed of 75×648 grid points.

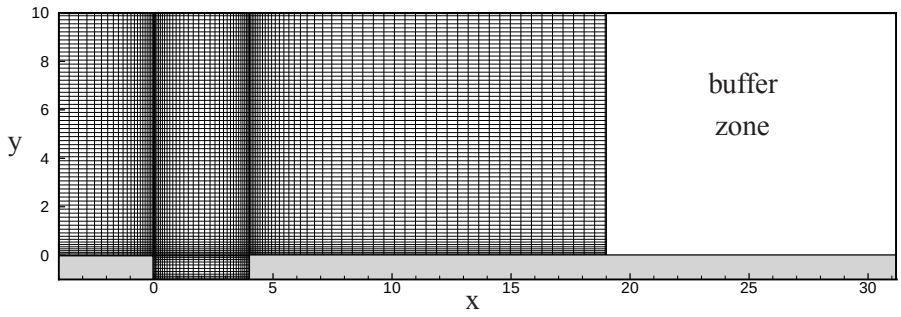

Figure 3.18 - *Computational domain and grid. For clarity, only 1 every 10 points is displayed.* $L/D = 4$.

The characteristic boundary conditions of Giles are used at the inf ow and radiation boundaries. The inf ow condition is a laminar boundary layer def ned as the numerical solution of the Blasius similarity equation. At the outf ow, the characteristics of Poinsot and Lele [140] are used, where the relaxation coeff cient is taken as $\sigma = 1.00$. The walls are considered isothermal and non-slip and are implemented with ghost cells with a 4^{th} order scheme.

3.4.2 Effect of the initial condition

Three initial conditions are selected in this case: `BLAS`, `UINF` and `ZERO`, who have been described previously in §3.3.2, and three probes are used in order to record the time history of pressure, vorticity and wall friction, as displayed in f gure 3.19.

Figure 3.20 shows the time-history of wall friction at `P3` $(2D, -D)$ for the three test cases. It is clearly displayed that the `ZERO` initial condition develops a f ow with a much higher wall friction and

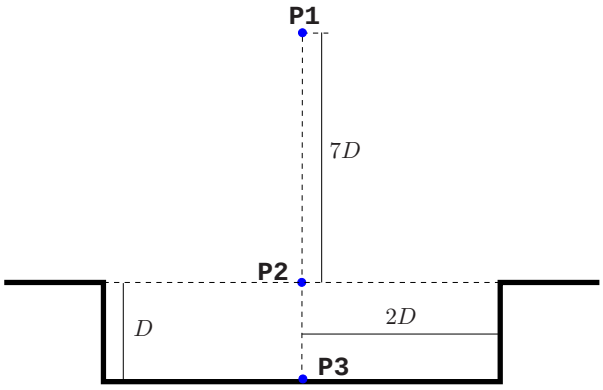

Figure 3.19 - *Probes to record time-history.* $L/D = 4$

hence higher drag. This is the main feature of the wake mode. On the other hand, BLAS and UINF present a much lower wall friction, both about the same order of magnitude and one order of magnitude smaller than ZERO. These two initial conditions lead to a shear layer mode. Contrarily to the deep cavity test case, different initial conditions can lead to a different f ow regime for this particular shallow cavity.

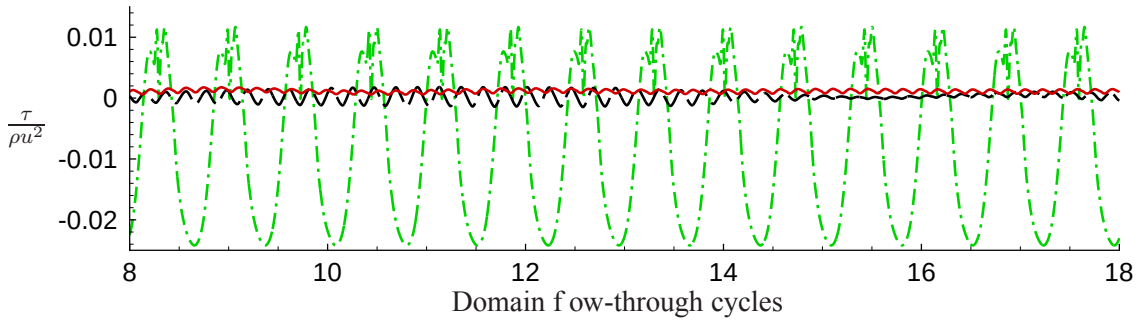

Figure 3.20 - *Wall friction time history at* P3. $L/D = 4$, $M = 0.15$. *Green dash dot:* ZERO, *red solid line:* UINF, *black dashed:* BLAS.

The cavity f ow in a wake mode is totally periodic and it presents only one oscillation mode, as shown in f gure 3.21. This spectrum has been calculated from the time-history of vorticity f uctuations at the position P2 $(2D, 0)$. The Strouhal number is $St_D = fD/u_\infty = 0.061$, in very good agreement with the value $St_D = 0.061$ found by Larsson *et al.* [116] for the same cavity conf guration and $St_D = 0.067$ from Suponitsky *et al.* [164] for an incompressible f ow over an $L/D = 4$ cavity oscillating in wake mode. For similar cavities in wake mode but higher Mach numbers, Rowley *et al.* [151] found values in the range $St_D = 0.061$ to $St_D = 0.064$, and Shieh and Morris [158] report $St_D = 0.054$ for a cavity of $L/D = 4.4$ and $M = 0.6$.

In wake mode, the f ow spanning over the cavity reattaches at the bottom wall, creating a large vortex starting from the leading edge. In a similar manner to the f ow behind a backward-facing-step shown in §2.3.2, the vortex grows and a secondary vortex appears at the upstream corner. The primary vortex separates from the incoming boundary layer and it is ejected over the downstream corner. Then the secondary vortex is large enough and it reattaches the upstream boundary layer. Figure 3.22 shows the isocontours of vorticity at four different instants in time during one period of oscillation $\mathcal{T}$.

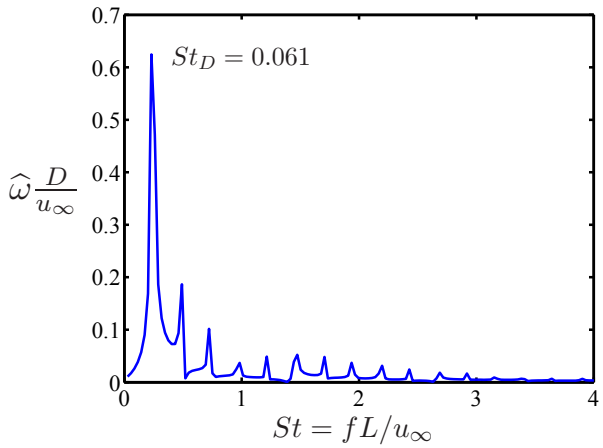

Figure 3.21 - *Spectrum of vorticity fluctuations at P2.* $L/D = 4$, $M = 0.15$. *Initial condition ZERO, wake mode.*

The ejection of the vortex over the trailing edge produces a low pressure zone at the cavity downstream wall, which corresponds to the lowest value of drag. On the other hand, the highest value of drag is found when the vortex has left the cavity only partially, and the downstream wall is exposed to the external f ow which is going inside the cavity.

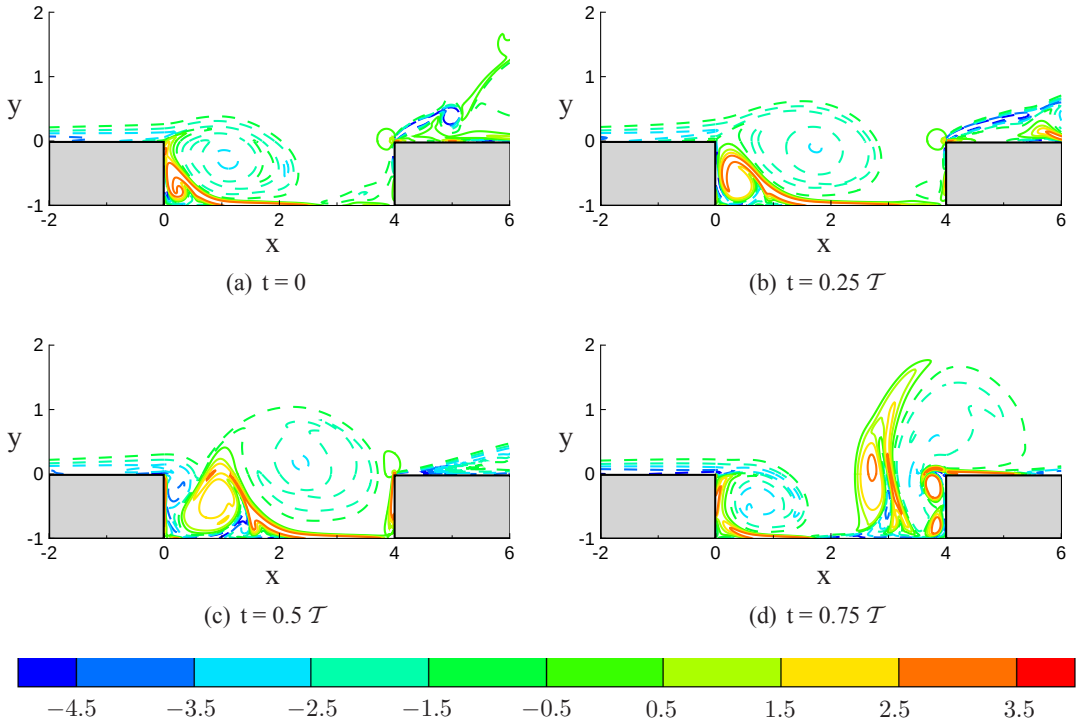

Figure 3.22 - *Instantaneous vorticity isocontours* $\omega D/u_\infty$, *dashed negative values.* $L/D = 4$, $M = 0.15$. *Initial condition ZERO, wake mode.*

The cavity flow initialized with the condition UINF, which oscillates in shear layer mode, is also perfectly periodic, as shown in figure 3.20. From the time-history of vorticity fluctuations the frequency of oscillation is found to be $St_2 = 1.00$, as illustrated in figure 3.23. It corresponds to the second Rossiter mode, predicted to be $St_2 = 0.92$ by the Rossiter formula in equation (3.1).

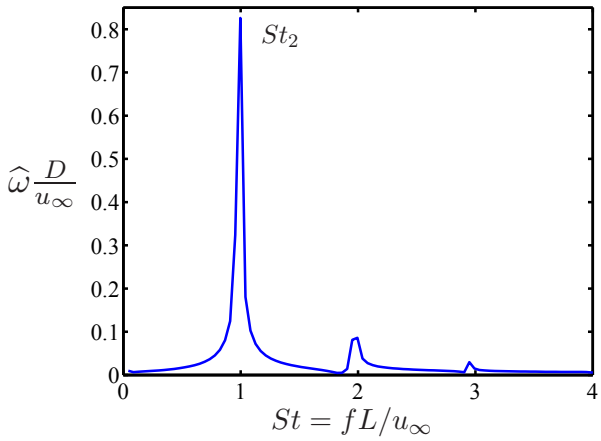

Figure 3.23 - *Spectrum of vorticity fluctuations at* P2. $L/D = 4$, $M = 0.15$. *Initial condition* UINF, *shear layer mode.*

The flow over a shallow cavity oscillating in shear layer mode resembles the one from a deep cavity, described in section §3.3. Figure 3.24 shows the isocontours of vorticity, where the recirculation region next to the downstream corner is clearly displayed. Two waves are identified along the shear layer, corresponding to the oscillation in second Rossiter mode.

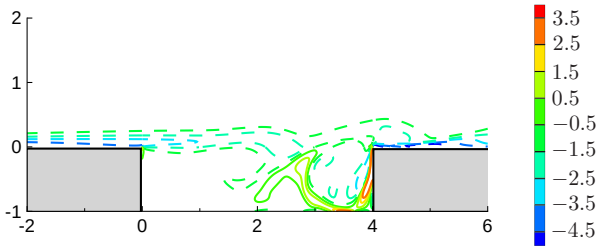

Figure 3.24 - *Instantaneous vorticity isocontours* $\omega D/u_\infty$, *dashed negative values.* $L/D = 4$, $M = 0.15$. *Initial condition* UINF, *shear layer mode.*

From figure 3.20 it is observed that the time-history of the case BLAS seems to present a low-frequency modulation. This is further enhanced in the time-history of vorticity at the location P2, shown in figure 3.25(a), where the amplitude of the fluctuations changes periodically. The spectra of the vorticity fluctuations in figure 3.25(b) confirms that the flow presents two main frequencies of oscillation: $St_2 = 0.82$, corresponding to the second Rossiter mode, and $St_D^{low} = fD/u_\infty = 0.005$.

A low frequency was also observed by Brès and Colonius [23] in their 3D DNS simulations of a cavity $L/D = 2$, $M = 0.6$, finding $St_D^{3D} = 0.026$. It should be mentioned that the corresponding two-dimensional simulation did not present this modulation. Chang *et al.* [28] also observed in their 3D LES simulations of a laminar flow over a cavity a low frequency modulation, which from their figures

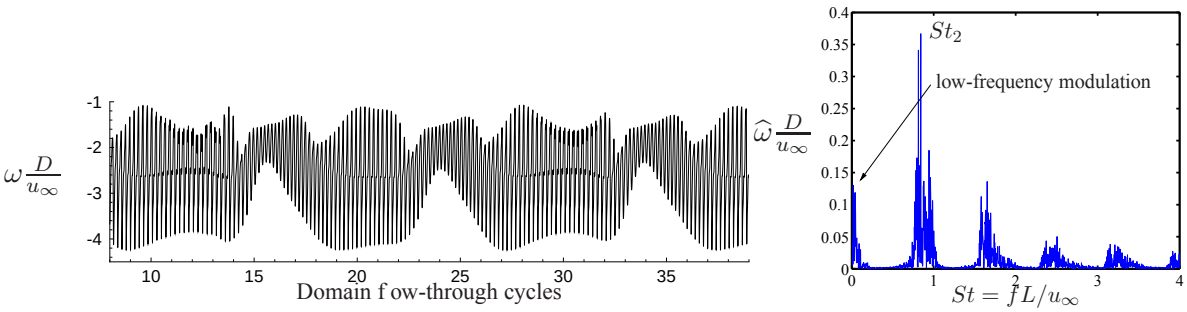

(a) Time-history (b) Spectrum

Figure 3.25 - *Time history and spectrum of vorticity fluctuations at P2.* $L/D = 4$, $M = 0.15$. *Initial condition* BLAS, *shear layer mode with a low-frequency modulation.*

can be estimated to be in the order of $St_D^{3D} \approx 0.025 - 0.03$. They attribute this low modulation to *a consequence of the shear layer interaction with the trailing edge and with the recirculating motions inside the cavity*.

Brès and Colonius [23] showed by 3D linear stability analysis that this low frequency is a centrifugal three-dimensional instability, and predicted the centrifugal modes for several cavity configurations. Furthermore, by 3D linear simulations of a cavity $L/D = 4$ and Mach number 0.3, they found a value of $St_D^{3D} = 0.011$ for $L/\theta = 30.1$, and $St_D^{3D} = 0.026$ for $L/\theta = 60.2$.

This low frequency modulation, to the authors' knowledge, has not been observed in 2D numerical computations. Obviously the present results from two-dimensional simulations do not match the values predicted as centrifugal modes. It is not clear at the moment which is the origin of the low-frequency modulation, if it is purely a numerical artifact or it can have a physical explanation.

Concerning the instantaneous vorticity field, there is no difference respect to the shear layer case without low-frequency modulation obtained with the initial condition UINF. It presents a recirculation region near the downstream wall as shown in figure 3.24.

3.4.3 Overall Sound Pressure Levels

Figures 3.26(a), 3.26(b) and 3.26(c) show the Overall Sound Pressure Levels for the initial conditions BLAS, UINF and ZERO respectively. In contrast to the deep cavity, where a directivity of 135° respect to the stream direction was found, in this case the waves propagate in the direction of the flow. This result is in agreement with the findings of Ahuja and Mendoza [2], who report a flat directivity for shallow cavities.

The wake mode, shown in figure 3.26(c), is louder than the two cases oscillating in shear layer mode. The cavity initialized with BLAS, oscillating in shear layer and a low-frequency mode, is about 5dB louder than the cavity initialized with UINF.

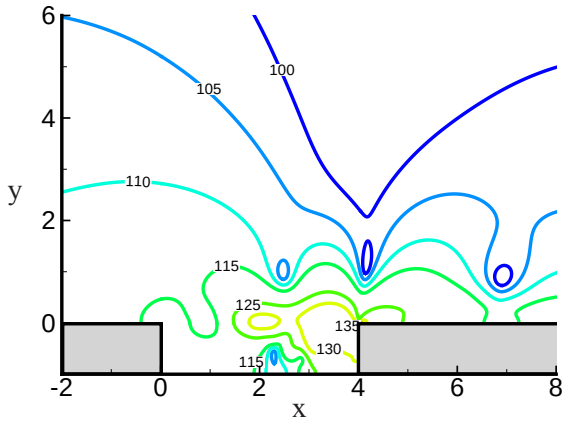

(a) Initial condition BLAS, shear layer mode with a low-frequency modulation.

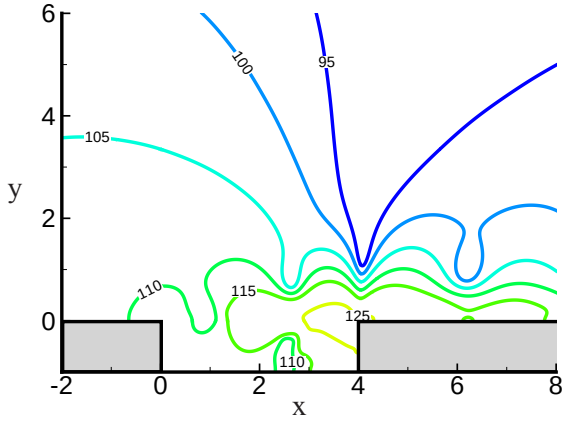

(b) Initial condition UINF, shear layer mode.

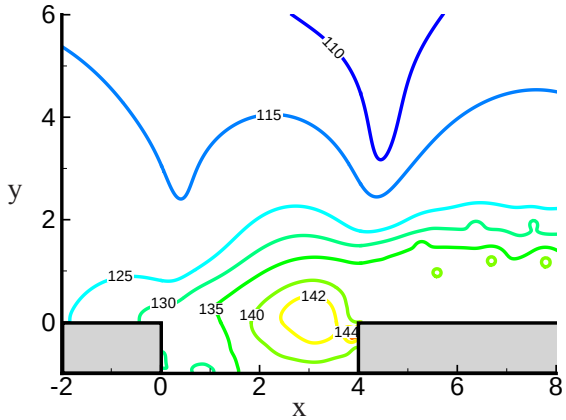

(c) Initial condition ZERO, wake mode.

Figure 3.26 - *Overall Sound Pressure Levels isocontours.* $L/D = 4$, $M = 0.15$.

3.4.4 Effect of Mach number and boundary layer thickness

The initial condition has been proved to have an important role in the oscillation regime of a low Mach number flow spanning over a shallow cavity. The aim of this section is to investigate if such an effect is found for other configurations.

According to the study by Rowley *et al.* [151], by increasing the Mach number the flow changes from a shear layer mode to wake mode. For this reason, the Mach number has been increased to 0.4 and 0.6, maintaining $L/\theta = 96.8$ as well as all the other parameters shown in table 3.5. The flow has been initialized with `UINF`, which leads to a shear layer mode when $M = 0.15$. The new cases $M = 0.4$ and $M = 0.6$ oscillate in wake mode. This result suggest that moderate subsonic Mach number flows always oscillate in wake mode, regardless of the initial condition.

The dependence on the boundary layer thickness is also investigated. For this study, the Mach number is kept at 0.15 and L/θ is reduced to 60 and 30, which implies a consequent modification of the other flow parameters, who are shown in table 3.5 and compared with the base case. In this case the flow is initialized with the initial condition `ZERO`, which develops a wake mode when $L/\theta = 96.8$. The results show that when the boundary layer thickness increases, the flow does not oscillate, independently of the initial condition.

Other combinations involving Mach numbers 0.4 and 0.6 and $L/\theta \approx 30$ and $L/\theta \approx 60$ have been computed. The flow parameters as well as the oscillation mode are displayed in table 3.5. The cases at Mach number 0.6 are in good agreement with the results published by Rowley *et al.* [151]. The results suggest that when the Mach number or L/θ increases, the ambiguity concerning the oscillation mode disappears, the resulting flow becoming independent on the initial condition. This might be due to the natural instability of the flow.

Mach	δ/D	L/θ	Re_D	Re_θ	mode regime
0.15	0.31	96.8	1511	62.5	SL/W
0.15	0.50	60.1	940	62.6	NO
0.15	1.00	30.0	470	62.6	NO
0.4	0.31	96.9	1522	62.9	W
0.4	0.52	57.8	895	62.0	SL
0.4	1.04	28.8	448	62.2	NO
0.6	0.31	96.2	1504	62.6	W
0.6	0.50	60.1	940	62.6	SL

Table 3.5 - *Flow parameters and results of the different test cases of cavity $L/D = 4$. W = Wake mode; SL = Shear Layer mode; NO = No Oscillations.*

3.5 Conclusions

Cavity flow simulations for different configurations have been made, in which the influence of the initial condition has been studied. This is an issue to which little attention has been given, but which plays an important role in the numerical results.

Firstly a deep cavity of $L/D = 2$ and moderate Mach number $M = 0.6$, clearly oscillating in shear layer mode, is considered. The results of the present and previous studies show that the dominant mode of a cavity flow oscillating in shear layer regime is difficult to predict. Five initial conditions are used. One of them leads to a flow oscillating at the first Rossiter mode at the beginning of the simulation, but later it changes to the second Rossiter mode. All the other initial conditions show that the dominant frequency corresponds to the second Rossiter mode.

The flow presents some differences depending on the dominant oscillation mode. When the flow oscillates at the first Rossiter mode, one vortex is found along the opening of the cavity. On the other hand two vortices are observed when the second Rossiter mode is dominant, and a more enhanced directivity of the acoustic radiation. Concerning the OSPL values, the initial condition does not seem to have an effect. If flow control is to be applied, the frequencies aimed should be the first and second Rossiter modes, since the suppression of only one of them might lead to the increase of amplitude of the other one.

Higher Rossiter modes are usually found for higher Mach numbers and thinner boundary layers. A change of the boundary layer thickness shows that indeed for larger boundary layer thickness, which correspond to more stable flows, the main frequency of oscillation is the first Rossiter mode. A change of Mach number, from 0.6 to 0.4, has not shown any significant difference.

The second test case of this investigation is a shallow cavity of $L/D = 4$, whose results respect to the flow regime are contradictory. Here the initial condition has a more important effect, since the flow regime has been found to change. Three initial conditions have been applied in a cavity with the following parameters: $L/D = 4$, $M = 0.15$ and $L/\theta = 96$. If the initial condition is a uniform flow, a shear layer mode is observed, while initializing with a zero mean flow leads to wake mode. The third case is more particular: an initialization with a boundary layer leads to a shear layer mode with a low-frequency modulation of unknown origin. These results suggest that the initial condition should be carefully chosen.

The flow parameters for which there is an ambiguity in the result are identified, showing that cavities with higher Mach number or boundary layer momentum thickness seem to be unaffected by the initial condition.

Appendix: review of cavity f ow studies

In this last section a review of cavity f ow studies is included, where the method of investigation and the main f ow parameters are given. The results concerning the oscillation mode are explained. For the deep cavities, the Rossiter modes which have been observed are given, pointing out which is the dominant one.

For shallow cavities, the oscillation regime (non-resonant, shear layer or wake mode) is given. If the cavity oscillates in shear layer mode, the Rossiter modes are described as for the deep cavities. When the cavity oscillates in wake mode, the frequency of oscillation is given.

Deep cavities: 2D numerical simulations

Study	Method	L/D	Mach	Flow regime	Results
Brès and Colonius (2007,2008) [21, 23]	2D DNS 2D DNS	2	0.3 0.35 - 0.6	laminar	St_2* St_1*
Gloerfelt (2001) [75]	2D DNS	2	0.7	laminar	St_2*
Gloerfelt (2006) [76]	2D DNS	2	0.6	laminar	St_1, St_2*
Hamed *et al.* (2001) [87]	2D DNS	2	0.6 0.9, 1.1	laminar	St_1*, St_2 St_1, St_2*
Rona and Brooksbank (2003) [148]	2D $k-\omega$, POD	3	1.5	turbulent	St_2*
Rowley *et al.* (2002) [151]	2D DNS	2	0.2-0.6 0.7-0.8	laminar	St_1*, St_2 St_1, St_2*

Table 3.6 - *Review of deep cavity studies: 2D numerical simulations.* St_i *represents the* i^{th} *Rossiter mode, where* St^* *indicates the dominant mode.*

Deep cavities: 3D numerical simulations and experiments

Study	Method	L/D	Mach	Flow regime	Results
Brès and Colonius (2007,2008) [21, 23]	3D DNS	2	0.325 0.6	laminar	St_1* St_2*
Cattafesta *et al.* (1998) [26]	experimental	2	0.4	turbulent	mode switch
Chang *et al.* (2006) [28]	3D LES	2	$<<0.1$	laminar turbulent	St_2* St_1*, St_2
Chatellier *et al.* (2004) [31]	experimental	1	$<<0.1$	turbulent	St_1, St_2, St_3*
Comte *et al.* (2008) [50]	3D LES, DES	0.42	0.78	turbulent	St_1*
Emmert *et al.* (2008) [58]	3D LES	2.5	0.1-0.25	turbulent	St_2,St_3
Ethembabaoglu (1973) [59]	experimental	<0.75 >0.75 >2	low	turbulent	St_1*, St_2 St_1, St_2* St_2*,St_3
Forestier *et al.* (2000) [64]	experimental	2	0.8	turbulent	St_1*, St_2
Forestier *et al.* (2003) [65]	experimental	0.42	0.5,0.65,0.7 0.6,0.75,0.8	turbulent	St_2* St_1*
Gharib and Roshko (1987) [71]	experimental		low	laminar	$L/\theta<127$,St_2* $L/\theta>127$,St_3*
Gloerfelt *et al.* (2003) [78]	3D LES	3	0.8	turbulent	mode switch
Haigermoser (2009) [84]	experimental	3	$<<0.1$	laminar	St_2*
Hassan *et al.* (2009) [90]	experimental	0.2	$<<0.1$	turbulent	St_1*
Kegerise *et al.* (2004) [104]	experimental	2	0.2-0.6	turbulent	mode switch
Krishnamurty (1956) [111]	experimental	2,2.5,3.3	0.4-0.8 0.65-0.8	laminar turbulent	St_2* St_1, St_2
Larchevêque *et al.* (2003) [115]	3D LES	0.42	0.8	turbulent	St_1*, St_2, St_3, St_4
Larchevêque *et al.* (2007) [113]	3D LES	2	0.8	turbulent	mode switch
Marsden *et al.* (2003) [130]	3D LES	1	0.6	laminar	St_1, St_2*
Podvin *et al.* (2006) [139]	3D DNS	2	$<<0.1$	laminar	St_2*
Rossiter (1966) [150]	experimental	1 1 1 2 2 2	0.4 0.45-0.8 0.85-1.1 0.4,0.8-1.1 0.5-0.6 0.7	turbulent	St_3* St_1* St_2* St_2* St_3* St_4*
Sarohia (1977) [156]	experimental	<0.8 >0.8	low	laminar	St_1* St_2*
Ukeiley and Murray (2005) [174]	experimental	1.49	0.17	turbulent	St_1, St_2*
Zhang (1988) [183]	experimental	3	1.5	turbulent	St_2*
Zhang *et al.* (1998) [184]	experimental 3D $k-\omega$	3	1.5	turbulent	St_1, St_2*, St_3 St_1, St_2*, St_3

Table 3.7 - *Review of deep cavity studies: experimental and 3D numerical simulations. St_i represents the i^{th} Rossiter mode, where St^* indicates the dominant mode.*

Shallow cavities

Study	Method	L/D	Mach	Flow regime	Mode	Results
Brès (2007) [21]	2D DNS	4	0.6	laminar	W	St_D = 0.063
	3D DNS	4		L, no dis (1)	W	St_D = 0.063
	3D DNS	4		L + dis (2)	SL	St_2*
Cattafesta *et al.* (1998) [26]	experimental	4	0.6	turbulent	SL	mode switch
Crook *et al.* (2007) [53]	experimental	6	$<< 0.1$	turbulent	SL	
De and Henshaw (2000) [55]	experimental	5	0.85	turbulent	SL	St_1, St_2*, St_3
Debiasi and Samimy (2004) [56]	experimental	4	$M < 0.3$	turbulent	SL	St_3*
			$0.32 - 0.38$			St_2, St_3
			$0.38 < M$			St_2*
Ethembabaoglu (1973) [59]	experimental	$4 - 6$	$<< 0.1$	turbulent	SL	St_2*, St_3
Geveci *et al.* (2004) [70]	experimental	5	≈ 0.1	turbulent	SL	St_2*
Gharib and Roshko (1987) [71]	experimental		low	laminar	SL	$L/\theta < 127$,St_2*
					SL	$L/\theta > 127$,St_3*
					W	$L/\theta > 155$
Gloerfelt (2001) [75]	2D DNS	4	0.5	laminar	SL	$L/\theta = 63$,St_2*
					W	$L/\theta = 280$
Haigermoser (2009) [84]	experimental	4	$<< 0.1$	laminar	SL	St_2*
Kegerise *et al.* (2004) [104]	experimental	4	0.2-0.6	turbulent	SL	mode switch
Lai and Luo (2007) [112]	3D LES	5	0.85	turbulent	SL	St_1, St_2, St_3*
Larchevêque *et al.* (2004) [114]	3D LES	5	0.85	turbulent	SL	mode switch
Larsson *et al.* (2003) [116]	2D DNS	4	0.15	laminar	W	St_D = 0.061
Murray (2006) [136]	experimental	6	0.2 - 0.8	turbulent	SL	mode switch
Rossiter (1966) [150]	experimental	4	0.4	turbulent	SL	St_2*, St_3
			0.9			St_1, St_2*, St_3
Rowley *et al.* (2002) [151]	2D DNS	4	0.2,0.3	laminar	SL	St_2*
			0.4-0.6		W	St_D = 0.064
			0.7,0.8		W	St_D = 0.061
Shieh and Morris (2000) [158]	2D DES	4.4	0.6	turbulent	W	St_D = 0.05
Shieh and Morris (2001) [159]	2D DES	4.4	0.6	turbulent	W	St_D = 0.05
	3D DES	4.4			SL	St_1, St_2
Suponitsky *et al.* (2005) [164]	3D LES	4	$<< 0.1$	T, no dis (1)	W	St_D = 0.067
				T + dis (2)	SL	St_2*
Ukeiley and Murray (2005) [174]	experimental	5.16	0.17	turbulent	NO	
Yao *et al.* (2004) [182]	3D DNS	4	$<< 0.1$	laminar	SL	

Table 3.8 - *Review of shallow cavity studies. SL = shear layer mode, W = wake mode, NO = non-resonant.* St_D *is the Strouhal number based on the cavity depth,* St_L *is the Strouhal number based on cavity length,* St_i *represents the* i^{th} *Rossiter mode, where* St^* *indicates the dominant mode. (1) no disturbances were imposed at the inflow. (2) disturbances were imposed at the inflow.*

Lire
la seconde partie
de la thèse